Quaternary Science Reviews 361 (2025) 109405

Contents lists available at ScienceDirect

Quaternary Science Reviews

journal homepage: www.elsevier.com/locate/quascirev

Unravelling the formation processes and depositional histories of the Middle Palaeolithic Ararat-1 Cave, Armenia: A multiscalar and multiproxy geoarchaeological approach

Ioannis A.K. Oikonomou [a,b,*], Theodoros Karampaglidis [c], Kaja Fenn [d], Shira Gur-Arieh [e], David Nora [a,f], Laura Sánchez-Romero [a,g], Dominik L. Rogall [a], Delphine Vettese [h], Boris Gasparyan [i], Artur Petrosyan [i], Ariel Malinsky-Buller [a]

[a] Human-Environment Dynamics Laboratory (HUMENDY), Institute of Archaeology, The Hebrew University of Jerusalem, Mt. Scopus, 91905, Jerusalem, Israel
[b] Malcolm H. Wiener Laboratory for Archaeological Science, American School of Classical Studies at Athens, 106 76, Athens, Greece
[c] Department of Geological and Mining Engineering, University of Castilla-La Mancha, 45004, Toledo, Spain
[d] Department of Geography and Planning, University of Liverpool, L69 7ZT, Liverpool, UK
[e] Institute for Prehistory and Early History, Christian-Albrechts-University, 24118, Kiel, Germany
[f] ICArEHB, Interdisciplinary Center for Archaeology and Evolution Human Behaviour, University of Algarve, Campus de Gambelas, 8005-139, Faro, Portugal
[g] Human Evolution Research Center, University of California, 3101 Valley Life Sciences Building, Berkeley, CA, 94720, USA
[h] Department of Art History and Archaeology, University of Perpignan Via Domitia, 66860, Perpignan, France
[i] Institute of Archaeology and Ethnography, National Academy of Sciences of Armenia, 375019, Yerevan, Armenia

ARTICLE INFO

Handling editor: Donatella Magri

Keywords:
Geoarchaeology
Micromorphology
Multi-proxy analyses
Site formation processes
Stratigraphy
Middle Palaeolithic
Human behaviour
Armenia

ABSTRACT

The sedimentary sequence of Ararat-1 Cave encapsulates an intricate depositional archive (Marine Isotope Stage 3), crucial for our understanding of the Middle Palaeolithic in the Armenian Highlands and beyond. The study of this record is accomplished through the use of a multi-proxy geoarchaeological framework of analysis, incorporating stratigraphical, micromorphological, sedimentological, mineralogical, chemical, magnetic, micro-archaeological and geochronological methods. These analyses demonstrate the predominance of geogenic processes, including rockfalls, grain and debris flows, interbedded with aeolian sedimentation, as well as localised pyroclastic material in-wash events. Post-depositional alterations are primarily linked to intense bioturbation, as well as minimal karst-induced cementation and minor phosphate diagenesis. The study of the anthropogenic and biogenic records indicates dynamic human-animal habitation histories. Human visits, associated with combustion and consumption activities, were infrequent and short-lived, representing brief occupation episodes in a cave habitually visited by carnivores and herbivores. This high-resolution reconstruction of Ararat-1 Cave formation histories improves our understanding of regional settlement and mobility patterns, highlighting the presence of Middle Palaeolithic groups that temporarily camped in the Ararat Depression.

1. Introduction

Understanding the formation processes of Palaeolithic records, often in the form of complex palimpsests (*sensu* Malinsky-Buller et al., 2011; Vaquero, 2008; Bailey, 2007), is essential step in providing the interpretive context for deciphering past hunter-gatherer lifeways. Numerous geoarchaeological investigations over the last few decades have shown the importance of the study of the sedimentary record from Palaeolithic sites as integral components of the exploration of the past settlement systems (e.g., Friesem et al., 2022, 2021, 2019; Benedetti et al., 2019; Leierer et al., 2019; Mallol et al., 2019; Karkanas et al., 2015a; Goldberg et al., 2009; Schiegl et al., 2003; Goldberg and Bar-Yosef, 1998). However, the relative absence of geoarchaeological investigations and the lack of stratified and well-preserved sites have partially obstructed the Palaeolithic research within the Armenian Highlands, hindering inter-site comparison, vital for the settlement patterns research. Many of

This article is part of a special issue entitled: Southern Caucasus published in Quaternary Science Reviews.

* Corresponding author. Human-Environment Dynamics Laboratory (HUMENDY), Institute of Archaeology, The Hebrew University of Jerusalem, Mt. Scopus, 91905 Jerusalem, Israel.
E-mail address: ioannis.oikonomou@mail.huji.ac.il (I.A.K. Oikonomou).

https://doi.org/10.1016/j.quascirev.2025.109405
Received 20 January 2025; Received in revised form 9 April 2025; Accepted 4 May 2025
Available online 13 May 2025

the archaeological assemblages derive from surface collections, reworked, secondarily deposited fluvio-colluvial sequences and/or open-air sites often lacking stratigraphic integrity (Egeland et al., 2014; Gasparyan et al., 2014). The absence of essential tools, such as archaeological micromorphology (e.g., Alapars-1; Malinsky-Buller et al., 2020), and the often merely descriptive character of stratigraphic documentation (e.g., Hovk-1, Pinhasi et al., 2008; often old excavations e.g., Yerevan-1: Gasparyan et al., 2014), have not permitted in-depth reconstruction of the depositional contexts, hindering inter-site comparisons, vital for the settlement patterns research.

Ararat Depression is a distinct geographical unit within the Armenian Highlands, a region of much interest for the palaeoanthropological research due to its high ecological diversity. The newly excavated MIS4-2 site of Ararat-1 Cave preserves a stratified geoarchaeological sequence that could potentially bridge the research gap of the missing Middle Palaeolithic archives, which limit our understanding of settlement patterns at the end of the period. In this article, we present the formation processes and depositional history of the Middle Palaeolithic cave of Ararat-1, reconstructed through a multi-scalar and multi-proxy geoarchaeological framework, incorporating micro-stratigraphic, sedimentological, mineralogical, elemental, magnetic, micro-archaeological, and geochronological analyses. The results highlight the importance of a multi-proxy geoarchaeological research for the study of low-intensity archaeological records.

1.1. Geographical and archaeological context

The Armenian Highlands and the Caucasus form a natural cul-de-sac at the crossroads of Africa, Europe and Asia, and exhibit high biogeographical diversity with implications for past population settlement and movement patterns (Adler and Tushabramishvili, 2004; Adler et al., 2006; Denk et al., 2001; Volodicheva, 2002). Covering an area of over 300,000 km^2, the Armenian Highlands border the Iranian Plateau to the east, the Asia Minor to the west, the Mesopotamian Plain to the south, and are linked to the Caucasus towards its northern margin – the Lesser Caucasus Mountains. The Caucasus is nestled between the Black and Caspian Seas and included the southern and northern flanks of the Greater Caucasus Mountain range (Oswald, 1906; Abich, 1882; Gasparyan and Glauberman, 2022). The elevational variability of the landscape is closely associated with the development of several altitude-dependent ecological niches. These range from low-elevation semi-deserts (≤c. 1200 m a.s.l.) to steppes, meadows and woodlands (c. 1200–2200 m a.s.l.), as well as (sub-) alpine belts (2200–5000 m a.s.l.; Fayvush and Aleksanyan, 2021; Williams, 2004). A similar tripartite geographical-altitudinal zonation has been proposed for the distribution of Palaeolithic sites within the limits of the state of Armenia (Gasparyan, 2010). The lower band at 450–600 m a.s.l. is associated with sites along the Debed River, bordering modern-day Armenia and Georgia, while sites of higher-altitude zones (1600–2500 m a.s.l.) are mainly found around the Akhuryan River Canyon and the Shirak and Lori depressions. Sites found within the Ararat Depression, Hrazdan and Arpa river gorges, at 900–1500 m a.s.l. represent the intermediate/middle altitudinal zone.

The Middle Palaeolithic record of the Southern Caucasus and the Armenian Highlands, limited by the lack of in-depth site formation studies, exhibits spatiotemporal gaps that obstruct the comprehensive understanding of the period. Sites dated to the MIS 7, 6, or 5 are very rare, except for the records from Jruchula Cave (Meignen and Tushabramishvili, 2010; 2007; Mercier et al., 2010), Hovk-1 Cave (Pinhasi et al., 2011) and Alapars-1 (Malinsky-Buller et al., 2020). The majority of the excavated sites in this region date to the end of the Middle Palaeolithic, during Marine Isotope Stages 4-2 (MIS4: 71–14 ka BP; Lisiecki and Raymo, 2005), marking the transition to the Early Upper Palaeolithic, a period often associated with population movement and replacement (Cullen et al., 2021; Adler et al., 2008, but see Goder-Goldberger and Malinsky-Buller, 2022).

Middle Palaeolithic (MIS 4–2) sites in the Hrazdan River Gorge (Armenia) include Yerevan-1 (913 m a.s.l.) and Lusakert-1 caves (1420 m a.s.l.; Williams, 2004; Gasparyan and Glauberman, 2022; Brittingham et al., 2019; Gasparyan et al., 2014; Adler et al., 2012; Birtwistle and Yeritsyan, 2012; Fourloubey et al., 2003) and the open-air site of Alapars-1 (1774 m a.s.l.; Malinsky-Buller et al., 2020). Additional sites at high-elevation zones include the open-air site of Kalavan-2 (1600 m a.s.l.; Malinsky-Buller et al., 2021; Ghukasyan et al., 2011), documenting repeated but ephemeral occupations and Hovk-1 cave (2040 m a.s.l.; Pinhasi et al., 2011, 2008), representing a chronologically rare example during the MIS5 with low-intensity human occupations alternated by animal habitation. Middle and lower altitudinal zones have been only sparsely investigated. The open-air sites such as Barozh-12 (1336 m a.s.l.) and Bagrateshen-1 (457 m a.s.l.), situated within these zones, preserve alluvial-colluvial sequences and palaeosols with variable degrees of reworking (Glauberman et al., 2020a; 2020b; Egeland et al., 2016; Glauberman et al., 2016). Middle Palaeolithic occurrences within the same elevational zones have been reported in adjacent regions. The caves of Ortvale Klde (530 m a.s.l.) and Bondi (477 m a.s.l.), in Georgia, are associated with intermittent occupations (Adler and Bar-Oz, 2009; Adler et al., 2008). Gazma cave in the Nakhchivan Autonomous Republic, with deposits dated to 55–40 ka BP, fall in the same framework (Zeynalov et al., 2023; Zeinalov et al., 2010). The end of the period and the onset of the Upper Palaeolithic era is documented in the high-elevation cave of Aghitu-3 (1601 m a.s.l.; in volcanic bedrock), at c. 39 ka BP, ~10 ka after the earliest occurrence in Georgia at Ortvale Klde (Kandel et al., 2011, 2014, 2017).

1.2. Ararat Depression and Ararat-1 cave

The Ararat Depression is situated within the southern forelands of the Lesser Caucasus and the northeastern part of the Armenian Highlands (Fig. 1A). Extending between Armenia and Turkey, it is an intermontane plateau, shaped by volcano-tectonic activity (Avagyan et al., 2018; Valder et al., 2018; Karampaglidis et al., 2025). The stratovolcanoes of Mt. Ararat (or Ağrı Dağı; 5165 m a.s.l.) and Mt. Aragats (4095 m a.s.l; Gevorgyan et al., 2020; Kirscher et al., 2020; Gevorgyan et al., 2018) denote the boundaries of the basin (area 1300 km^2 and drainage area 31500 km^2), in which Araxes River and its tributaries flow (Weller et al., 2006). The eastern part of the depression is dominated by the Devonian-Triassic-Cretaceous and Paleogene sedimentary formations and includes limestones (often fossiliferous and sandy limestones), silt- and sand-stones, marls and conglomerates, as well as travertines (Avagyan et al., 2018; Adamia et al., 2011). Volcanic rocks and volcanoclastic successions formed during or prior to the Pleistocene are also present (e.g., Gegham, Aragats and Ararat volcanic regions; Avagyan et al., 2018: 489; Lebedev et al., 2011). Cenozoic infillings and Quaternary alluvial sedimentary sequences are also present in the Depression (Valder et al., 2018). Receiving an average annual precipitation of 200–250 mm, the regional climate of the landlocked Ararat Depression is semi-dry and highly continental (Volodicheva, 2002). This is associated with the development of xerophilous vegetation communities, xerophytes and phrygana, formed on semi-desert calcisols and solonchacks/saline soils (Fayvush and Aleksanyan, 2021, 2022; Ghazaryan, 2013).

Ararat-1 Cave is located at the southeastern extremities of the Ararat Depression (39° 51′ 3.7908″ N, 44° 46’ 8.6232” E; elevation: 1034 m a.s.l.), c. 6 km from the modern town of Ararat (Fig. 1). Ararat-1 is a dissolution, joint-guided, relict cavity, situated within Devonian, steeply-dipping limestone, dominated by sparitic calcite cement with few intraclasts and oolites. It appears to be part of an extensive karstic system, similar to those reported for the areas near Ararat town and Vedi River (Ruggieri et al., 2022), but its extent remains largely uninvestigated. The cave consists of the main entrance, covered by series of roofspall debris and debris flows, the main chamber (maximum height c. 6m; maximum width (transversal) c. 4.5m; maximum length

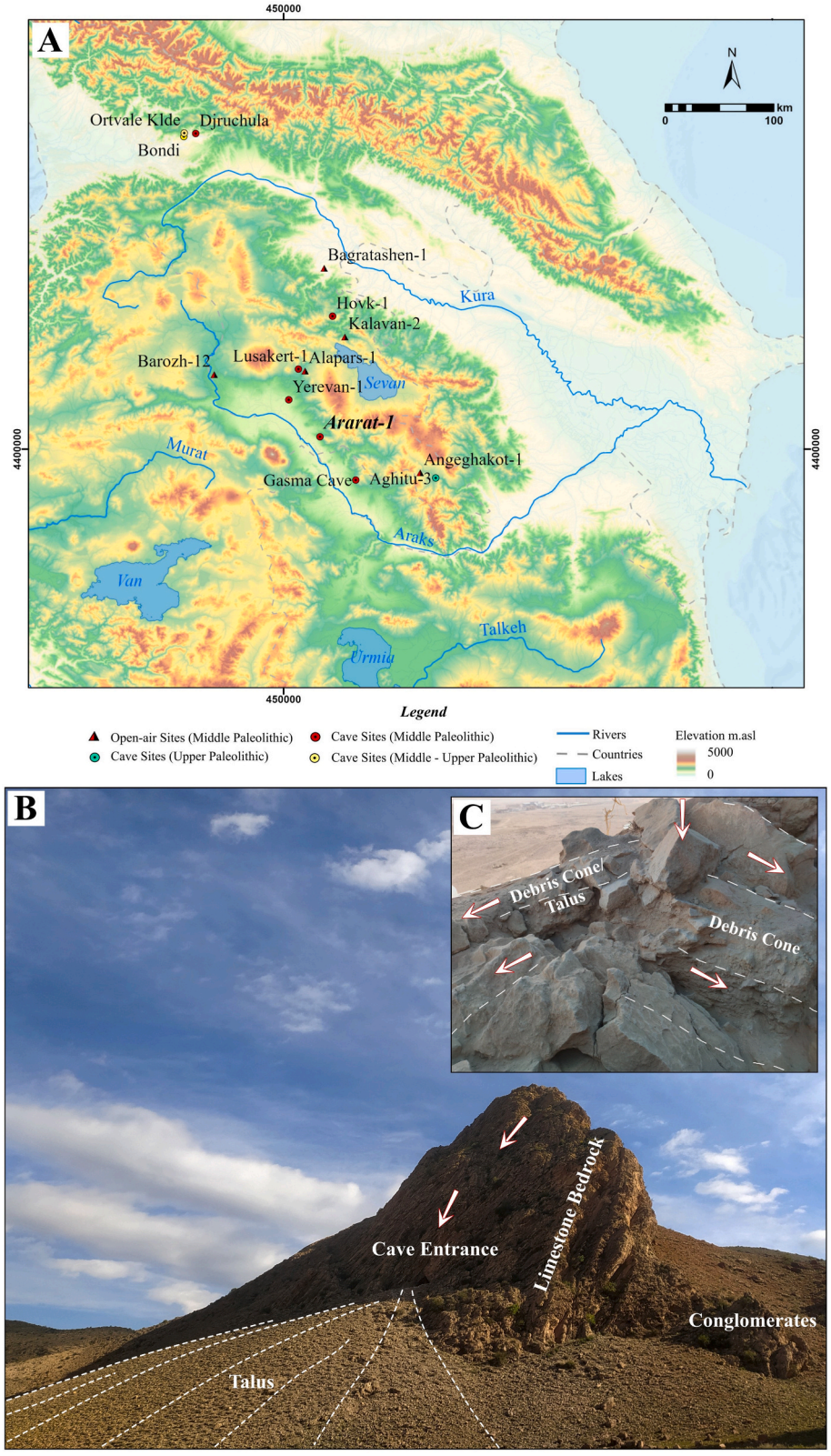

Fig. 1. **A**) Map of the Armenian Highlands landscape and the adjacent regions, showing the location of Ararat-1 Cave in relation to the distribution of some of the Middle and Upper Palaeolithic Cave and Open-air sites. **B**) Ararat-1 Cave and its settings. The disintegration of the limestone cliff results into the formation of a massive talus, as well as the incorporation of weathering products inside the cave. **C**) The current cave entrance and the point of rockfall impact, resulting in material deposition towards the cave interior and the external slope.

(longitudinal) c. 5.5m), and three small circular passages/conduits. The conduits show downwards inclination, from the internal to the external parts of the cave, formed under vadose conditions. The archaeological remains were found only within the main chamber of the cavity and the entrance.

The site was first excavated in 2018–2019 to reveal a late Middle Palaeolithic sequence, dated to 52–35 ka. Preliminary stratigraphic and sedimentological analyses of the interior/rear part of the cave suggested four phases of sedimentary accumulation in the MIS3 and the Holocene, documenting the presence of humans and other animals (Sherriff et al., 2024). A combination of aeolian and cave rockfall depositional processes has been suggested as the main sediment accretional agent in the site. The upper strata have been reportedly disturbed by bioturbation and anthropogenic, Holocene-dated, post-depositional alterations. The latter is documented by the presence of pottery. The underlying Middle Palaeolithic deposits, comprised mainly of lithic assemblages, indicate ephemeral occupation patterns of highly mobile hunter-gatherers who exploited a wide territory, as evidenced by the variable and distant sources of the raw materials (Nora et al., 2025; Frahm et al., 2025). Recent re-investigations (TransCause Project) included further on-site excavations (2022 and 2023), focusing on the spatial exploration of the entire cave (internal, rear, entrance and external parts).

2. Materials and methods

2.1. Field documentation and sampling

Thirty-five bulk samples (hence BSS1-35 column) were collected at 4-cm intervals throughout the entire extent of the stratigraphy from the Northern Profile (Fig. 2A). Oriented and undisturbed micromorphological blocks were extracted from all sedimentological units (Northern, Western, and Southern Profiles; Fig. 2). Additional bulk and block samples were collected from areas of particular interest (e.g., possible combustion features, sedimentary structures), cumulatively reaching 12 block and c. 100 bulk samples. For the extraction and storage of the blocks strategies similar to Karkanas and Goldberg (2017) and Stoops and Nicosia (2017) were followed. The off-site bulk sampling was conducted in parallel to the regional geomorphological survey led by Karampaglidis et al., 2025, with focus on the immediate environs of the cave, in order to create a reference collection of possible sediment sources (e.g., local colluvial, alluvial deposits, etc.).

2.2. Optically stimulated luminescence (OSL)

The initial chronology for the Ararat-1 was previously developed by Sherriff et al. (2024) and this paper is supplementing it with five additional OSL ages. OSL samples were taken in 2019, 2022 and 2023 (Fig. 2). In each case sediment for analysis was collected by hammering opaque tubes (5 cm Ø) into cleaned surface. All samples were wrapped to prevent exposure to sunlight and transported to the University of

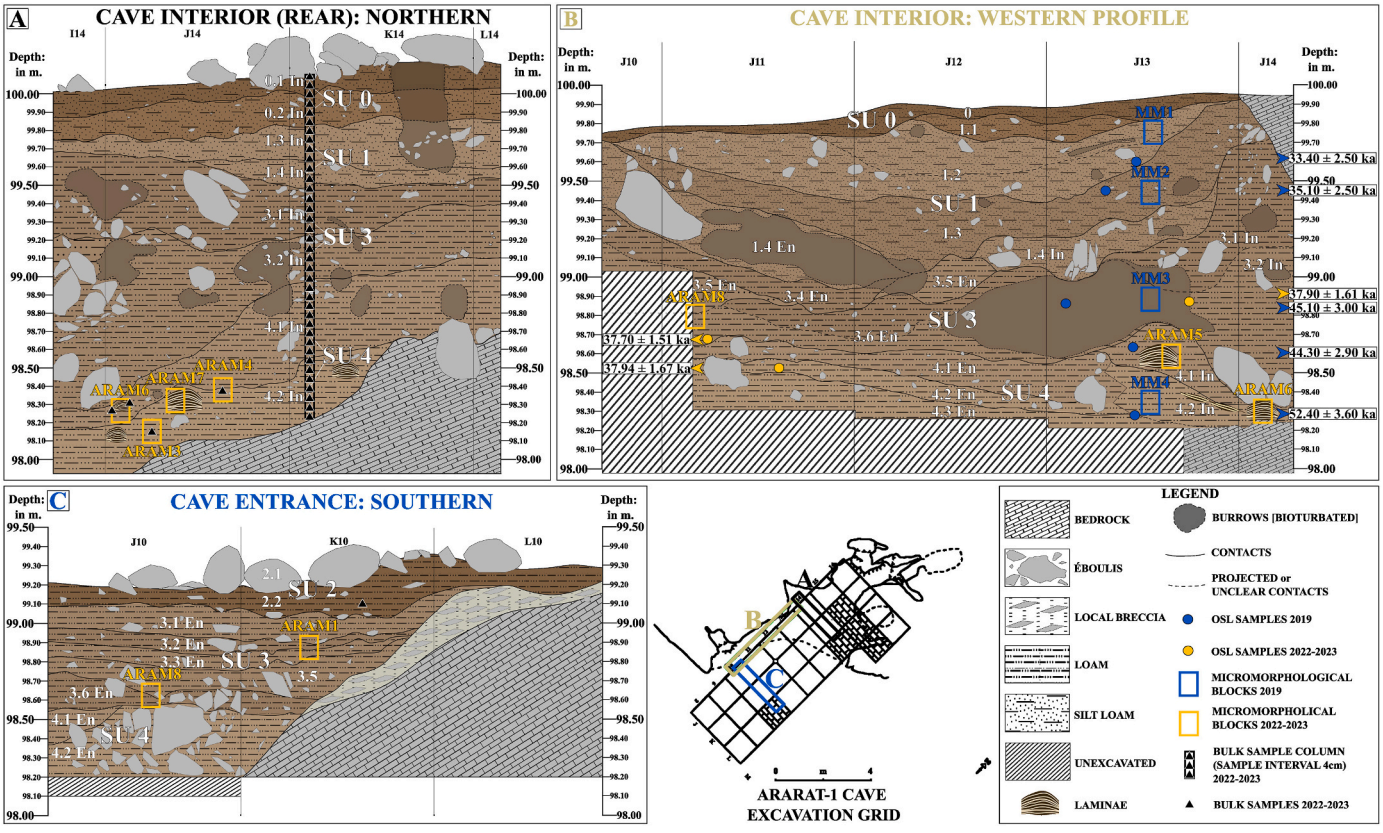

Fig. 2. A-C: The Stratigraphy of Ararat-1 Cave as documented in (**A**) the inner/rear parts of the Cave, the (**B**) main internal area, and (**C**) the entrance. The location of each area and respective profile is shown on the excavation grid/cave plan. The major sedimentological units are labelled as 'SU', followed by the respective number (e.g., SU1), while the sub-units are specified only as numbers (e.g., 3.2). The colours and the sediment textures (see legend) of the stratigraphic drawings are based on the results of the colourimetric and granulometric analyses. All analysed micromorphological, OSL, and bulk sediment samples, from the 2022–2023 season are illustrated. The main bulk sample sequence, "BSS1-35 Column" is noted on the Northern Profile. The location of the micromorphological and OSL samples from the 2019 season are not placed on the original profile surface, as the latter has been re-excavated and refreshed during the 2022–2023 expedition (see the relevant stratigraphic position in Sherriff et al., 2024).

Liverpool, where they were analysed under subdued orange light conditions. 4–11 μm polymineral fraction was extracted and used in all measurements. Following dose recovery tests, equivalent doses (De) were determined using the pIRIR225 protocol (Thomsen et al., 2008). To determine environmental dose-rates μDose (Tudyka et al., 2020) system was used to measure α and β emissions from collected sediment and μRate (Tudyka et al., 2023) to make dose rate calculations. A detailed information regarding luminescence dating protocol is presented in **SI.A**.

2.3. Bulk sedimentological and chemical analyses

Particle size analysis was undertaken at the Geological Survey of Israel, using the Malvern "MasterSizer 3000". Wet dispersion was used in all analyses and the Mie light scatter theory was applied. Prior to the analysis, dried samples were sieved using a <2 mm mesh, and submersed in c. 5 % hydrogen peroxide (H_2O_2; Gray et al., 2010) and c. 10 % hydrochloric acid (HCl) to remove organic matter and disintegrate calcium carbonate respectively (Crouvi et al., 2008). The prepared sediment was left overnight on a vertical rotating mixer in water dispersion that included 2 drops of sodium hexametaphosphate ($(NaPO_3)_6$ – 'calgon') to disaggregate finer, clay-sized grains. The characterisation of the sediment population and the particle size distribution was based on Folk and Ward (1957), utilising the μm-scaled logarithmic distribution plots. The BSS1-35 column and a single sample from the Entrance SU2 were analysed (Fig. 2A-B).

Particle **shape analyses** were conducted complimentarily on three selected samples using the ImageSizer Analysette 28 of Fritsch, without any prior chemical treatment (samples: AR22-BSS09, AR22-BSS16, AR22-BSS28 from the BSS1-35, representing SU1, SU3, and SU4 respectively). The sample preparation included the separation of the <2 mm fraction through sieving. The measurement of the dry samples was achieved by a series of high-resolution photographs with a telecentric lens and flashlight, based on dynamic image analysis conducted in the ImageSizing-Software (ISS). The morphological parameters of aspect ratio (AR; elongation), circularity (CI; roundness/circularity) and convexity (CO; roundness/surface roughness), with values expressed within the range of 0 to 1, were analysed. Minimum Ferret Diameter (in μm) is used for the determination of size classes. The analyses were conducted at the Human-Environment Dynamics Laboratory (hence Humendy Lab), in the Hebrew University of Jerusalem.

Inductively Coupled Plasma Atomic Emission Spectroscopy (ICP-AES) was used for the multi-elemental characterisation of bulk sediment samples. The <2 mm-sediment fractions were ground and sieved with a 75-μm mesh, prior to the analysis. Specimens of 0.25 g were subjected to four-acid digestion, utilitising a combination of nitric, perchloric and hydrofluoric acids, with a final dissolution stage of hydrocholoric acid. Five main elements (Al, Ca, Fe, Mn, P) and two element ratios (Al/Ca, Fe/Mn) were analysed as proxies to the depositional/hydrological regime and sediment sources (autochthonous vs allochthonous). The preparation and the analysis of the BSS1-35 column (Fig. 2B) and a single cave bedrock sample was performed commercially at the laboratories of ALS (see https://alsglobal.com/).

Loss-On-Ignition (LOI) was conducted at the Humendy lab in order to estimate of the **organic (**hence: **OM)** and **carbonate ($CaCO_3$) content**, following a modified version of Dean (1974) protocol. After weighing the grounded and dried sediments (at 90 °C/24 h), samples were heated at 550 °C in a muffle furnace for 4 h. The weight difference accounted for the estimate of the organic matter, as the latter is oxidised to carbon dioxide during the ignition. At a next stage, the sediments were re-heated at 1000 °C for 2 h and the weight loss after combustion accounted for the carbonate content (Heiri et al., 2001). The BSS1-35 column was analysed (Fig. 2B).

Magnetic susceptibility analysis was conducted at the Paleomagnetic Laboratory of the Institute of Earth Sciences, The Hebrew University of Jerusalem, using the MFK1 – Multifunction Kappabridge instrument from AGICO, with a low frequency sensor (976 Hz) and sensitivity of 5×10^{-8}. Prior to measurement, samples were ground, weighed, and placed in a cylinder (25.4 mm diameter x 22.0 mm length). Weights were used to convert values to mass-specific susceptibility (χ). The BSS1-35 column and 4 samples from selected contexts were analysed (2 from ARAM6 area, 1 from ARAM3 and ARAM4 respectively; Fig. 2B).

Colourimetry was performed at the Humendy Lab using a Konica Minolta Portable Colorimeter CR-400, following Ferro-Vázquez et al. (2021). The CR-400 system is based on a Cartesian (x, y) approach, following the Commission Internationale d' Eclairage (CIE), where the differences between colours are defined in a Euclidean manner (Scheinost and Schwertmann, 1999). The colour is translated into the (1) lightness/light-dark axes (L; 0–1), the (2) red-green axis (+a/-a) and the (3) yellow-blue axis (+b/-b), while the colour changes in the L, a, b components correspond to the perceived colour differences. The BSS1-35 column and 8 samples from the external profile were analysed.

2.4. Micro-archaeological analyses

Fourier Transform Infrared Spectroscopy – FTIR was implemented for the examination of the mineralogy and the organic component of the sediments, focusing on the determination of the relative concentrations of major minerals and the presence of diagenetically and thermally altered minerals (Weiner, 2010; Weiner et al., 2002; Regev et al., 2010; Berna et al., 2007; Karkanas et al., 2000; Schiegl et al., 1996). The analyses were conducted on the iS5 Thermo Scientific instrument, with an iD1 Transmission FTIR head, following the method of ultrapure potassium bromide (KBr; Weiner, 2010), at the Humendy Lab. A few micrograms of sample were ground using an agate mortar, mixed with a few milligrams of KBr, and left under high pressure for a few seconds to form the final transparent disk. The spectra were collected in transmission mode between 4000^{-1} and 400 cm^{-1}, with a resolution of 4 cm^{-1}. For the interpretation, the Infrared Spectra Library of the Kimmel Centre of Archaeological Science, Weizmann Institute of Science (https://centers.weizmann.ac.il/kimmel-arch/infraredspectra-library) was employed (Weiner, 2010), using the OMNIC 9 Software. The BSS1-35 column was analysed (Fig. 2B).

The study of **calcite pseudomorphs after calcium oxalate crystals**, commonly known as **ash pseudomorphs** can be informative in terms of diagenesis, as well as the use of fire and fuel selection practices (Gur-Arieh and Shahack-Gross, 2020). Ash pseudomorphs are formed after combustion, retaining the shape of the original calcium oxalates (CaOx) crystals present especially in woody plants, which are usually available as whewellite (CaC2O4·H2O) and weddellite (CaC2O4·2H2O; *ibid*). **Dung spherulites** are radially crystallised spherical bodies of calcium carbonate, usually with a diameter of 5–15 μm, formed in the intestines of certain animals, and in higher concentrations in ruminants (Shahack-Gross, 2011; Canti, 1997, 1998). The extraction and quantification of ash pseudomorphs and dung spherulites is executed simultaneously, following the method of Gur-Arieh et al. (2013). All microscopic analyses, including ash pseudomorph and dung sperulite analyses, were performed at the Wiener Laboratory of the American School of Classical Studies at Athens, Greece (ASCSA). The multi-step protocol included the homogenization of c. 50 mg of sediment, the sieving of the latter through a 150-μm mesh and its placement in a 1.5-ml Eppendorf tube, where 500 μl of 2.4 g/ml SPT solution were added. The mixture was then vortexed and sonicated for 10 min, while further vortexing was required prior to the transfer of 50 μl of the solution with a pipette onto a glass slide with 24 × 24 mm coverslip. For the calculation of the concentration of ash pseudomorphs and dung spherulites per gr of sediment, 20 fields of view were microscopically examined, at ×200 magnifications under Plane Polarised Light (PPL), and Crossed Polarised Light (XPL; Gur-Arieh et al., 2013). The ratio between ash pseudomorphs and dung spherulites can be utilised as a proxy for the use of the cave by human and animal agents. A sub-sample

of 17 samples from the BSS1-35 column was analysed (SU0, SU1, SU3, and SU4 included; Fig. 2BB).

2.5. Microscopic analysis of thin sections

The preparation of the micromorphological blocks included a drying period on the shelves, followed by oven drying at no more than 50 °C. A 85:15 mixture of polyester resin and acetone, adding Methyl Ethyl Ketone (MEKP), was utilised for the impregnation under the fume hood. The cured samples were stored in the storage cabinet for a few weeks. After sawing the blocks, the slabs were mounted on glass slides (9 × 5 cm) and were ground to 30 μm thickness. Preliminary mesoscopic observations were conducted through high-resolution scans/photographs of the thin sections and slabs (Arpin et al., 2002). The micromorphological analysis was conducted following the standard descriptive criteria of Bullock et al. (1985), Courty et al. (1989) and Stoops (2021), as well as relevant individual micromorphological publications. The thin sections were examined under the DM2700P petrographic polarising microscope of Leica at ×12.5, ×100, ×200, ×400 and ×500 magnifications, using a Leica Flexacam C1 and the Leica Application Suite X. The micromorphological analyses were conducted under PPL, XPL, Oblique Incident Light (OIL), and Ultra-Violet Light (UVL). Blue Fluorescent Light (BLF; Stoops, 2017) microscopy was performed through a Leica DMILM Inverted Microscope. Selected thin sections were studied under the Scanning Electron Microscopy and Energy Dispersive X-Ray Spectroscopy (SEM-EDS; Frahm, 2017), aiming to produce elemental maps of certain localities of interest. The JEOL (JSM-IT300LV) SEM and the Oxford Aztec STD X-act EDS was used in low vacuum mode, after applying a 20–40 nm carbon coating on the thin sections with the Quorum Q150R ES coating apparatus. The impregnation and sawing were conducted at the Environmental Micro-History Laboratory (EMH), University of Haifa, while the final thin sections were prepared at Quality Thin Sections, Arizona and the Wiener Lab (ASCSA; excluding MM1, 2, 3, and 4 from Sherriff et al., 2024). A total of 20 thin sections (ARAM1, 2, 3.A-B-C-D, 4.A-B, 5.A-B-C, 6.A-B, 7, 8.A-B) from 12 blocks, were analysed (Fig. 2).

3. Results

The main results presented in the following chapter are divided into five main sections. Section 3.1 contains information from macroscopic field observations, Section 3.2 bulk sedimentological and chemical analyses, Section 3.3 chronometric results, Section 3.4 micro-archaeological analyses, and Section 3.5 microscopic analyses of thin sections. Additional supporting data can be found in two **Supplementary Information** files (**SI**), **SI.A** and **SI.B**. **SI.A** (.docx) is divided in five segments, **SI.A1** to **SI.A5**. **SI B**, and **SI.B** (.xlsx) is divided in seven segments, **SI.B1** to **SI.B7**.

3.1. Field observations

The 2-m stratigraphic sequence of Ararat-1, as revealed after the excavation of the inner parts (northern and western profiles) and the entrance of the site (southern profile), was divided into five main Sedimentological Units (hence SU), encapsulating late Pleistocene and Holocene deposits (Fig. 2). The determination of the different SUs was based on changes in sedimentological properties, structure, texture, contacts, colour, representation of coarse component (gravel-to-boulder-sized rock fragments), presence of organic matter and bioturbation/disturbances. The (sub-) units are spatially variable throughout the site, with lateral variations observed in the Northern Profile at the inner/rear part of the cave, the Western Profile in the main cave area and the Southern Profile, at the cave entrance. The summary of the field observations of the Ararat-1 stratigraphy are presented here (Fig. 2; Table 1).

3.1.1. Cave interior/rear (Northern Profile)

The Northern Profile represents the rear parts of the cave (squares J14 and K14, partially I14- L14 too; Fig. 2A) and preserves a sequence of SU4, SU3, SU1 and SU0 strata (Table 1; **SI.A1**). SU4 (SU4.2–4.1) lies directly over the limestone bedrock, dipping towards the western part of the cave. It is unconformably overlain by the SU3 (SU3.2–3.1). SU3.2 follows the orientation of the SU4, while the overlaying SU3.1 appears semi-horizontal. The conformably superimposed SU1 (SU1.4–1.3) gently slope towards the east. The topmost SU0 (SU0.2-SU0.1) lies conformably/gradually above it and represents the cave topsoil.

3.1.2. Cave interior (Western Profile) and entrance (Southern Profile)

The Western Profile is exposed throughout the longitudinal axis of the cave (squares J11, J12, J13 and partially J10 and J14; Figs. 2 and 15; Table 1; **SI.A1**). The limestone bedrock has been only exposed within the inner/rear areas, where the overlain deposits follow the same stratification of the major SUs with the Northern Profile (i.e., SU4, SU3, SU1, and SU0). The rest of the profile (squares J10, J11, and partially J12) preserves similarly four sedimentological units that exhibit lateral variations, while the bedrock has not been detected. The lowermost SU4 (SU4.3–4.1) dips towards the inner/rear parts of the cave, while the lateral change to the internal SU4 is not clear. The SU4 deposits are conformably overlain by the SU3, which consists of a series of sub-units often exhibiting channel-like contacts (SU3.5–3.6 and SU3.4–3.5/3.6). The lateral contact to the inner parts is unclear, due to the presence of large burrows. It is unconformably overlain by the SU1 (SU1.4–1.1), which slopes towards the middle of the cave. It is conformably/gradually overlain by the SU0 (topsoil). The Southern Profile, situated at the cave entrance (squares J10, K10 and L10), preserves the sediments of the SU4, SU3 and SU2 (Fig. 2C; Table 1; **SI.A1**). The SU4 deposits are identical to the SU4 of the Western Profile and are conformably overlain by the SU3 (SU3.5–3.6 and 3.1–3.3). The latter is conformably superimposed by the SU2 (SU2.2–2.1), which extends up to the surface.

3.1.3. Cave exterior – talus

The external test trench preserves three main units (SU3, SU2, SU1) differentiated from the internal profiles (Table 2; Fig. 13; **SI.A1**). The basal SU3 (SU3.B-3.A) exhibits (semi-) horizontal orientation, but its lateral and vertical extent remains uninvestigated and mostly unexcavated. It is unconformably overlain by the SU2 (SU2.E-A), which appears inclined, following the slope towards the floodplain. The surface of the SU2 is capped by the SU1, which represents the topsoil.

3.2. Bulk sedimentological and chemical analyses

3.2.1. Particle size analysis

The particle size distribution is skewed and leptokurtic, with higher skewness and kurtosis values reported for the SU1-0. Silt (mode at 60–70 μm) is the most common grain fraction in Ararat-1, with a mean value of c. 50 %, ranging from ~56 % in the SU4.1 to ~34 % in the SU1.4 (Figs. 3A-B and 5A; **SI.B1**). The sand is the second most frequent fraction, with an average value of ~36 % and a range of ~52 % in the SU0.2 to ~29 % in the SU4.1. The average clay proportion is ~14 %, but it ranges from ~10 % in the SU0.2 to ~16 % in the SU3.1–4.1. The mean grain size of the sediment matrices from the northern profile is ~74 μm (very fine sand). The equivalent value for the upper SU0-SU1 and the lower strata SU3-SU4, when separated, is ~93 μm and ~64 μm respectively. The finest sediment is found in the lower sedimentological units, with minimum average size and mode values at ~54 μm and ~57 μm (SU4; coarse silt). Coarser matrices are found in the upper strata, where the highest average and mode values are noted, at ~155 μm and ~96 μm respectively (SU0; very fine sand).

The results show a gradual shift from finely-grained to slightly coarser-grained sediments from the bottom to the top of the sequence (Fig. 5A), as demonstrated by the decrease of the clay and silt fractions, and the increase of sand upwards. On the tertiary diagram the vast

Table 1
Field description of the stratigraphic sequence of Ararat-1 Cave, synthetically presenting all sedimentological units from the three main profiles: the Northern, the Western, and the Southern profiles; see Fig. 2). The presence of the suffix '**En**' denotes that the SU is present only within, or near the cave entrance. Colourimetric values are reported with reference to the values of Lightness - **L***, the red-green range - **a***, and the yellow-blue range - **b*** and the respective colours are visually represented. Field-collected Munsell-based equivalent observations are also reported. The characterisation of the texture is based on both macroscopic and analytical examinations.

Major Sedimentological Units (SU)[1]	Sub-Units	Short Description	Texture	Colour	Facies
4 (99.60/99.50 – 98.00/98.10)	**4.2**	Poorly-sorted, matrix-supported (C/F 10%), with angular limestone gravels/granules. Low bioturbation rates. Locally cemented &/or compacted. Direct contact to the limestone bedrock. Contact to **SU4.1** conformable. Present only within the inner/rear parts of the cave (Northern Profile & partially Western Profile; mainly squares J14 & K14). Occasional, fragmented, curved and parallel laminar features (hence **LF**) of (**a**) dark brown/black fine silty laminae interbedded with fine sandy to coarse sandy laminae (**LFa**) & (**b**) pale brown silty laminae (**LFb**), are present (depth: ~98.00-98.50/98.60).	Silt Loam* *Except LF: (a) Sandy Loam to Loam (b) Silt Loam to Silt	L*=61.16, a*=5.56, b*=17.96 Very Pale Brown 10YR 7/4	Slack-Water/Puddles (**LFa-b**) & Debris Flow Matrix-Supported (DFM)
	4.1	Poorly-sorted, matrix-supported (C/F 5-10%), with angular limestone clasts & gravels/granules. Locally cemented &/or compacted. Moderate bioturbation rates. Occasional, fragmented **LF**s are present. Contact to **SU3** unconformable. Present only within the inner/rear parts of the cave (Northern Profile & partially Western Profile; mainly squares J15 & K14).		L*=60.19, a*=5.35, b*=17.66 Very Pale Brown 10YR 7/4	
	4.2 En	Poorly-to-Moderately-sorted, clast-supported (C/F>33%), with angular limestone clasts & gravels/granules. Compacted. Low bioturbation rates. Contact to lower unit or bedrock unexplored. Contact to **SU 4.1 En** conformable. Present within the entrance and most of the inner parts of the cave (Southern Profile & most of the Western Profile; squares J10, J11, J12, part of J13).	Silt Loam		Debris Flow (DFC) Clast-Supported
	4.1 En	Very poorly-sorted, matrix-supported (C/F 20%), with angular limestone clasts & gravels/granules. Compacted. Low bioturbation rates. Contact to **SU 3** conformable. Present within the entrance and most of the inner parts of the cave (Southern Profile & most of the Western Profile; squares J10, J11, J12, part of J13).			
3 (99.00/98.90 – 99.60/99.50)	**3.2**	Poorly-sorted, clast-supported (C/F >33%), with angular/subangular limestone boulders and angular clasts/gravels. Loose. High bioturbation rates. Contact to **SU 3.1In** conformable, inclined. Present only within the inner/rear parts of the cave (Northern Profile & partially Western Profile; squares J13, J14 & K14).	Silt Loam		Debris Talus (DT)
	3.1	Poorly-sorted, matrix-supported (C/F <20%), with angular limestone clasts & gravels/granules. Loose. High bioturbation rates (severely bioturbated). Contact **to SU 1** unconformable, inclined. Present only within the inner/rear parts of the cave (Northern Profile & partially Western Profile; squares J13, J14 & K14).			Debris Flow Matrix-supported (DFM)
	3.6 En	Moderately-to-poorly-sorted, matrix-supported (C/F 10%), with angular/subangular limestone gravels. Loose. High/Moderate bioturbation rates. Contact to **SU 3.5/3.4** unconformable. Present within the entrance and most of the inner parts of the cave (Southern Profile & most of the Western Profile; squares J10, J11, J12 & K10).	Silt Loam	L*=59.96, a*=5.36, b*=17.74 Very Pale Brown 10YR 7/4	Debris Flow (Channel-like)
	3.5 En	Poorly-sorted, matrix-supported (C/F 10%), with angular/subangular limestone clasts & gravels. Loose. High/moderate bioturbation rates. Contact to **SU 3.4** & **SU 1** unconformable. Present within the entrance and most of the inner parts of the cave (Southern Profile & most of the Western Profile; squares J10, J11, locally J12 & K10).			
	3.4 En	Poorly-sorted, matrix-supported (C/F <10%), with angular/subangular limestone gravels & granules. Loose. High/moderate bioturbation rates. Contact to **SU 1** unconformable. Present only within inner parts of the cave (part of the Western Profile; square J11).			
	3.3 En	Moderately-to-poorly-sorted, matrix-supported (C/F 10%), with angular/subangular limestone granules. Loose. Moderate bioturbation rates. Contact to **SU 3.2** conformable. Present only within the entrance (Southern Profile).			
	3.2 En	Very poorly-sorted, matrix-supported (C/F 10%), with angular/subangular limestone clasts & gravels. Loose. Moderate bioturbation rates. Contact to **SU 3.1** conformable. Present only within the entrance (Southern Profile).			
	3.1 En	Moderately-to-poorly-sorted, matrix-supported (C/F 10%), with angular/subangular limestone granules. Loose. Moderate bioturbation rates. Contact to **SU 1** unconformable. Present only within the entrance (Southern Profile).			
2 (99.30 - 99.10)	**2.2 En**	Poorly-to-moderately-sorted, matrix-supported (C/F <5%), with rare angular/subangular gravels. Loose to compacted. Moderate/low bioturbation rates. Present only within the entrance (Southern Profile).	Silt Loam	L*=61.98, a*=6.67, b*=20.09 Very Pale Brown 10YR 7/4	Debris Flow
	2.1 En	Very poorly-sorted, clast-supported (C/F>50%), with angular/sub-angular limestone boulders, clasts, & gravels. Loose. Moderate bioturbation rates. Present only at the entrance surface. Present only within the entrance (Southern Profile).			Debris Flow/Rockfall (DFR)
1 (99.90/99.80 – 99.00/98.90)	**1.4**	Very poorly-sorted, clast-supported (C/F >33%), with angular limestone clasts & gravels. Loose. High bioturbation rates. Contact to SU 1.3 conformable. Present within the inner and rear parts (Northern Profile and portion of the Western Profile; part of J12, J13, J14, K14).	Loam	L*=58.51, a*=6.22, b*=18.84 Very Pale Brown 10YR 7/4	Debris Flow/Rockfall (DFR)
	1.4 En	Very poorly-sorted, clast-supported (C/F >33%), with angular limestone boulders, clasts & gravels. Loose. High bioturbation rates. Contact to SU 1.3 conformable. Present only near the entrance (mainly in J11). Present only within the inner and parts of the cave (Western and Northern Profile; part of J10, J11, J12, J13, J14, K14).			
	1.3	Moderately-to-poorly-sorted, matrix-supported (C/F 5%), with rare angular/subangular limestone clasts & gravels/granules. Loose. High bioturbation rates. Contact to **SU 1.2** conformable. Present within the inner and rear parts of the cave (Western & Northern Profile; squares J10, J11, J12, J13, J14, & K14).			Debris Flow Matrixx-Supported (DFM)
	1.2	Very poorly-to-poorly-sorted, matrix-supported (C/F 25%), with angular/subangular limestone clasts. Loose. High bioturbation rates. Contact to **SU 1.1** conformable. Present within the inner cave (Western Profile; squares J10, J11, J12, J13).			
	1.1	Moderately-to-poorly-sorted, matrix-supported (C/F 5%), with angular limestone gravels/granules. Loose. High bioturbation rates. Contact to **SU 0** conformable. Present within the inner cave (Western Profile; squares J12, J13).			
0 (100.00-99.90/99.80)	**0.2**	Poorly-sorted, matrix-supported (C/F 20-25%), with angular/subangular limestones boulders and clasts. Loose. High bioturbation rates; dung present. Note: vertical cracks/prismatic soil structure. Contact to **SU 0.1** conformable. Present only within the rear parts of the cave (Northern Profile; squares J14, K14).	Loam	L*=48.89, a*=7.90, b*=22.0 Dark greyish brown 10 YR 5/2	Cave Topsoil (Ap Horizon)
	0.1	Poorly-sorted, matrix-supported (C/F 5-10%), with angular/subangular limestones gravels. Loose. High bioturbation rates; dung present. Note: vertical cracks/prismatic soil structure. Cave surface. Present within the inner and rear parts of the cave (Western & Northern Profile; J10, J11, J12, J13, J14, K10, K14& L10).		L*=43.50, a*=7.95, b*=22.90 Greyish brown 10 YR 4/2	

[1]: Approximate elevation (in m) of the upper and lower contacts per major SU is given (the top and the bottom of the excavated sequence are c. 100.00 and c. 98.00 from datum).

Table 2
Field description of the stratigraphic sequence of the external profile, Ararat-1 Cave, represented in Squares J8-J9. Colourimetric values are reported with reference to the values of Lightness - **L***, the red-green range - **a***, and the yellow-blue range - **b*** and the respective colours are visually represented. Field-collected Munsell-based equivalent observations are also reported. The characterisation of the texture is based on both macroscopic and analytical examinations.

Major Sedimentological Unit (SU)	Sub-Unit	Description	Texture	Colour	Facies
3	3.B	Massive, poorly-to-moderately sorted, matrix-supported (C/F 20:80), with subangular/angular, $CaCO_3$-coated boulder-, cobble- and pebble-sized limestone clasts. Rare allochthonous red-coloured, pebble-/granule-sized rock fragments also reported. Highly indurated/cemented. Low bioturbation rates. Contact to underlying unit unknown (unexcavated); bedrock not exposed Note: Archaeological material present.	Sandy Loam	L*= 73.29, a*= 4.7, b*= 16.535 Very Pale Brown 10YR 8/4	Indurated deposits (?; Unexcavated)
	3.A	Massive, unsorted/poorly-sorted, clast-supported (C/F 50:50), with subangular/angular, elongated cobble-, pebble- and granule-sized limestone clasts. Moderately indurated/cemented. Low bioturbation rates. Contact to underlying **SU 3.B** unclear (partially exposed).	Loam	L*= 66.54, a*= 5.635, b*= 18.7 Very Pale Brown 10YR 7/4	Indurated Roof Collapse Debris (Talus)
2	2.E	Massive, poorly-sorted, matrix-supported (C/F 25%), with subangular/angular boulder- and pebble-sized limestone clasts (rare granule-sized too). Slightly compacted (non-indurated). Low bioturbation rates. Contact to underlying **SU 3.A** is inclined, uconformable.	Loam	L*= 65.66, a*= 5.78, b*= 18.75 Very Pale Brown 10YR 7/4	Debris Flow (Talus)
	2.D	Massive, unsorted/poorly-sorted, clast-supported (C/F 55:45), with angular pebble- and granule-sized limestone clasts. Slightly compact, with slightly indurated localities. Moderate-to-low rates of bioturbation. Contact to underlying **SU 2.E** inclined, unconformable.	Loam	L*= 67.015, a*= 5.455, b*= 18.38 Very Pale Brown 10YR 7/4	
	2.C	Massive, unsorted/poorly-sorted, clast supported (C/F 60:40), with angular/subangular pebble-sized limestone clasts (imbrication structures noted). Slightly loose. Moderate-to-low rates of bioturbation. Contact to **SU 2.D**, inclined, unconformable.	Silt Loam	L*= 62.39, a*= 6.52, b*= 19.445 Very Pale Brown 10YR 7/4	
	2.B	Massive, poorly-to-moderately-sorted, matrix-supported (C/F 25:75), with subangular pebble-sized limestone fragments (local imbrication structures noted). Slightly loose. Moderate rates of bioturbation (roots present). Moderate-to-low rates of bioturbation. Contact to **SU 2.C** (and **2.D** in localities were **2.C** is discontinuous) inclined, unconformable.	Silt Loam/Loam	L*= 62.455, a*= 6.18, b*= 18.785 Very Pale Brown 10YR 7/4	
	2.A	Massive, poorly-sorted, clast-supported (C/F 55:54), with angular/subangular pebble-sized limestone clasts (local imbrication structures noted). Loose. Moderate-to-low rates of bioturbation. Contact to **SU 2.B** is inclined, conformable.	Silt Loam	L*= 60.62, a*= 6.3, b*= 18.525 Very Pale Brown 10YR 7/4	
1	-	Massive, poorly-sorted, matrix-supported (C/F 25:75), with angular/subangular pebble-sized limestone clasts. Loose. Moderate-to-high rates of bioturbation (roots/organic matter present). Contact to **SU 2.A** is gradual, conformable.	Silt Loam	L*= 57.52, a*= 5.58, b*= 17.34 Brown 7.5 YR 5/4	Topsoil (A Horizon)

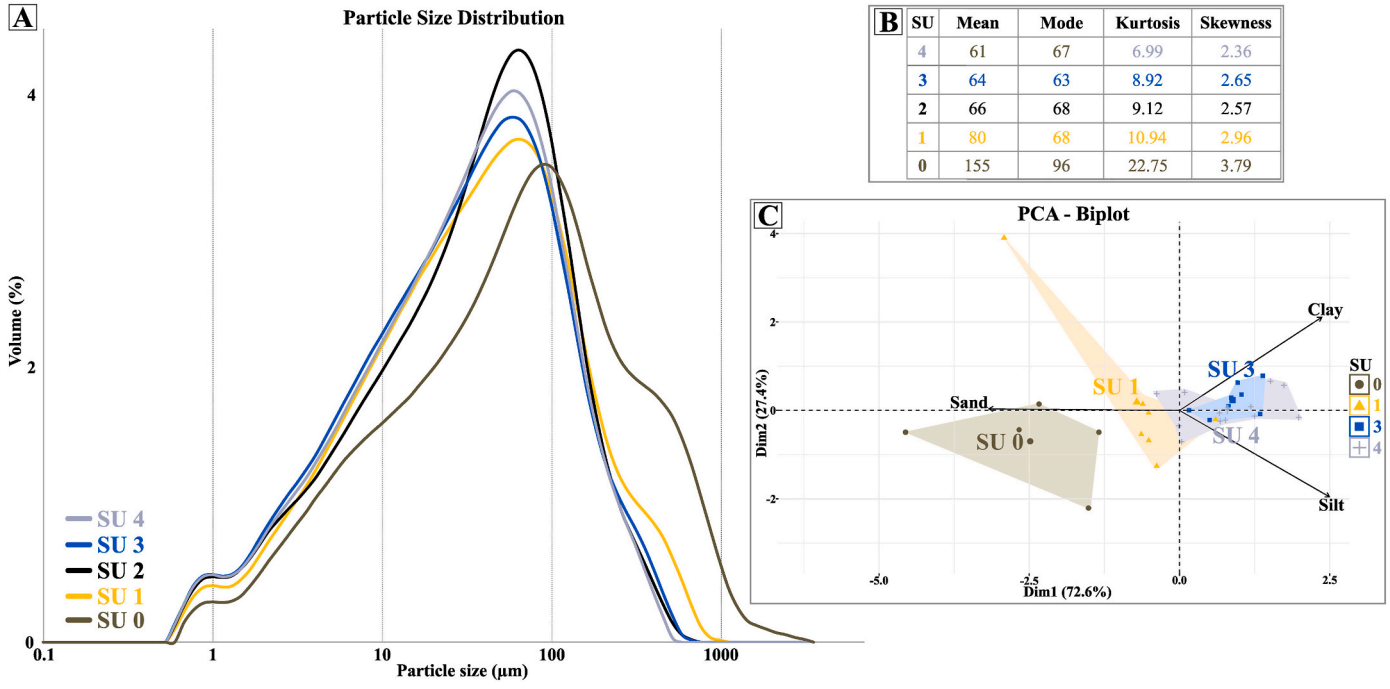

SU	Mean	Mode	Kurtosis	Skewness
4	61	67	6.99	2.36
3	64	63	8.92	2.65
2	66	68	9.12	2.57
1	80	68	10.94	2.96
0	155	96	22.75	3.79

Fig. 3. A-C: A) Particle Size Distribution of representative matrices from the different Sedimentological Units (SU 0–4), plotted as particle size in µm (from 0.1 to 2000 µm) at logarithmic scale vs volume in %. **B)** Table showing mean grain size, mode, kurtosis and skewness values of the samples presented in **A**. Mean and Mode values are in µm. Note: **SU0** = AR22_BSS03; **SU1** = AR22_BSS09; **SU2** = AR22_2A_BS4; **SU3** = AR22_BSS24; **SU4** = AR22_BSS35 (see also **SI.B1**). **C)** Principal Component Analysis (PCA) biplot of CLR (centered log-ratio)-transformed data, visualizing the particle size results from all the samples from the northern profile sample column (sample number 33). PC1 and PC2 explain 72.6 % and 27.4 % of the variance respectively. Sediments from the SU4 and SU3 are grouped within the same region, suggesting textural similarity and separation from the deposits from the SU1 and SU0. These are coarser-grained units, with higher variance, resulting in wider spread.

majority of the samples from the SU4 and SU3 are classified as silt loam, while most of the samples from the SU1 and SU0 are loam (**SI.B1**). This textural change from silt loam-dominated to loam-dominated sediments supports the gradual inverse grading observed at the profile-scale level. Principal Component analysis also shows the vertical changes in grain size composition, showing that PC1 explains ~73 % of the variance, differentiating the texture of the SU0 from the SU1, as well as from the SU3-4 (Fig. 3C). The grouping of the SU3 and SU4 within the same region corresponds with their textural similarities, as both strata contain silty loam sediments.

3.2.2. Particle shape analysis

Samples from the SU1, SU3, and SU4 were selected for the analysis (**SI.B2**). The data shows a population of subangular to subrounded grains with relatively smooth to moderately irregular surfaces and moderate degree of elongation. The average aspect ratio throughout the strata is associated with regular or moderately elongated particles (0.648–0.678; Table 3; Fig. 4B). The mean circularity values are between 0.857 and 0.881 and could possibly be associated with subangular and subrounded forms. The most rounded particles (0.901) are observed in fine sand in the SU4. The SU1 sediments are relatively more angular, with the lowest circularity noted for medium-sized sand (0.810). The average convexity values of 0.963–0.968 indicate relatively smooth particles' surface. However, the coarser grains show higher convexity values, at a range of 0.932–0.937, compared to the finely sand particles with values 9.784–0.984. Therefore, fine sand exhibits slightly rougher edges and more irregular surfaces. The SU4 sediments show the most homogeneous values across aspect ratio, circularity, and convexity (Fig. 4A), indicating a more consistent texture in comparison to the SU3 and SU1. Moreover, the SU4 particles are slightly less elongated and relatively more rounded, when compared to the SU3-1 samples (Table 3; Fig. 4A).

3.2.3. Loss-On-Ignition

On average the $CaCO_3$ content accounts for 33 % of the total sediment weight. The lowest percentage is recorded in SU3.2 at ~28 %, while the highest is noted at the interface between SU1.4 and SU3.1. A clear increase of the calcareous component upwards is observed (Fig. 5A). The SU4 sediments have on average ~30 % of $CaCO_3$, while the percentages of the SU3 is ~34 %. The concentration of $CaCO_3$ is further elevated within the SU1 and 0, equally showing a percentage of ~36 % (**SI.B3**).

The organic matter (OM) varies from 4.8 % (SU4.1) to 16.3 % (SU0.2) and increases upwards (Fig. 5A). The OM at the lowermost SU4 is 5.3 % while the SU3 has a content of 7.5 %. The values of OM in the SU1 and SU0 are ~10.3 % and ~14.2 % respectively (**SI.B4**). As the higher content of OM corresponds to changes in colour, the downprofile decrease in colour lightness is likely related to the decrease in OM content.

3.2.4. Magnetic susceptibility

The mean magnetic susceptibility value of Ararat-1 sediments is $2.9e^{-5}$, while the minimum and maximum values are noted for the SU4.2 and SU1.3, at $1.8e^{-5}$ and $4.5e^{-5}$ respectively (Fig. 5A; **SI.B5**). The lowest mean magnetic susceptibility is recorded at the bottom of SU4 is $2.1e^{-5}$, followed by the uppermost SU0, with a value of $2.9e^{-5}$ (Table 4). The SU3 shows a considerably higher value of $3.5e^{-5}$, but the highest mean susceptibility is noted for the SU1, at $3.9e^{-5}$. The elevation-dependent distribution of the data shows a gradual upwards increase in magnetic values between the SU4.2 and SU1.3 (Northern profile; Fig. 5A), which is followed by a sharp decrease towards the SU0, where the values are nearly equated to the SU4 values.

The highest susceptibility values recorded for sediments within the cave are also associated with tephra deposition (ARAM6 feature/block; Section 3.3.; Table 4). However, their values ($3.5e^{-5}$ and $4.2e^{-5}$) are considerably lower, due to their heterogeneous composition. The presence of reworked (crypto-) tephra throughout most of the sequence (Blockley et al., 2025), especially within the SU3 and SU1, might be responsible for the elevated magnetic susceptibility. The only samples associated with possible combustion remains have low susceptibility values ($2.5e^{-5}$ and $1.9e^{-5}$; ARAM3-4 area; Section 3.3), therefore enhancement of the magnetic signal due to pyrogenic/anthropogenic agents is not evident.

3.2.5. Elemental analyses

Ca, ranging from ~8.5 % to ~12.5 %, is the most dominant element Ararat-1 sediments (Fig. 5B; **SI.B6**), showing upward increase from the SU3. The lowest percentages are within the SU4.1, decreasing from the SU4.2. Al is most abundant within the SU4, exhibiting upward decrease, with lowest percentages reported in the SU0. The Al/Ca ratio shows the highest values for the SU4, which is followed by a drop (SU3.2) and gradual upwards reduction from SU3.1. The Al/Ca ratio of the limestone bedrock of the cave is lower from the one found in the SU4 sediments by two orders of magnitude (Bedrock Al/Ca: ~0.005, SU4 Al/Ca: ~0.50; Table 5). As such, the lower strata contain considerably higher Al-rich minerals compared to those of the SU3, SU1, and SU0, where Ca-rich materials are increasingly more common. Both the Fe (%) and the Mn (ppm) data show an upward decrease, while the highest average values are present in the SU4, at 3.2 % and 882 ppm respectively (similarly Fe/Mn; Fig. 5B; Table 5; **SI.B6**). P broadly increases upwards in a step-like

Table 3
Summary table of the mean aspect ratio, mean circularity and mean convexity values for the entire analysed particle size population, i.e., 63–2000 μm, as well as for the different size classes, i.e., 63–125 μm (very fine sand), 125–250 μm (fine sand), 250–500 μm (medium sand), 500–1000 μm (coarse sand) and 1000–2000 μm (very coarse sand).

	Mean Aspect Ratio					
	63–2000 μm	63–125 μm	125–250 μm	250–500 μm	500–1000 μm	1000–2000 μm
AR_NP_09 (SU1)	0,648	0,661	0,652	0,589	0,670	0,702
AR_NP_16 (SU3)	0,664	0,662	0,680	0,627	0,694	0,716
AR_NP_28 (SU4)	0,678	0,694	0,713	0,645	0,676	0,707
	Mean Circularity					
	63–2000 μm	63–125 μm	125–250 μm	250–500 μm	500–1000 μm	1000–2000 μm
AR_NP_09 (SU1)	0,857	0,874	0,859	0,810	0,862	0,847
AR_NP_16 (SU3)	0,864	0,868	0,867	0,844	0,878	0,863
AR_NP_28 (SU4)	0,881	0,894	0,901	0,871	0,873	0,860
	Mean Convexity					
	63–2000 μm	63–125 μm	125–250 μm	250–500 μm	500–1000 μm	1000–2000 μm
AR_NP_09 (SU1)	0,964	0,979	0,963	0,945	0,946	0,932
AR_NP_16 (SU3)	0,963	0,978	0,963	0,949	0,948	0,937
AR_NP_28 (SU4)	0,968	0,984	0,971	0,958	0,949	0,937

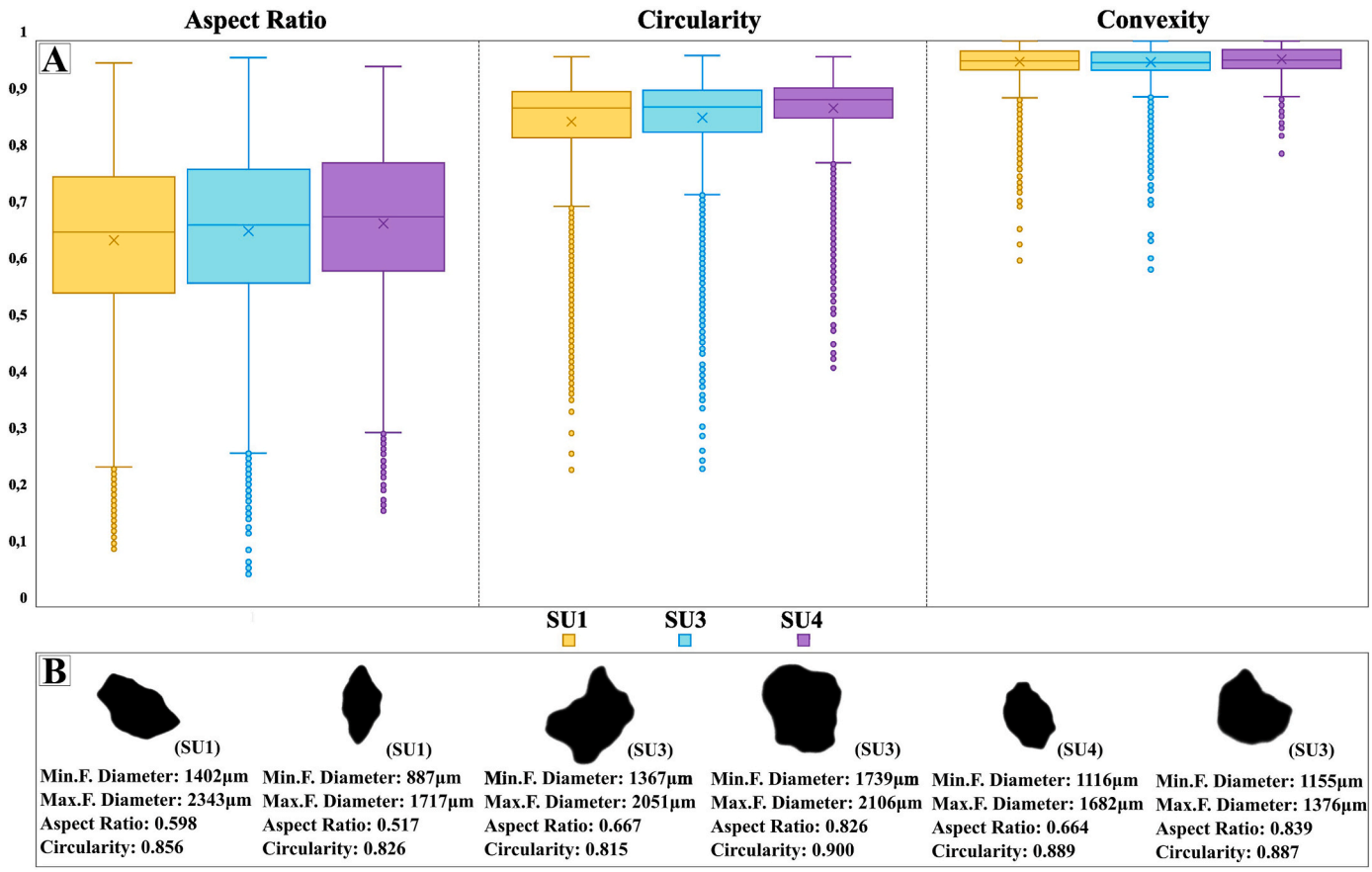

Fig. 4. A-B: **A**) Box and Whishker plots for Aspect Ratio, Circularity and Convexity, per SU: **SU1** (AR_NP_09; 30226 grains), **SU3** (AR_NP_16; 19747 grains), and **SU4** (AR_NP_28; 9210 grains). **B**) Selected individual particles from **SU1**, **SU3** and **SU4**, indicative of the variance in terms of elongation (aspect ratio), roundness (circularity) and edge roughness (convexity).

manner. SU4.2 show average values of 4227 ppm, while SU4.1 values drop to 4032 ppm, following an increase and a plateau between 3.2 and 1.3. Noticeably, the topmost part of the SU0.1 is differentiated, showing a drop in P (4140 ppm; SI.B6). Principal Component Analysis of Al, Ca, Fe, Mn and P shows separation of the lower SU4 from the rest of the strata (SI.B6). More than 90 % of the variance is explained by PC1, illustrating a clear contrast between Ca-rich and Al-rich deposits, suggesting a change in the ratio of autochthonous to allochthonous sediment input.

3.3. Chronology

A summary of luminescence dating results is presented in Table 6 (SI. A2). All OSL results are stratigraphically consistent and increase with depth. However, some discrepancies are noted between OSL ages previously generated for the site by Sherriff et al. (2024) with a particular inversion noted for the SU3. The re-investigation of the cave showed that this sample (age: 45.10 ± 3.0 ka) was collected from a bioturbated locality of the Western Profile. Additionally, the ~8 ka offset between samples taken at similar depths from the SU4 (44.30 ± 2.9 ka at the back of the cave and 37.94 ± 1.67 ka close to the entrance) is likely an indication of spatially heterogenous processes within the cave. Finally, ages point to relatively active sedimentation between 33.40 ± 2.50 (SU1.2) and 37.94 ± 1.67 ka (SU4).

3.4. Micro-archaeological analyses

3.4.1. FTIR results

The sediments of Ararat-1 Cave are primarily composed of calcite and clay minerals and Si-minerals such as quartz and feldspars (Fig. 6). Calcite is usually represented by major absorption at 1430 cm^{-1} and 875 cm^{-1}, while minor calcite peaks at 713 cm^{-1} and 2513 cm^{-1} are also present. Clay minerals are usually represented by major absorbance at 1030 cm^{-1} and 466 cm^{-1}, while the presence of peaks at c. 3690 cm^{-1} and c. 3620 cm^{-1}, at c. 915 cm^{-1}, as well as at c. 525 cm^{-1}, suggests that clays have not been thermally altered. The presence of the shoulders of 1163 cm^{-1} and 1084 cm^{-1} is indicative of SiO_2/Si-mineral contribution. Moreover, quartz is represented by the doublet of 797 cm^{-1} and 779 cm^{-1}, as well as from minor peaks at 513 cm^{-1} and 695 cm^{-1}. Series of minor peaks found within the 700-400 cm^{-1} range, namely 647 cm^{-1}, 635 cm^{-1}, 578 cm^{-1}, and 432 cm^{-1} can be associated with the feldspar groups, which is supported by the micromorphological analyses. However, the major absorption of the feldspars occurs within the 1000-1200 cm^{-1} range, where clay groups are also found, possibly masking the other minerals (see Fig. 6).

Although the FTIR analyses for all the samples from the cave deposits, from the northern profile and from different contexts, show similar compositional, mineralogical patterns (Fig. 6; SI.A3), some strata-specific changes can be observed. First, progressive upwards increase in the matrix calcite content is suggested. The relative absorbance of the latter, within the lower strata and mainly the SU4, appears lower than the clay absorbance, while in the overlaying units it either appears equal or higher. This is supported by the LOI-based $CaCO_3$-estimation (Fig. 5), and the Ca and Al/Ca element results. Second, the presence of organic matter is higher in the upper strata (SU0 and SU1), which might correspond to sodium nitrates and carboxylate groups (absorbance at the ranges of 3400–3700 cm^{-1}, 2900-2800 cm^{-1}, and c. 1600 cm^{-1}). Possible sodium nitrate contamination of the upper strata is shown by

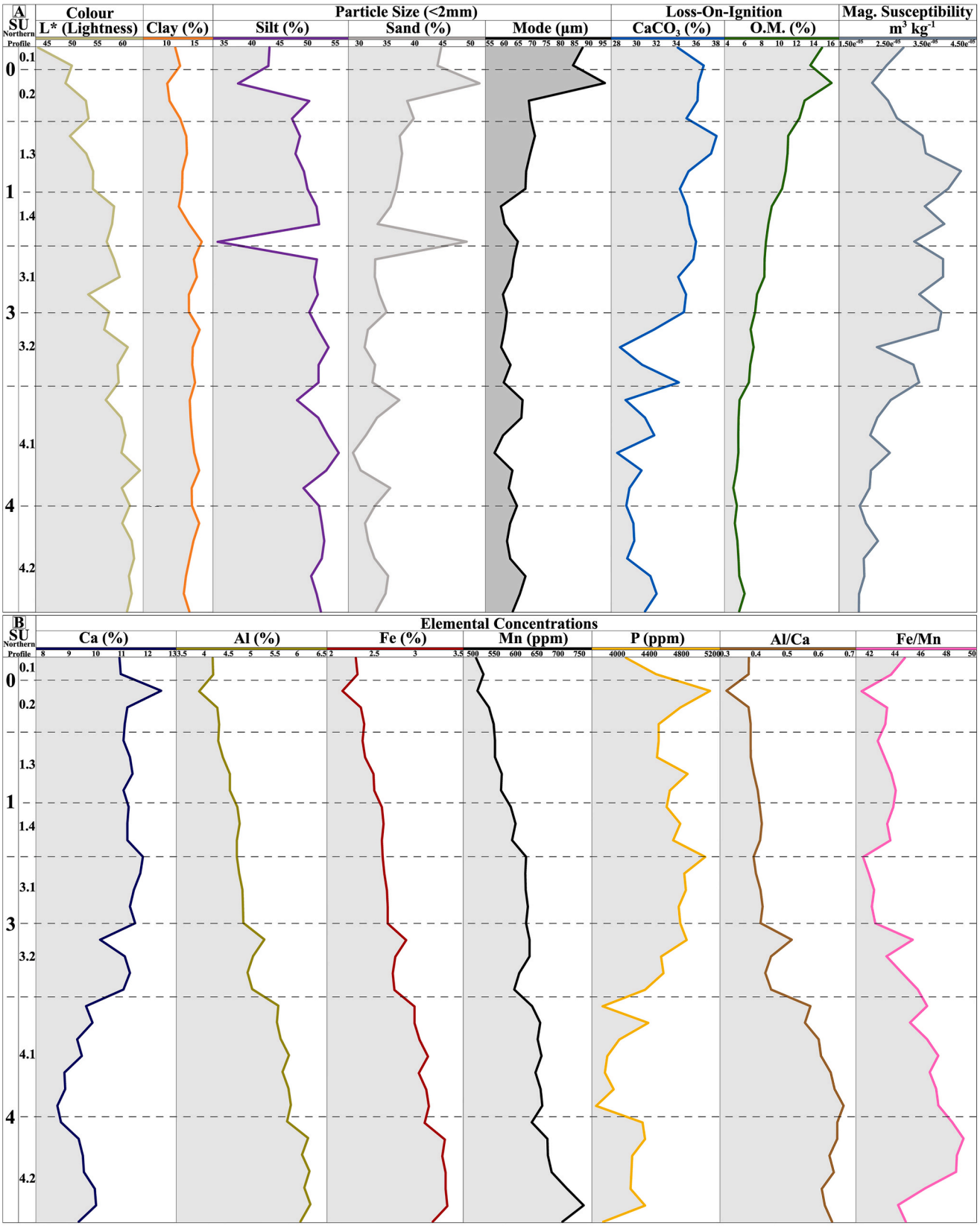

Fig. 5. Graph showing the results of the main bulk sedimentological, magnetic and elemental analyses of the sample sequence from the Northern Profile (Square K14; sampling interval 4 cm), plotted as elevation-dependent, interconnected points (see Fig. 2A; **SI.B1, SI.B3-5**). The relevant Sedimentological Units are shown. **A**) The results include the colour property of lightness* (darker/black to paler/white sediment range), granulometric composition – clay, silt, sand in %volume, estimates of organic matter (OM) and $CaCO_3$ content after Loss-On-Iginition (LOI), and magnetic susceptibility values as e^{-5} m^3 kg^{-1}. **B**) The results include the concentrations of Ca (%), Al (%), Fe (%), Mn (ppm), P (ppm) and the elemental ratios of Al/Ca (Aluminium to Calcium ratio), Fe/Mn (Iron to Manganese ratio; see **SI.B6**).

Table 4
Summary table of the mass-normalised magnetic susceptibility values (χlf) of the different strata and selected contexts. Note that the results shown for the SU0, SU1, SU3, and SU4 are the mean values of a series of samples analysed per SU, coming from the BSS1-35 column: SU0 from BSS1-5, SU1 from BSS6-11, SU3 from BSS12-20 and SU4 from BSS21-35 (see also: **SI.B5**). The rest of the samples come from contexts sampled for micromorphological and other micro-contextual analysis.

Sample ID	Context/SU	χlf (m^3 kg^{-1})
BSS1-5	SU0	$2.9e^{-5}$
BSS6-11	SU1	$3.9e^{-5}$
ARA22.2A.BS4	SU2	$1.8e^{-5}$
BSS12-20	SU3	$3.5e^{-5}$
BSS21-35	SU4	$2.1e^{-5}$
ARAM6	Tephra-rich fine-grained moderately-to-well-sorted laminae (Square J14)	$4.2e^{-5}$
ARAM6	Tephra-rich coarse-grained poorly-sorted laminae (Square J14)	$3.5e^{-5}$
ARAM3	Sediment with possible fire-related matter (Square J14)	$2.5e^{-5}$
ARAM4	Tephra-rich coarse-grained laminae (Square J14)	$1.9e^{-5}$

Table 5
Summary of Al (%), Ca (%), Fe (%), Mn (ppm), P (ppm), and Al/Ca and Fe/Mn ratios from the limestone bedrock of the cave and sediments from the SU4, SU3, SU1, SU0. Except for the Cave Bedrock (single sample), the presented sediment values represent the average of multiple values of a series of samples analysed per SU, coming from the BSS1-35 column: SU0 from BSS1-5, SU1 from BSS6-11, SU3 from BSS12-20 and SU4 from BSS21-35 (see also: **SI.B6**).

	Al (%)	Ca (%)	Al/Ca	Fe (%)	Mn (ppm)	Fe/Mn	P (ppm)
Cave Bedrock	0,2	36,6	0,005	0,2	882	2,7	300
SU4 Sediment	5,9	9,5	0,622	3,2	674	47,0	4123
SU3 Sediment	4,9	11,3	0,436	2,7	630	43,0	4825
SU1 Sediment	4,6	11,3	0,407	2,5	579	43,6	4697
SU0 Sediment	4,2	11,4	0,370	2,3	531	43,4	4644

the prominent absorbance at 1385 cm^{-1}. These observations are consistent with macroscopic evidence of dung and organic matter and by the LOI (OM; Fig. 5), which shows higher organic input within the SU0-1. Rarely, the presence of minor absorbance at 603 cm^{-1} and 565 cm^{-1}, indicative of carbonated hydroxyl apatite, could be attributed to the presence of finely comminuted bone fragments as noted by the micromorphological analyses throughout the sequence.

3.4.2. Dung spherulite and ash pseudomorph quantification

Ararat-1 sequence is relatively rich in dung spherulites (average ~$0.59{\cdot}10^6$ spherulites per g of sediment (sph/g)) in comparison to ash pseudomorphs (Fig. 7; Table 7; **SI.B7**). The highest concentration, at ~$1.56{\cdot}10^6$ sph/g, is found in SU0.1, followed by ~$0.98{\cdot}10^6$ sph/g and ~$0.90{\cdot}10^6$ sph/g in SU4 and SU1 respectively. Conversely, the concentration of ash pseudomorphs per g of sediment (aps/g) is very low. A considerable number of samples collected from SU1 and the interface between SU3 and SU4 did not yield any pseudomorph remains, while, in many cases, the identified particles were often fragmented or poorly-preserved. On average, Ararat-1 sequence contains ~8.2k aps/g, with the highest values of ~60k aps/g and ~17k found within the SU0.1 and SU0.2 respectively. Unheated, 'fresh' calcium oxalates are also reported within these strata. It is noteworthy that the ash pseudomorphs always co-exist with dung spherulites within the samples where they were counted. On the contrary, dung spherulites were identified in all analysed samples, including those that do not contain ash pseudomorphs. No evidence of spherulite heating was recorded.

3.5. Microscopic analyses of thin sections

Ten different microfacies are determined (following the microfacies approach, *sensu* Goldberg and Macphail, 2006; Courty, 2001), based on differences in the (micro-) structure, basic distribution, mineralogical composition, biogenic and anthropogenic inclusions (**SI.A4**). The following notations are used to denote microfacies: **DF** for mass-movement, debris/grain flow-related processes, **WT** for water-lain processes, and **CF** for cementation processes (Table 8). The main microfacies of the SU4 are **DFi-ii**, while **DFab** and **WTi-ii** are present discontinuously within portions of the unit. **Cfi-ii** microfacies are also found within the SU4, but only at localities near the cave bedrock. The microfacies of the overlying SU3 at the cave entrance are **DFiii**, while the SU3 of the internal cave parts share the same **DFiv** microfacies with the SU1.

3.5.1. Sedimentological unit 4

3.5.1.1. Debris flows (DFi-DFii microfacies). **SU4** is dominated by the **DFi** and **DFii** microfacies, which are represented within **ARAM3, ARAM4, ARAM7** and **MM4** thin sections (**SI.A4**). At the meso- and micro-scopic level, they consist of series of obliquely inclined micro-layers, predominantly of moderately-sorted, fine-grained matrices (**DFi**) and less frequently of poorly-sorted, grain- or granule-/gravel-supported units (**DFii;** Fig. 8A-I). The presence of micro-layering, the oriented and obliquely inclined coarse and fine fraction, and the rotational movement features are characteristic elements of these microfacies. **DFi** consists of silt loam, dominated by silt-sized fractions, usually as silty clay micro-aggregates, with various mineral species, including mainly feldspar(s) and micritic $CaCO_3$, but also volcanic pyroclastic material, tephra shards (Fig. 8F), and quartz. The coarser fraction primarily includes limestone fragments, while other dark-coloured volcanic minerals, epidote and pyroxene, are occasionally reported for the sand size-class. **DFii** exhibits loamy texture, with increased sand-sized particles and coarser, granule-sized components of limestone, while containing overall similar mineralogical composition. Common characteristic of both **DFi** and **DFii** is the oriented, slopping distribution, the complex vughy/vesicular micro-structures and the micro-aggregated appearance of the finer fractions. The b-fabric appears both stipple-speckled and calcitic crystallitic, due to the presence of clay/silty clay microaggregates and micritic $CaCO_3$ respectively. Occasional laminae of

Table 6
A summary of the luminescence dating results.

Sample	SU		Depth (m)	Grain size (μm)	n/N	OD (%)	De (Gy)	Total dose rate (Gy ka^{-1})	Age (ka)
AraOSL 1	**2**	**2.D**	0.60	4–11	25/25	0.7	161.1 ± 1.1	4.35 ± 0.17	37.03 ± 1.47
AraOSL 2		**2.E**	0.90	4–11	23/29	0	134.2 ± 1.0	3.17 ± 0.13	42.40 ± 1.79
AraOSL 3	**3**	**3.2**	0.80	4–11	20/20	2.6	147.2 ± 1.9	3.88 ± 0.16	37.90 ± 1.61
AR23_OSL_1	**3**	**3.5 En**	1.60	4–11	20/20	0	161.2 ± 1.2	4.28 ± 0.17	37.70 ± 1.51
AR23_OSL_2	**4**	**4.1 En**	1.96	4–11	20/20	4.4	142.6 ± 1.8	3.76 ± 0.16	37.94 ± 1.67

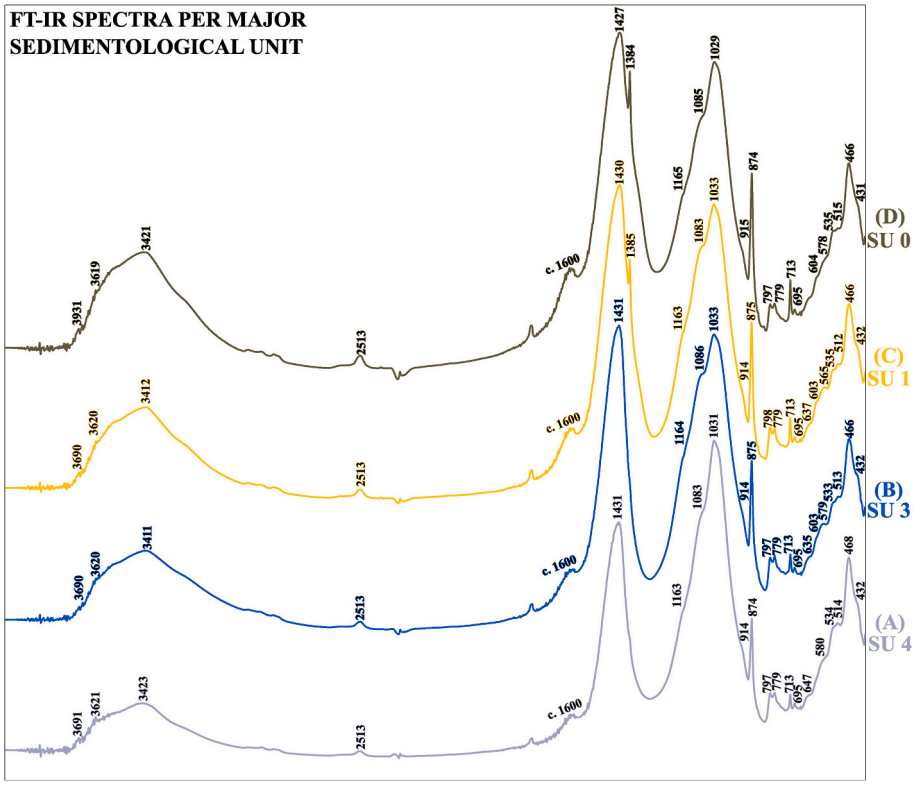

Fig. 6. Selected FT-IR spectra from the four major sedimentological units (from the BSS1-35 column): (**A**) **SU4**, (**B**) **SU3**, (**C**) **SU1**, (**D**) **SU0**. **A**) Spectra from matrix sediment from **SU4**, showing major absorbance at 1031 cm^{-1} and 468, indicative of clay groups, 1431 cm^{-1} and 874 cm^{-1}, indicative of calcite. Minor absorption at 713 cm^{-1} and 2513 cm^{-1} is associated with calcite too. The shoulders of 1083 and 1163 are associated with the presence of SiO_2-minerals, which are noted elsewhere: absorbance at the 797 cm^{-1} and 779 cm^{-1} doublet, as well the minor peaks at 514 cm^{-1} and 695 cm^{-1}, indicative of quartz. Minor absorbance at 432 cm^{-1}, 534 cm^{-1}, 580 cm^{-1}, and 647 cm^{-1} can be associated with the presence of the feldspar group. The absorbance within the >3400 cm^{-1} range, as well as the 914 cm^{-1} peak, indicative of unaltered sediments. The low absorbance within this and the c. 1600 cm^{-1} region suggest low amount of structural water and/or carboxylate matter. Note the higher relative absorbance of the clay/silicate component, compared to calcite. **B**) Spectra from matrix sediment from **SU3**, showing major absorbance at 1033 cm^{-1} and 466, indicative of clay groups, 1431 cm^{-1} and 875 cm^{-1}, indicative of calcite. The shoulders of 1086 cm^{-1} and 1163 cm^{-1}, associated with the presence of SiO_2-minerals, appear slightly more pronounced. Minor absorbance at 432 cm^{-1}, 533 cm^{-1}, 579 cm^{-1}, 635 cm^{-1} is associated with the presence of the feldspar group, while absorbance at 603 cm^{-1} could be related to minor contribution of hydroxylapatite (bone). Note the increased relative absorbance in the major calcite peak, as well as the slightly elevated absorption at the >3400 cm^{-1} range. **C**) Spectra from matrix sediment from **SU1**, similar to **B**. Calcite major peak at 1430 cm^{-1} is higher than the clay major peak at 1330 cm^{-1}. Note the presence of absorbance at 1385 cm^{-1}, related to sodium nitrate contribution from organic matter decay. **D**) Spectra from matrix sediment from **SU0**, similar to **C**. The absorbance at the <3400 cm^{-1} range is the highest of all samples, while the peaks associated with organic matter contribution (i.e., c. 1600 cm^{-1} range, 1385 cm^{-1}) appear more pronounced. The peaks that could be associated with the feldspar group are slightly diminished and faded (i.e., 432, 535, 577 cm^{-1}).

well-sorted silty sediments are also reported within these microfacies (Fig. 8J).

P-rich/apatite nodules, micritic $CaCO_3$ infillings and nodules, dendritic and orthic Mn-/Fe-oxide nodules are common features of the **DFi-ii** microfacies (e.g., Fig. 8D-E, G-H). The bone fragments often exhibit microbially-induced degradation traces, resulting in high concentrations of dendritic Mn-/Fe-oxide staining on their external surface (Fig. 8K). In localities with higher $CaCO_3$ impregnation and cementation, bone fractures, haversian canals and pores are infilled with calcite (Fig. 8L-M). Fragmented, decaying excretory products are commonly found floating throughout the **SU4**, as well as micro-fauna bone pieces. Few localities within the **DFi-ii** structures document the presence of anthropogenic, as well as biogenic contributions, and are described separately as separate microfacies (**DFab,** see Section 3.3.1.2).

The presence of phosphorous in the **SU4** and the **DFi-ii** microfacies is associated with the coprolitic and bone content. Traces of bat guano are absent. The matrices occasionally appear impregnated with phosphatic matter, through the decomposition and redistribution of the coprolitic component (Fig. 9A; **ARAM3**). Subrounded to subangular carbonated apatite nodules are also present. P-rich precipitates are detected within limestone gravel fractures (Fig. 9B-C). Concentrations of amorphous or subangular/subrounded nodular calcium phosphates with yellow colours in PPL and yellow, weakly birefringent appearance in XPL are found at the deeper parts of the sequence (Fig. 9G-H). The SEM-EDS elemental mapping confirms the presence of concentrations of Ca and P, while the targeted elemental probing shows the non-stoichiometric character of this authigenic neoformation (Fig. 9I; **SI.A5**). Calcium phosphates are also found within limestone fractures. They also replace recrystallized sparitic limestone rims and neo-form pendants (Fig. 9D-F). Partially phosphatised, weakly isotropic micritic pendants and phosphocalcitic nodules are also reported.

3.5.1.2. Debris flow with anthropogenic and biogenic component (DFab). **DFab** microfacies are defined as **DFi-ii** areas with anthropogenic components and features (**ARAM3-4**; Fig. 10A), situated with **SU4**. These microfacies appear fragmented, scarce and preserved in few patches/lenses, usually within moderately cemented areas. **DFab** is associated with the presence of macro- and micro-charcoal pieces, often micro-comminuted or as dotted and speckled patterns in the matrices (Fig. 10B-C). These localities have matrices with high micritic $CaCO_3$ content, and are often compacted, with dark to pale grey or slightly brownish grey colours and cloudy appearance (Fig. 10C-D). Occasionally, large mm-sized angular aggregates of calcite are reported (Fig. 10E). These aggregates often preserve rectangular/rhomboid ash

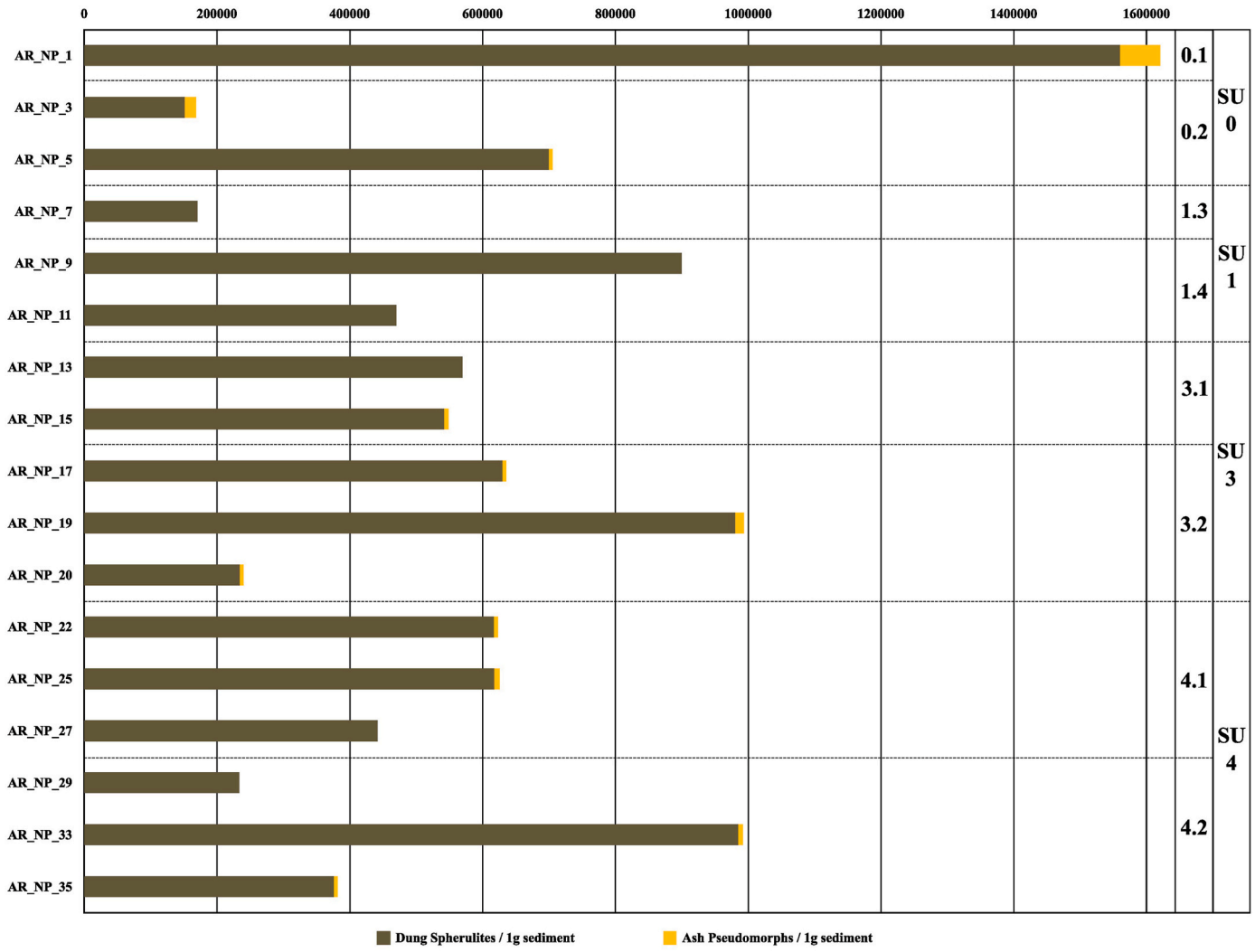

Fig. 7. Stacked bar chart of dung spherulite and ash pseudomorph concentration per gr of sediment. The sample IDs and the relevant Sedimentological Units (SU) and sub-units are labelled at the right and the left part of the plot respectively.

Table 7
Concentration of dung spherulites and ash pseudomorphs per 1 g of sediment (integer values), followed by the respective error (±30 %). Values are shown in mil/g (10^6).

Sample ID	SU		Dung Spherulites/g sediment (10^6)	±30 % error	Ash Pseudomorphs/g sediment (10^6)	±30 % error
AR_NP_1	**SU0**	**0.1**	1.560	0.468	0.060	0.018
AR_NP_3		**0.2**	0.152	0.045	0.017	0.005
AR_NP_5			0.700	0.210	0.006	0.002
AR_NP_7	**SU1**	**1.3**	0.171	0.051	0	0
AR_NP_9		**1.4**	0.900	0.270	0	0
AR_NP_11			0.470	0.141	0	0
AR_NP_13	**SU3**	**3.1**	0.570	0.171	0	0
AR_NP_15			0.542	0.163	0.006	0.002
AR_NP_17		**3.2**	0.630	0.190	0.006	0.002
AR_NP_19			0.980	0.294	0.013	0.004
AR_NP_20			0.233	0.070	0.005	0.002
AR_NP_22	**SU4**	**4.1**	0.617	0.185	0.006	0.002
AR_NP_25			0.617	0.185	0.008	0.002
AR_NP_27			0.442	0.133	0	0
AR_NP_29		**4.2**	0.234	0.700	0	0
AR_NP_33			0.985	0.295	0.007	0.002
AR_NP_35			0.376	0.113	0.006	0.002

pseudomorphs after calcium oxalates and appear in close spatial relationship to (micro-) charcoal fragments. Charred and uncharred mm-to μm-sized bone fragments are reported at a 10:90 ratio (Fig. 10F-G). The former exhibits brownish red/reddish brown colours in PPL and reddish colours in XPL, suggesting a sub-500 °C heating (Villagran et al., 2017). Fibrous, oxidised organic/plant matter is also found impregnated in the matrix, but opaline phytoliths are very rarely observed. Such materials and features are associated with anthropogenic combustion processes. Except for a single possibly knapped lithic fragment (Fig. 10H), lithic artefacts remain largely undetected by the micromorphological analyses.

The anthropogenic matter is found in close micro-contextual association with non-anthropogenic excretory products (Fig. 10A: micro-layers **I** and **II**), as they appear roughly interspersed in the same localities. The underlying and overlying micro-layers are rich in faecal matter, while the latter can be divided into two broad categories. The first group is attributed to carnivorous animal agents and it consists of large isotropic (XPL) to pale yellow, yellowish grey masses that incorporate small, μm- or few mm-sized digested bone fragments (Fig. 10I-N). They range from subrounded to subangular μm- or mm-sized coprolitic fragments to subrounded cm-sized coprolites. The coprolitic matrices are usually covered with dendritic Mn stains, while reddening due to Fe-oxidisation is sometimes documented for their external surfaces. The larger coprolites overlaying the anthropogenic units show traces of *quasi*

Table 8
Correlation between sedimentological units, identified microfacies and their interpretation. The location of the samples can be seen in Fig. 2 (for additional micromorphological descriptions, see **SI.A4**).

Sedimentological Unit		Microfacies	Interpretation	Sample
SU4	**SU4.2/ SU4.1**	**DFi/DFii**	Loess-rich (**DFi**) to *éboulis*-rich (**DFii**) Debris Flow	ARAM3; ARAM4; ARAM5; ARAM6; MM4
		DFab	Debris Flow Deposits with Anthropogenic Combustion Residues and Coprolitic Material	ARAM3; ARAM4;
		CFi/CFii	Well- (**CFi**) to Moderately-Developed (**DFii**) Karstic-Induced Cemented Deposits	ARAM2; ARAM3
		WTi/WTii	Low-Energy (**WTi**) to High-Energy (**WTii**) Water-Induced Tephra/ Pyroclastic material Deposits	ARAM5; ARAM6
SU3En	**SU3.1–3.3/ SU3.5En**	**DFiii**	Debris Flow with two distinct fabrics of aeolian origin	ARAM1; ARAM8
SU3/ SU1	**SU3.2 SU1.1/ SU1.2**	**DFiv**	(Bioturbated) Grain Flow Deposits	MM3 MM1; MM2

in situ degradation and fragmentation of the internal structure to finer subangular pieces. The second group of excretory products consists of micro-remains that preserve calcitic dung spherulites, indicative of herbivorous fauna agents (Fig. 10O). This material is isotropic in XPL and yellow to orangish yellow in PPL, with subrounded shapes of few hundreds of μm. Both categories within **DFab** are present in high percentages, up to 30 %, with the herbivore-related component being less frequent, while the anthropogenic component takes no more than 10 % (in **ARAM3**).

3.5.1.3. Water-induced tephra/pyroclastic material deposits (WTi-ii). The laminar features of dark brown silty laminae interbedded with sandy units (**LFa-b**; Table 1), found macroscopically within localities of the **SU4.1**–**2** (**ARAM5**) and **SU4.2** (**ARAM6**), can be divided into two rhythmically alternated microfacies, **WTi** and **WTii** (Fig. 11A-C). The contact from **WTii** to **WTi** is gradual, showing positive grading from the coarse-grained **WTii** cycles to the fine-grained **WTi** laminae. Usually, the laminae are curved and parallel to each other, while planar or semi-horizonal laminae are also reported. Occasional wedging and interbedded laminae are also recorded.

WTi microfacies consist of silt loam/silt textures, including c. 80 %, or more, of silt-sized grains, 10–20 % of clay, while sand particles are very rare. Most of the mineralogical component consists of allochthonous subrounded micro-aggregates (originally aeolian), followed by minor contribution by feldspars and volcanic tephra shards (Fig. 11I). These microfacies exhibits a 5:95 C/F ratio, monic to open porphyric distribution, and are deposited following oriented, banded patterns. These laminar units have planar microstructures and are dominated by planar voids, while rare vesicles are also present, summing to a total of 10–15 % porosity. Occasional micro-remains of decaying vegetal matter, as well as Mn-/Fe-oxide orthic and dendritic nodules are also documented. **WTii** is composed of poorly-sorted loamy sediments, dominated by sand- and silt-sized minerals at c. 45 % and c. 40 % respectively, followed by clay at c. 15 % (Fig. 11D-E). The sand fraction is primarily dominated by angular volcanic pyroclastic materials, tephra shards and feldspar grains. The mineralogical composition of **WTii** appears heterogeneous in some localities, represented by angular volcanic tephra shards, feldspars, quartz, limestone fragments, as well as non-mineral components, such as bone fragments and coprolitic matter (Fig. 11G-H). These microfacies show a CF ratio of 45:55 with open porphyric, locally single-spaced enaulic, distribution and oriented, banded deposition pattern. The porosity rises up to c. 30 % and is mostly expressed by the presence of vesicles and vughs. Orthic and dendritic Fe-/Mn-oxide, as well as micritic $CaCO_3$ nodules, are present in low percentages.

WTi and **WTii** deposits contain significant contribution of volcanic tephra or other finely-sized volcanoclastic fragments, often up to 30 %. The vast majority of this material consists of angular dark brown/reddish brown (PPL) to black (XPL) silica-composed shards with high density of feldspar micro-phenocrysts (Fig. 11D-F). Platy and cuspate shards without microlites, as well as shards with micro-vesicles, are detected in lower amounts. Y-shaped tephra shards are occasionally reported within these microfacies. In terms of shape, pyroclastic particles and tephra shards tend to be very angular, exhibiting minimal weathering. The chemical mapping of **WTi** and **WTii** microfacies confirms the dominance of elements/minerals of allochthonous origins, mainly Si, as well as Al, Na, K, while Ca and autochthonous $CaCO_3$-composed minerals are scarcer (Fig. 11J). These laminar features often appear deformed due to water dripping, compression under water-saturated conditions, as well as mechanical break-up, due to bioturbation and impact from the overlying deposits (Fig. 11K-L).

3.5.1.4. Cemented deposits (CFi-ii). Cemented sediments are not very common. These are found only within the **SU4** and, generally, close to the bedrock and/or dripline, and can be divided into: well-cemented microfacies – **Cfi** and moderately-cemented microfacies – **Cfii** (Fig. 12A-C). The former is characterised by moderately-to-poorly-sorted silt loam, following an open porphyric c/f-related distribution, dominated by silt-/micritic-sized $CaCO_3$ and complex, vesicular to vughy microstructure, with porosity up to 15 %. Its b-facric is calcitic crystallitic, while the most common pedofeatures include micritic and, occasionally, microsparitic $CaCO_3$ hypo-coatings, nodules and infillings, as well as dendritic Mn-/Fe-oxide staining (Fig. 12D-G). The main difference between the **CFi** and the **CFii** microfacies is the slightly diminished and moderately-to-poorly-sorted silt/micritic $CaCO_3$ content, the higher representation of non-authigenic material, including feldspar and quartz sand, bone and plant matter, as well as the presence of calcified root remains. The microstructure of the latter is also complex, vughy to vesicular, but with granular areas and porosity percentage at c. 20 %. Relicts of compacted laminar crusts composed exclusively of micritic $CaCO_3$, grains with micritic/silty coatings and pendants, as well as other speleothem fragments are also reported in localities within the **SU4**.

3.5.2. Sedimentological unit 3 (cave entrance)

3.5.2.1. Debris flows (DFiii). **DFiii** sediments (**ARAM1**; **ARAM7**) are present only within the **SU3** near the cave entrance. They are characterised by the presence of massive structure and slightly obliquely oriented coarse component (Fig. 13A, E). Distinctive element of the **DFiii** microfacies, compared to the rest **DF** microfacies, is the co-existence of two different fine-grained matrices (hence **fabric 1** and **2**; Fig. 13B-C). **Fabric 1** is represented by large, often subrounded peds/aggregates of silt loam, with higher percentages of clay compared to **Fabric 2**. It is dominated by silt at 55–60 %, followed by sand at c. 20 %, and clay at c. 15–20 %, with characteristic yellowish orange/orange colours (PPL and XPL). The b-fabric is calcitic crystallitic and stipple speckled. Sesquioxides, especially Fe-oxides, are present within the matrix as impregnative nodules. These peds often appear aggregated with the limestone granules/gravels. The latter are usually coated with pedogenic, $CaCO_3$-rich, dirty silty/silty clay pendants that exhibit internal undulated micro-laminar structures (Fig. 13F). The peds/aggregates appear floating within **Fabric 2** sediments, often separated by large channels (Fig. 13B-C). **Fabric 2** consists of clay-poor silt loam sediments, dominated by silt at 65–70 %, sand at 25–30 % and clay at <5 %. It is characterised by complex, channel to vughy microstructures, the

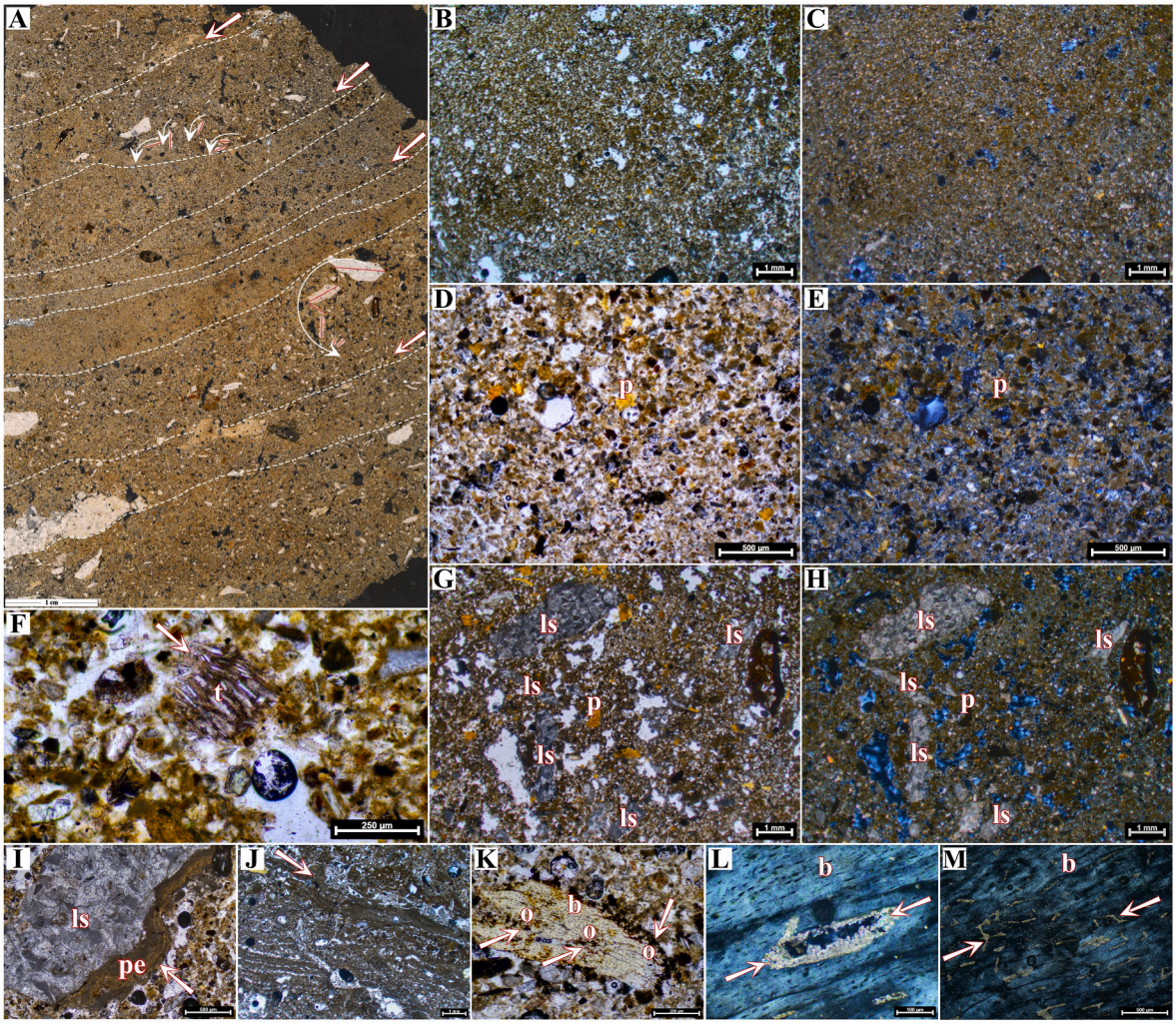

Fig. 8. Thin section scan and photomicrographs from **SU4** (**DFi-ii** microfacies). **A**) **ARAM4B** thin section scan, showing micro-layering of alternating fine-grained, loessic deposits (**DFi**) and mixed loessic deposits with granule- and sand-sized limestone (**DFii**). Note the slopping orientation and the presence of rotational features (**arrows**), indicative of debris flow deposition (XPL, scale = 1 cm). **B**) Fine-grained, loessic matrix (**DFi**) with discrete lens of oriented, compacted, silty sediment from **ARAM4B** (PPL, scale = 1 mm). **C**) Same, in XPL. **D**) Zoomed-in view of the fine-grained units (**DFi; ARAM4B**). Note the presence of micro-aggregated silt and silty clay, feldspar and quartz finely-/very finely-sized sand, and yellowish/orange coprolitic (**p**) nodules (PPL, scale = 500 µm). **E**) Same, in XPL. The coprolitic nodules (**p**) appear isotropic. **F**) Dark reddish brown pyroclastic shard (**t**) with high density of feldspar micro-phenocrysts, within silty matrix, from **ARAM4B** (PPL, scale = 250 µm). **G**) Coarser-grained units (**DFii**) with angular, elongated granules and very coarse/coarse sand of limestone *éboulis* (**ls**). This locality shows increased amount of yellowish/orange coprolitic (**p**) nodules (PPL, scale = 1 mm). **H**) Same, in XPL. Note the isotropy of the coprolitic nodules (**p**). **I**) Granule-sized limestone *éboulis* (**ls**) with micro-laminated $CaCO_3$-rich, silty/clayey silt pendant (**pe**), from **ARAM4**. Presence of minor phosphatic content among the micro-laminae is noted (PPL, scale = 500 µm). **J**) Well-sorted silty laminae, within the debris flow units (**DFi-ii**), demonstrating inclined deposition of sediment through overland runoff, from **ARAM3D** (PPL, scale = 1 mm). **K**) Bone fragment with extensive sesquioxide stains (**o**), along the outer zone and within its core from **ARAM5C**. Both dendritic nodules of Mn- and Fe-oxides are present, mainly due to bio-erosion (PPL, scale = 250 µm). **L**) $CaCO_3$-infilled bone fragment haversian canal, from **ARAM4A** (XPL, scale = 100 µm). **M**) $CaCO_3$-infilled bone fragment fractures and pores, from **ARAM4A** (XPL, scale = 500 µm).

presence of calcitic crystallitic b-fabric and the relative absence of sesquioxides, in comparison to **Fabric 1**. Common element of both fabrics is the presence of micro-aggregates and subrounded mineral grains, with shape possibly indicative of eolian saltation and/or rolling (Fig. 13D; Boschian, 1997). Biogenic component, such as bone fragments and opaline phytoliths, are reported at low percentages for both matrices, while no anthropogenic matter has been documented. Extensive Fe-oxide staining and weak phosphatisation of the bone fragments is noted (Fig. 13G-H).

3.5.3. *Sedimentological units 3 and 1 (cave interior)*

3.5.3.1. Bioturbated grain flows (DFiv). **DFiv** are massive, poorly-sorted to unsorted deposits, of silt loam and granule-/gravel-sized limestone fragments (Fig. 14), found throughout both the **SU3** (**MM3**) and **SU1** (**MM2**; **MM1**). The matrix is dominated by silt-sized grains at c. 50–55 %, often as subrounded loessic micro-aggregates of silt/clayey silt (Fig. 14A-B, E), with micritic $CaCO_3$ and volcanic tephra shards (occasionally silt-sized). Sand represents c. 30 % of the distribution and consists primarily of feldspar, limestone fragments, and less of volcanic tephra shards and quartz. The clay-sized fraction, at 15–20 %, is usually incorporated within micro-aggregates of clayey silt. Opposed to the **DFi-ii** microfacies, **DFiv** do not exhibit clear micro-layering or consistent semi-horizontal/slope orientation of the coarse and fine fraction. Instead, the basic distribution patterns appear random, while both fine and coarse fractions appear turbated. The microstructure is massive and complex, vughy-to-vesicular, but in localities the presence of planar cracks creates blocky ped structures. The porosity ranges from c. 5 to c. 15 %. The presence of infilled micro-fauna/earthworm-induced micro-burrows and channels, usually infilled with reworked matrices, is very

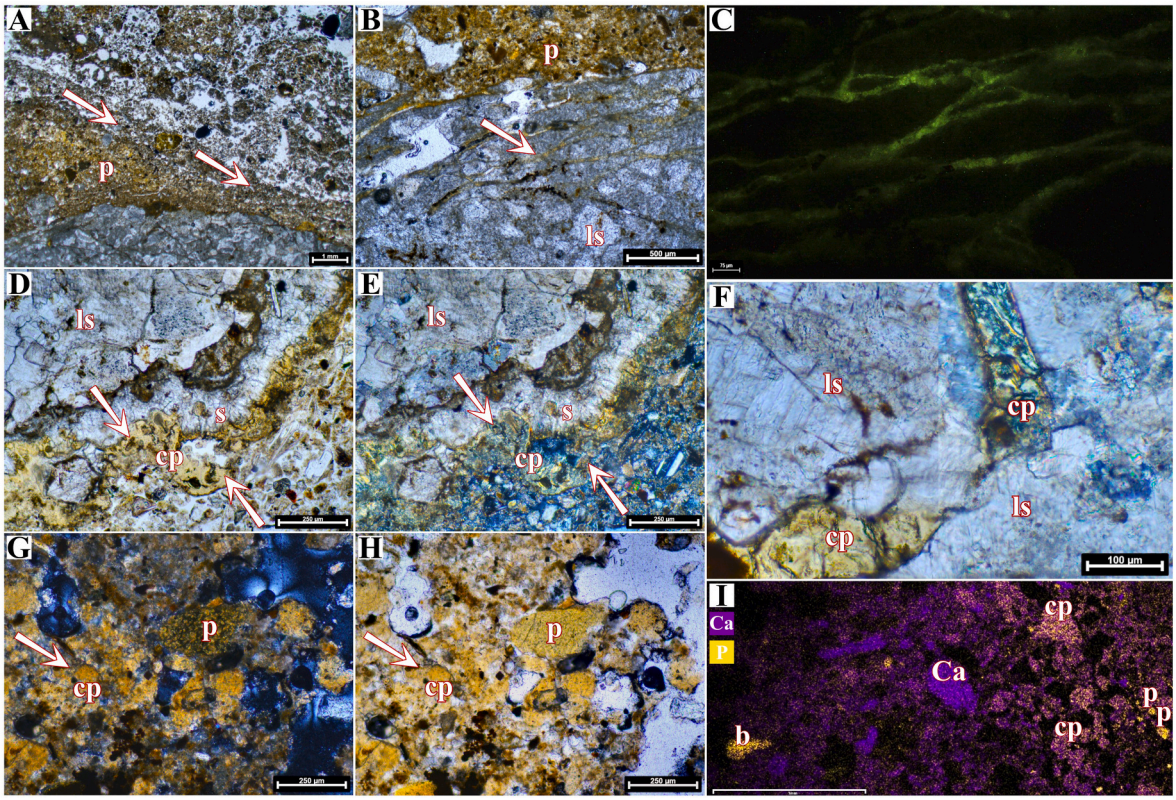

Fig. 9. Thin section scan and photomicrographs from **SU4** (**DFi-ii** and **DFab** microfacies). **A**) Phosphorus-rich matrix (**p**), due to the presence of fauna-induced faecal matter, from **ARAM3A**. It is overlain by waterflow feature; the latter assists into the translocation of phosphorus downprofile (PPL, scale = 1 mm). **B**) Limestone gravel fractures (**ls**) infilled with phosphorus-rich precipitate (**arrows**) and Mn-oxide stains, from **ARAM3A** (PPL, scale = 500 μm). **C**) Same feature, showing the enhanced autofluorescence of the phosphorus-enriched limestone cracks (BLF, scale = 75 μm). **D**) Undulating/amorphous calcium phosphate pendant (**cp**), formed along a recrystallized, sparitic pendant (**s**) of a limestone gravel (**ls**), from **MM4** (PPL, scale = 250 μm). **E**) Same feature, in XPL, partially isotropic, showing weak birefringence. **F**) Calcium phosphate (**cp**) neoformation within limestone fracture (**ls**), from **MM4** (PPL – left and XPL – right, scale = 100 μm). Note the partial isotropy and weak birefringence in XPL. **G**) Subangular to subrounded nodules of calcium phosphate with characteristic yellow, weakly birefringent colour, from **ARAM3B**; occasionally weakly isotropic. Note the presence of coprolitic (**p**) matter (XPL, scale = 250 μm). **H**) Same feature, in PPL; the calcium phosphate is indistinguishable from coprolitic fragments under such lighting conditions. **I**) SEM-EDS elemental mapping of **P** (**yellow**) and **Ca** (**purple**), clearly separating purely Ca-based matter (**Ca**), bone fragments (**b**), coprolitic remains (**p**) and calcium phosphates (**cp**; see nodules **G-H**; also **SI.A5**). The presence of non-stoichiometric calcium phosphate is consistent with weak, early phases of P-induced diagenetic processes.

common within **DFiv** sediments (Fig. 14C-D). Calcified root remains, Mn-/Fe-oxide typic and dendritic nodules, as well as micritic $CaCO_3$ nodules, micro-laminated dusty $CaCO_3$ cappings and crusts, and subrounded/subangular phosphocalcitic nodules are pedofeatures occasionally observed. Micro-comminuted fibrous plant matter and vegetal tissues with silica skeletons/phytoliths, subangular coprolitic/apatite nodules and bone fragments constitute most of the biogenic component (Fig. 14F). Portion of the fresh-/recent-looking plant matter is often associated with herbivorous excretory products. Subangular nodules of coprolitic matter, of possible carnivorous animal origin, also exist. Bone and shell fragments (only from **SU1**), representing 2–5 % and <2 % respectively, constitute the remaining components of the biogenic inclusions (Fig. 14G).

Distinctive element of the **DFiv** microfacies is the scarcity of anthropogenic input. Only a single fragment of heated bone, reported within **MM2** and a large, partially humified and fractured piece of charcoal (max. diameter c. 4.5 mm; Sherriff et al., 2024) are reported. Although more materials, such as unheated bone and shell fragments could be included within the anthropogenic component, the extensive bioturbation and the lack of cohesive fabric organization and structure restricts the latter within the sphere of non-anthropogenic, biogenic deposition. The scarcity of anthropogenic matter, the lack of ash-related concentrations, the absence of cementation and the randomly oriented distribution differentiates the **DFiv** and **SU3-1** from the **SU4** and its microfacies.

4. Discussion

4.1. Site formation processes

The results of this study show that the sedimentary sequence from Ararat-1 Cave is formed via series of mechanisms, including geogenic, biogenic, and anthropogenic depositional processes, and was also altered by post-depositional agents. These will be discussed in detail below.

4.1.1. Geogenic

4.1.1.1. Mass movement processes and material origin. The deposition of the Ararat-1 sediments can be primarily described in terms of mass movement (including rockfall/*éboulis* free fall, talus and debris cone formation, debris flows and grain flows), which is strongly influenced by topographical features of the cave and its setting (Figs. 1 and 15). The mechanical fracturing of the steep limestone cliff above the cave entrance results into rockfall episodes forming a debris talus that extends towards the floodplain. The uppermost part of the talus, situated at the entrance and directly under the rockface, functions as a debris cone with gentle slopes towards the cave interior. The debris cone, along with rockfall, windblown material, and precipitation, delivers debris and sediments to the main chamber of the cave. The deposition of debris and grain flows is further influenced by the downward inclination of the cave

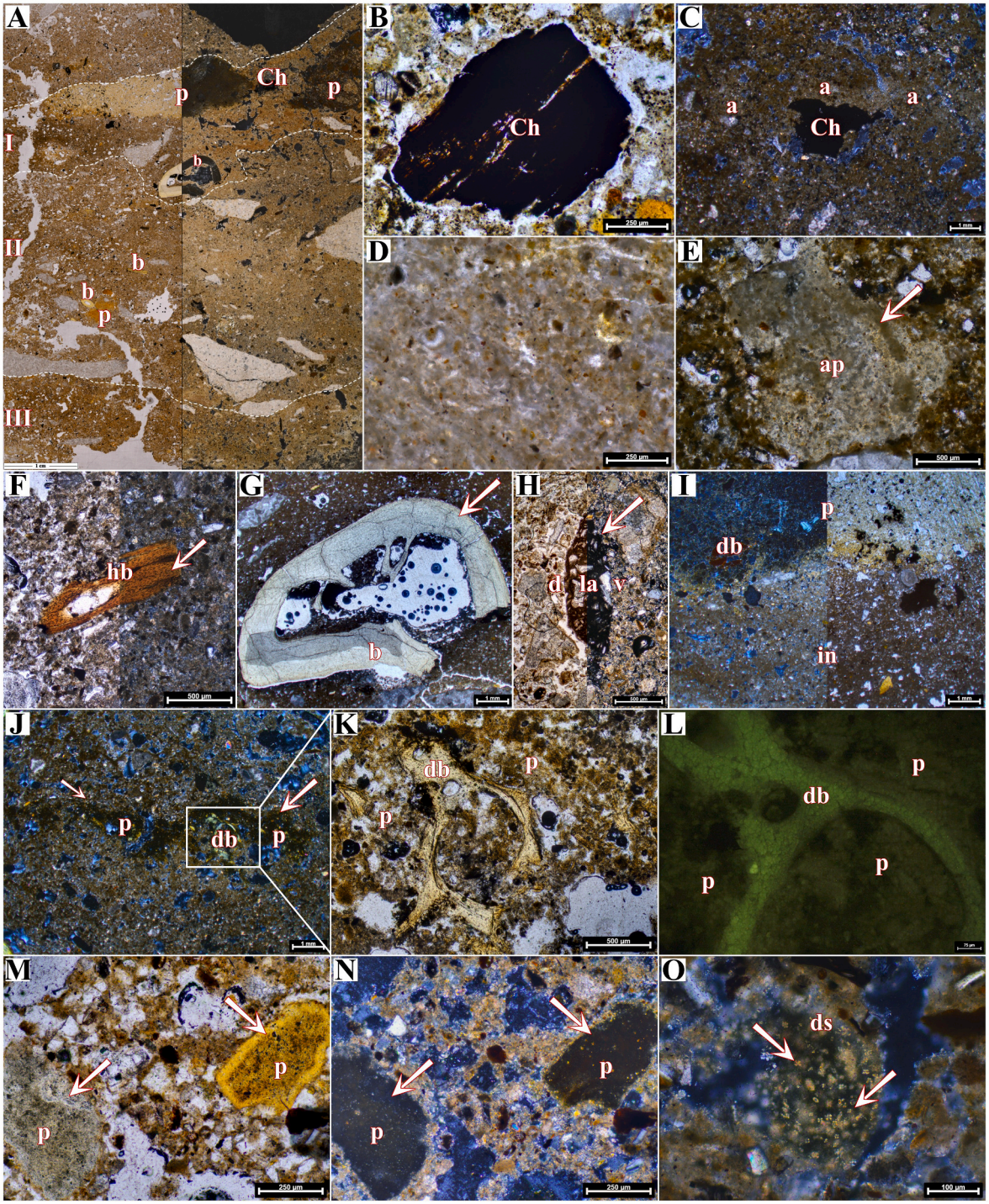

(caption on next page)

Fig. 10. Thin section scan and photomicrographs from **SU4** (**DFab** microfacies). **A**) **ARAM3B** thin section scan in PPL (left) and XPL (right). The lower part (**III**) contains coprolitic fragments and nodules of calcium phosphate neoformations (see Fig. 9). The middle area (**II**) includes coprolitic fragments (**p**), bone pieces (**b**), and scarce anthropogenic material. The upper unit (**I**) is calcite-indurated, it includes anthropogenic residues of combustion-related origin, such as charcoal (**ch**), and it is overlain by large masses of degrading carnivorous coprolitic (**p**) matter (scale = 1 cm). **B**) Charcoal fragment (c. 800 μm max. diameter) with slightly humified areas observed within its fractures, from **ARAM4A** (PPL, scale = 250 μm). **C**) Large charcoal fragment (**ch**; c. 2.4 mm max. diameter) embedded within $CaCO_3$-rich, grey/dark brownish grey ashy sediment (**a**), micro-charcoal speckled matrix, from **ARAM3C** (XPL, scale = 1 mm). **D**) Greyish calcitic ash remains with cloudy, convoluted patterns and occasional micro-charcoal speckling, within ash aggregate, from **ARAM3B** (PPL, scale = 250 μm). **E**) Subangular aggregate preserving pale to dark grey ashes, including calcitic ash pseudomorphs after calcium oxalates (**ap**), from **ARAM3C** (PPL, scale = 500 μm). **F**) Charred bone fragment (max. diameter c. 1.1 mm) with orange-red colours, from ARAM3C (PPL – left and XPL – right, scale = 500 μm). **G**) Large uncharred bone fragment (**b**; max. diameter c. 8 mm) within the indurated deposits, from **ARAM3B** (PPL, scale = 1 mm). **H**) Angular, sand-sized (c. 1400 μm x c. 450 μm) micro-flake (**lf**; see Angelucci, 2017; Angelucci and Zilhão, 2009; Courty, 2001) made of intermediate volcanic rock (possibly dacite; note the dominance of plagioclase feldspars and glassy texture; amphibole/pyroxene also reported), with prominent/sharp boundaries and regular surface roughness. The right side of the possible lithic artefact is slightly curved, potentially corresponding to the ventral face (**v**), while the left side exhibits clearly defined corners, likely representing the dorsal (**d**) face (PPL – left and XPL – right, scale = 500 μm). **I**) Coprolitic mass of carnivorous agents (**p**), containing digested bone micro-fragments (**db**), in direct contact/overlain the indurated deposits (**in**), from **ARAM3B** (XPL – left and PPL – right). **J**) Degraded coprolite of carnivorous animal (**p**), containing micro-fragments of digested bone (**db**), from **ARAM3C** (XPL, scale = 1 mm). **K**) Zoomed-in view of feature from photomicrograph **J**: digested bone fragments (**db**) embedded within coprolitic (**p**) mass, from **ARAM3C** (PPL, scale = 500 μm). **L**) The upper part of the same feature (BLF, scale = 75 μm). The bone fragments (**db**) show stronger autofluorescence compared to the coprolitic matrix (**p**). **M**) Pale greyish beige (left) and yellow (right) phosphatic/coprolitic nodules (**p**), from **ARAM4A** (PPL, scale = 250 μm). **N**) Same as **M**, in XPL, showing differential isotropy patterns. **O**) Excretion rich in dung spherulites (**ds**), attributed to herbivorous agents, from **ARAM4B** (XPL, scale = 100 μm).

bedrock, from the north-eastern parts towards the western-southwestern parts of the main chamber. Finally, small taluses are formed through the accumulation of *éboulis* at the junction of the steep cave walls and the floor.

The basal SU4 of the inner/rear parts of the cave is directly deposited on the limestone bedrock surface and its geometry reflects the inclined bedrock topography (Figs. 8 and 15). The SU4 and its sub-units (SU4.2 and SU4.1) contain moderate to low amount of angular and usually elongated limestone *éboulis*, floating within the matrix-supported, silt loam background. These strata contain **DFi-ii** microfacies, which exhibit micro-layering with rhythmic-like depositional patterns. The contacts and the coarse fraction follow conformably the gentle inclination of the slope, while rotational structures and circular arrangements around core mineral grains, as well as some turbate structures are occasionally reported. Such elements and features, along with the porphyric related distribution and the presence of air escape vesicles, commonly present within debris flows (Bertran and Texier, 1999; Menzies and Zaniewski, 2003; Philips, 2006), indicate similar deposition process for the SU4 sediments. The debris flows of SU4 are understood as relatively low-energy, viscous flows of fine-grained sediment with floating coarse components, assisted by the available water volume, driven by the precipitation (Bosch and White, 2004; Dasgupta, 2003). Occasional discontinuous thin laminae of moderately-to-well-sorted silts and silty clay, which follow the orientation of the slope, can be interpreted as episodes of overland flows or sheetwash (Fig. 8J; Karkanas and Goldberg, 2019; Mallol and Goldberg, 2017). Fragments of such shallow water-induced laminae are often found translocated, through the erosion and the incorporation within the debris flows. Sherriff et al. (2024) dated the basal SU4.2 to 52.40 ± 3.60 ka (OSL) and the overlying SU4.1 to 44.30 ± 2.90 ka (OSL) and 44,660–42,370 cal BP (charcoal--derived ^{14}C).

The cave entrance SU4 sediments are associated with the dynamics of the entrance cone topography and interpreted as a debris flow (Fig. 15). In particular, the matrix-supported SU4.3 and SU4.1 show the characteristic macroscopic features of the debris flow. On the contrary, the massive clast-supported SU4.2, dominated by angular limestone *éboulis* originating directly from the cliff freefall, represent one of the lower debris sheets building-up the entrance debris cone (rockfall facies). The contact between the SU4.3 and SU4.2 is partially erosive, but further investigation is required as the lateral and vertical extent of the former has not been exposed. The succession by the SU4.1 is conformable. Based on the new OSL ages, the SU4.1 was dated to 37.94 ± 1.67 ka, acting as a *terminus ante quem* for the onset of the inner cave entrance debris cone formation. The alteration between matrix- (SU4.1 and SU4.3) and clast-supported facies (SU4.2) suggests cyclical sedimentation pattern, with slower deposition of fine-grained sediments and more abrupt episodes of coarse material accumulation.

Six matrix-supported sub-units were recorded for the SU3 near the cave entrance, indicating series of grain and debris flow episodes. In contrast to the inner erosive SU4-SU3 contact, the deposition of the SU3.6 is conformable to the SU4. However, the subsequent SU3.5-SU3.4 contact is locally erosive, as the SU3.4 appears to split the SU3.5 in a channel-like manner. The SU3.5 was dated to 37.70 ± 1.51 ka as part of this study. The overlying SU3.3–3.1 are very thin sub-units without erosive features and represent a series of conformably overlying short depositional episodes of combined debris and/or grain flows. The **DFiii** microfacies typically show semi-horizontal orientation of the coarse component, parallel to the debris cone slope, while randomly oriented sediments also exist. The presence of weakly-developed rotational structures and arrangement of clastic material and aggregates around core grains can be associated with debris flow deposition. A distinctive element of the **DFiii** microfacies and the SU3.3–3.1 is the co-existence of clay-depleted and clay-rich matrices. The latter is introduced in the form of aggregates or peds and is often lumped with limestone granules.

The sediments of the SU3 are related to rockfall events and grain flow processes. The inner SU3.2 is a massive clast-supported unit, suggesting cave ceiling rockfall event(s) that have promoted the deformation and partial erosion of the SU4.1 sediments. The deposition of the SU3.2 follows a relatively steep slope with unconformable contact inclined towards the middle of the cave. The published and new OSL ages place the deposition of this unit between 45.10 ± 3.00 ka (Sherriff et al., 2024) and 37.77 ± 1.57 ka. The matrix-supported SU3.1 follows similar inclination and conformably overlies the SU3.2. The **DFiv** microfacies from the inner SU3.1 show random orientation of poorly sorted or unsorted matter and the relative absence of water-induced structures, therefore suggesting grain flow deposition (Mücher et al., 2018). The lateral contact between the inner SU3 and the SU3 of the entrance (central and southern part of the cave) remains unidentified due to the presence of severe bioturbation (section 4.2.3).

The SU2, consisting of the SU2.1 and SU2.2, is only found at the upper entrance strata and is interpreted as the outcome of rockfall and debris flows. The lower, matrix-supported and fine-grained SU2.1 is interpreted as a debris flow unit extending towards the external and internal parts of the debris cone. The slightly finer-grained character of the SU2.1, compared to the underlying units, suggests possible clay and silt sediment infiltration through the SU2.2 blocks. However, no micromorphological data are reported for this locality and further investigation is required. The SU2.2 consists almost exclusively of coarse limestone *éboulis*, mainly angular boulders and cobble-/pebble-sized limestone fragments with blocky and elongated forms, representing a massive rockfall event. The inner part of the SU2.2 is partially eroded by the overlying SU1.4. The SU2 is the uppermost unit within the area of the cave entrance, while no surface soil development is attested.

The SU1 deposits comprise a basal, erosive rockfall deposit, followed

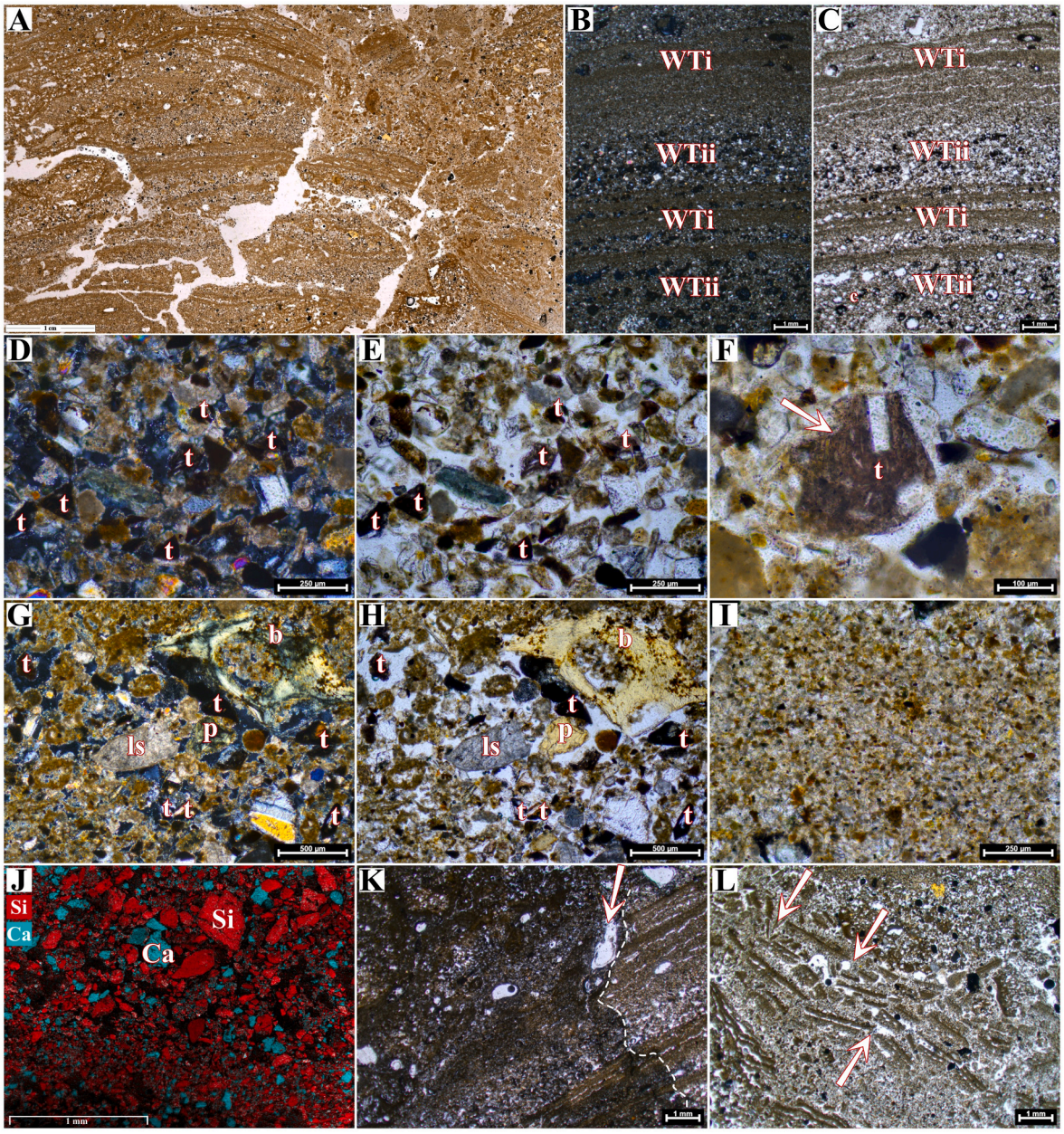

Fig. 11. Thin section scan and photomicrographs from **SU4** (**WTi-ii** microfacies). **A**) **ARAM6A** thin section scan, preserving water-induced laminated structures and large channel systems (PPL, scale = 1 cm). Similar laminated features are noted for **ARAM5C** too. **B**). Series of laminated structures, including fine-grained silty **WTi** and coarser-grained **WTii** microfacies, representing puddle formations with several episodes of coarse material inwash, from **ARAM5C** (XPL, scale = 1 mm). **C**). Same, in PPL. **D**) Angular, very finely-to-finely-sized sand particles of pyroclastic material and volcanic tephra/tephra shards with feldspar micro-phenocrysts (**t**), within **WTii**, from **ARAM6A**. Note the very dark reddish brown, nearly black colours, the angularity and the smoothness of their surface (XPL, scale = 250 μm). **E**). Same, in PPL. **F**) Zoomed-in view of an example of finely-sand-sized, dark reddish brown pyroclastic shard with high density of feldspar micro-phenocrysts (**t**), from **ARAM6A** (PPL, scale = 100 μm). **G**) Poorly-sorted **WTii** locality with highly heterogenous composition, including significant contribution by medium-/finely-sand-sized tephra and pyroclastic grains (**t**), coarse-sand-sized limestone *éboulis* (**ls**), quartz and feldspar grains, bone fragments (**t**) and coprolitic matter (**p**), from **ARAM6A**. Surficial inwash patterns, from the exterior to the rear parts of the cave would explain the heterogenous character of some localities within **WTii** (XPL, scale = 500 μm). **H**) Same, in PPL. **I**). Zoomed-in view of finely-grained, silt-dominated **WTi** microfacies, from **ARAM5C** (PPL, scale = 250 μm). **J**) SEM-EDS elemental mapping of **ARAM6A** locality with graded fabric, denoting the dominance of allochthonous Si-rich (**Si**) minerals that include significant pyroclastic material contribution. $CaCO_3$-rich (**Ca**) grains are present, but in lower percentages (scale = 1 mm; see also SI.A5). **K**) Dripping water-induced deformation of the laminated features and replacement with silty, $CaCO_3$-enriched sediments, from **ARAM5C**. Note the presence of intact laminar relicts, due to the impermeability of the silty clay composition (PPL, scale = 1 mm). **L**) Mechanical deformations of the laminated structures, due to sedimentary load impact/*éboulis* collapse from the overlying **SU3** and/or bioturbation (note the presence of small channels), observed in **ARAM6A** (PPL, scale = 1 mm).

by episodes of grain flows. The massive, clast-supported SU1.4 at the southern and northern parts of the cave were likely deposited by collapse from the cliff and the cave ceiling. These events led to partial erosion of the upper parts of the SU3 and the SU2. The overlying matrix-supported SU1.3–1.1 represent conformably overlying grain flows induced by the slopes of the cave entrance and the inner parts, through minor rockfall deposition and aeolian sedimentation. The published OSL dates for the SU1.3 and SU1.2 place the deposition between age of 35.10 ± 2.50 ka and 33.40 ± 2.50 ka (Section 4.1.4.1). The micromorphological results of the SU1 deposits are similar to those noted for the SU3,

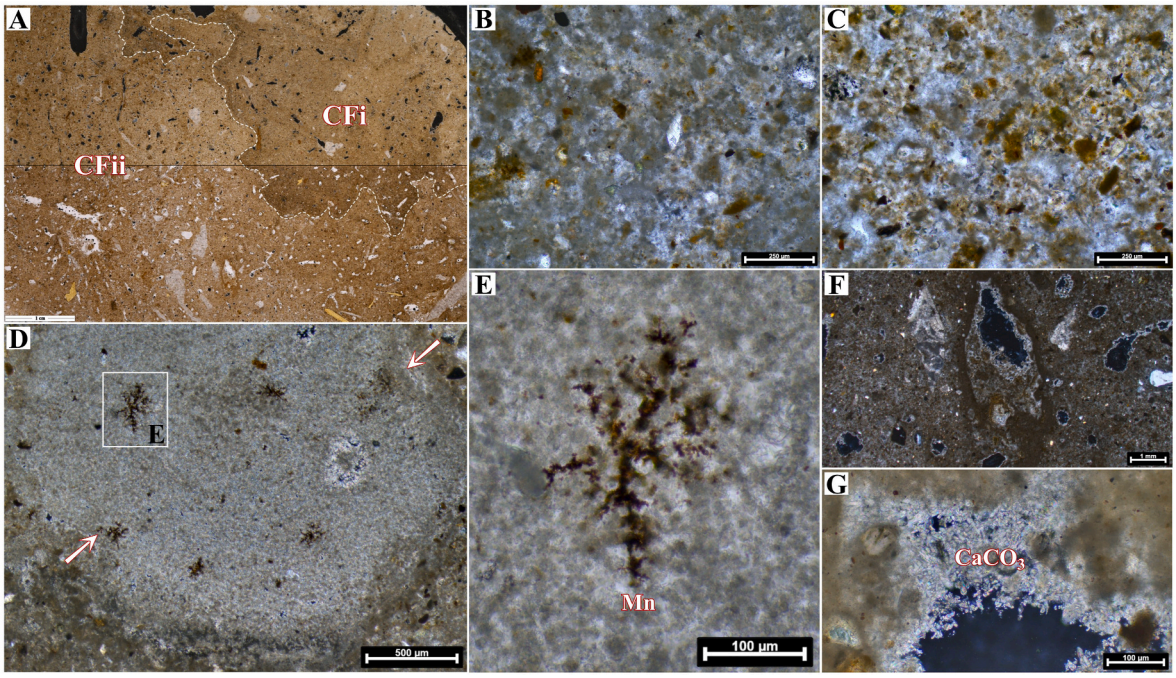

Fig. 12. Thin section scan and photomicrographs from areas **near the cave bedrock/SU4** (**Cfi-ii** microfacies). **A**) **ARAM2** thin section scan of sediments near the bedrock, at the inner/rear part of the cave, in XPL (upper) and PPL (lower). The dotted line demarcates the lateral contact separating the **Cfi** and **CFii** microfacies (scale = 1 cm). **B-G**) All photo-micrographs are from **ARAM2**. **B**) Well-cemented **CFi** fabric dominated by fine-grained, silt-sized matter, mainly micritic $CaCO_3$ (PPL, scale = 250 μm). **C**) Moderately-cemented **CFii** fabric with high micritic $CaCO_3$ matrix impregnation and significant contribution of loessic, silty micro-aggregates (PPL, scale = 250 μm). **D**) Large (max. diameter c. 2.2 mm) nodule of micritic and micro-sparitic $CaCO_3$ (XPL, scale = 500 μm). Note the presence of impregnative dendritic Mn-oxide nodules. **E**). Detail of dendritic Mn-oxide (**Mn**) nodule from micrograph **D** (scale = 100 μm). **F**) Calcified root remains, infilled with micritic $CaCO_3$, from **CFii** (XPL, scale = 1 mm). **G**). Micro-sparitic to micritic $CaCO_3$ hypo-coating from **CFii** (XPL, scale = 100 μm).

as they share the same **DFiv** microfacies with unsorted or poorly-sorted and randomly oriented sediments, lacking the water-induced character, indicative of grain flows. As in the SU3, the sediments of the SU1 show extensive bioturbation. The SU1 is overlain by the weakly developed cave topsoil, the SU0, within which (especially the rearmost, unexcavated parts of the cave) Holocene-dated archaeological remains (ceramic sherds and a large grinding slab) were found.

The external profile documents three distinct sedimentological units, SU3, SU2 and SU1. The lowermost SU3 consists of the matrix-supported, $CaCO_3$-rich and well-indurated SU3.2 and the clast-supported, moderately-indurated SU3.1. However, as most of the SU3 remains unexcavated, further investigation is required. The overlying SU2 consists of a series of matrix-supported (SU2.D, SU2.B) and clast-supported sub-units (SU2.E, SU2.C, SU2.A) indicative of rockfall and debris flow depositional patterns. These strata are external manifestation of the debris cone sequence. The new OSL ages indicate that the SU2.E (42.90 ± 1.79 ka) and SU2.D (37.77 ± 1.57 ka) were deposited in relatively close succession. This indicated that the matrix-supported SU2.D was developed around the same time as the internal part of the entrance debris cone (SU3.5 at 37.70 ± 1.51 ka and SU4.1 at 37.94 ± 1.67 ka), suggesting synchronous depositional episodes blanketing both sides of the cone. Therefore, the deposition of the SU3.E and the SU4.2 postdated 42.90 ± 1.79 ka, as both strata represent massive rockfall debris sheets, which possibly form the basal topography for the deposition of the SU2. E and SU3.5/4.1 event.

Large proportion of the fine-grained matrix of the debris and dry grain flows, represented by subrounded, micro-aggregated silty-clay/silt particles, feldspars, micritic and micro-aggregated $CaCO_3$, subangular quartz and rare volcanic tephra shards, can be associated with aeolian sediment sources (Crouvi et al., 2010; Pye and Tsoar, 2009). The predominance of the silt fraction (10–70 μm) at ≥50 % correlates with the micromorphological observations and is consistent with the loessic nature of the matrices. The presence of a minor mode at the ≤10 μm range and the clay within very fine silty-clay micro-aggregates could be attributed to longer-distance travelling aeolian dust (Pye, 1995; Tsoar and Pye, 1987), rather than post-depositional aggregation. The subangular/subrounded shape is evidence of the textural maturity of these particles, supporting their allochthonous loessic sources (Karkanas and Goldberg, 2019). These sediments are deposited through wind suspension and are re-deposited via the debris/grain flow dynamics. Subrounded shapes of sand-sized, silty-clay-coated aggregates, commonly present at the upper parts of the entrance SU3 deposits (**DFiii**), could be associated to aeolian saltation and/or rolling (Boschian, 1997). Such materials are deposited at the entrance possibly through colluvial processes, via the erosion of sediment pockets proximal to the cave, which would be rich in such particles and clay-rich matrices. Although colluvial sedimentation is not pronounced in (semi-) arid landscapes (Frumkin et al., 2016), possible minor colluvial contribution of clay-rich sediments admixed with saltation-impacted particles, could explain their presence at the entrance (Krajcarz et al., 2016). Opposed to the allochthonous finer fractions, the sand-sized and coarser geogenic components (granule-to-boulder-sized clasts) are autochthonous, almost exclusively related to the degradation of the cave limestone bedrock (*éboulis*). These materials have angular shapes and often elongated forms, indicative of short-distance movement and very low textural maturity (*sensu* Folk, 1951; Campaña et al., 2016).

The progressive upwards coarsening of the matrices from silt loamy (SU4-3) to loamy sediments (SU1-0) with higher sand component coincides with a decrease in Al-rich minerals and an increase in Ca-related material (Figs. 3 and 5B). This upwards increase of $CaCO_3$/calcite is further supported by Loss-On-Ignition and FTIR (Fig. 5A and Fig. 6). Grain shape results are also consistent with this pattern, as the lower SU4 sediments show higher homogeneity for all morphological parameters and, therefore, higher textural maturity. Conversely, sediments from the overlying SU3 and, especially, SU1 exhibit lower textural maturity, associated with autochthonous mineralogy (sand-sized

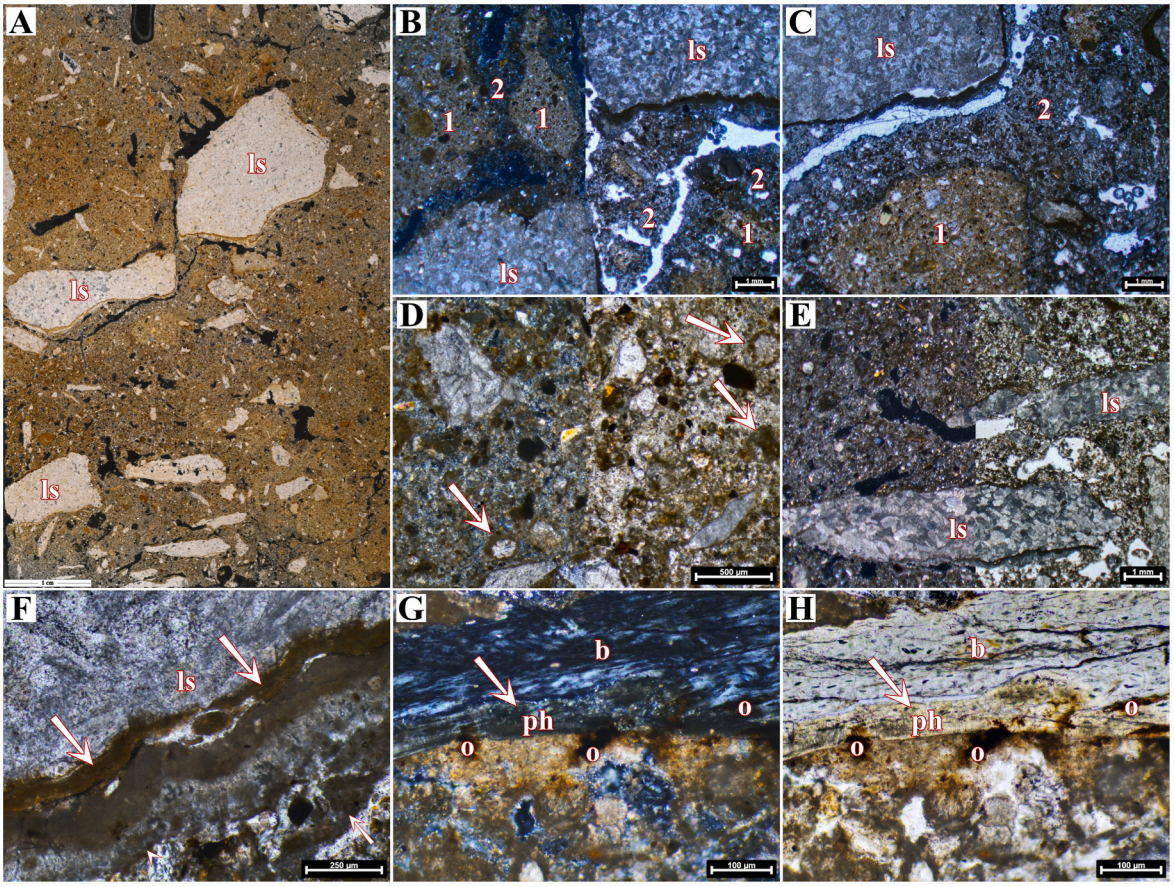

Fig. 13. Thin section scan and photomicrographs from the **Cave Entrance SU3En** (**DFiii** microfacies). **A**) **ARAM1** thin section scan with **DFiii** microfacies, consisting of granule- and gravel-sized limestone *éboulis* and two fine-grained matrices/fabrics (**13.B-C**; PPL, scale = 1 cm). **B**) **DFiii** deposits with clay-rich **Fabric 1** (**1**) and clay-poor **Fabric 2** (**2**), from **ARAM1** (XPL – left and PPL – right; scale = 1 mm). The presence of pendant-covered limestone granules/gravels (**ls**) is common. Note the long channels passing through **Fabric 2**. **C**) Large subrounded aggregate of **Fabric 1** embedded within **Fabric 2**, from **ARAM1** (PPL, scale = 1 mm). **D**) Fine silty clay micro-aggregates and subrounded, aggregated mineral grains (or pedorelicts; see arrows), possibly related to aeolian rolling and/or saltation (*sensu* Boschian, 1997), observed in **ARAM1**. These grains likely originated from earlier deposits outside the cave and were incorporated into entrance sediments via debris flows. Angular, coarse sand-sized limestone fragments are also reported (XPL – left and PPL – right; scale = 500 µm). **E**) Angular, elongated, (semi-) horizontally oriented limestone gravels (**ls**) are very common in **ARAM1** (XPL – left and PPL – right; scale = 1 mm). **F**) Micro-laminated dirty, silty/silty clay capping (c. 500 µm thickness) on limestone gravel, from **ARAM1** (PPL, scale = 250 µm). At least 4 laminae are reported (from **ls** to the matrix): i) silty clay, Fe-rich lamina (Fe possibly due to exposure/reaction rim), ii) dirty/dusty silty/silty lamina, iii) recrystallized lamina with local dirty silty 'clouds', iv) silt-rich laminae with allochthonous mineral inclusions. **G**) Bone fragment (**b**) with internal mechanical fractures, Fe-oxide staining (**o**) and weak phosphatisation of the lower part (**ph**), from **ARAM1** (PPL, scale = 100 µm). **H**) Same, in XPL.

limestone *éboulis*). Thus, these observations suggest a shift in the matrix sediment sources, expressed by the gradual decrease in the allochthonous aeolian input and the increase in the autochthonous calcareous-limestone contribution. Possibly, this change in the sedimentation of the upper strata is due to a more pronounced syn-depositional reworking and deflation (Mallol and Goldberg, 2017), stripping away portion of the fine-grained aeolian matrices. The complete infilling of the cave's accommodation space may have triggered the onset of such erosive processes. The decrease in fine-grained sediments might also be linked to broader palaeoclimatic phenomena, particularly a reduction in aeolian sediment circulation. Such patterns are observed in the loess-palaeosol sequences of northeastern Armenia, which show evidence of drastic decline in loess deposition at the onset of MIS2 (Wolf et al., 2022). Nevertheless, this hypothesis cannot be fully assessed, due to the limited availability of relevant data from the cave surroundings and Ararat Depression. The lower percentages of $CaCO_3$ and Ca in SU4 may also reflect dissolution processes impacted from the phosphate diagenesis (Section 4.1.4.3). However, the latter is only weakly developed and with limited effect on the sediment matrix, and therefore its influence should be considered rather meager.

The magnetic susceptibility values of the bulk sediments indicate the presence of magnetic minerals and volcanic tephra in low proportions throughout the entire Ararat-1 sequence. Significantly enhanced magnetic susceptibility values attributed to strong admixture of volcanic minerals, is known for open-air loess pedocomplexes in the northeastern parts of the Armenian Highlands (Achajur/Sevkar: Wolf et al., 2022; Lomax et al., 2021). Although no direct comparison is possible, due to the differential standardization of the susceptibility measurements (Lomax et al., 2021), the relatively lower values detected within the southeastern parts of the Ararat Depression and Ararat-1 Cave could be explained by the increased contribution of calcareous sediments eroded from the carbonate lithologies into the loess (Wolf et al., 2022; also: Sherriff et al., 2024).

4.1.1.2. Water-induced processes and material origin. The presence of well-defined water-induced sedimentary structures is only noted at the inner rear parts of the cave (SU4.2 and SU4.1; LFa-b; Table 1). These structures (Fig. 11A-C) are characterised by the presence of curved, parallel, occasionally planar and often interbedded laminae of moderately-to-well-sorted silts and silty clays (**WTi**) and poorly-sorted, heterogeneous, sand-rich loams (**WTii**). The latter represents series of deposition of in-washed, mixed sediments through sheetwash processes,

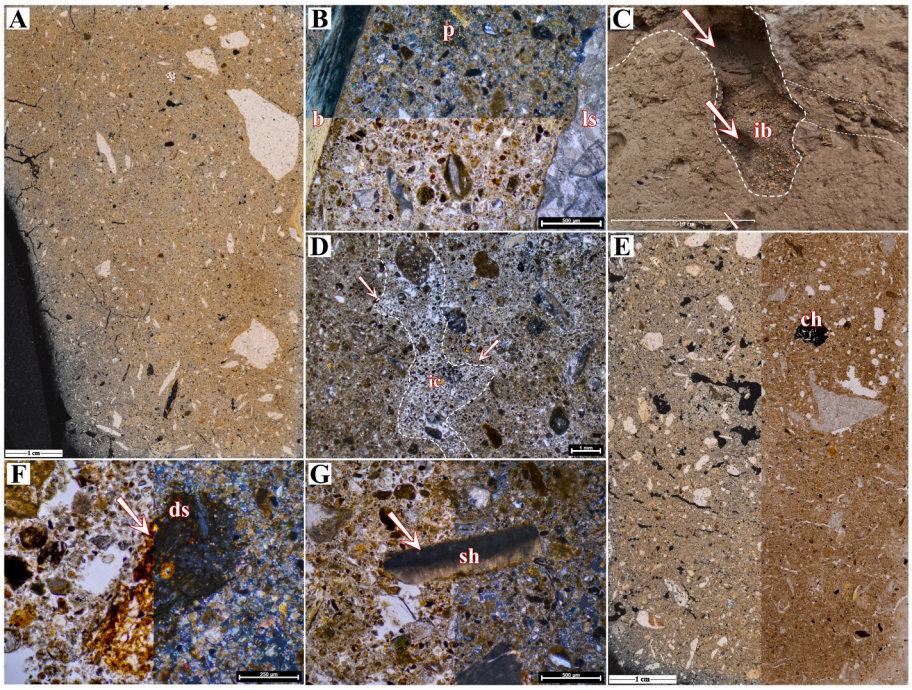

Fig. 14. Thin section scan and photomicrographs from **SU3** and **SU1** (**DFiv** microfacies; **Cave Interior**). **A**) **MM3** thin section scan, containing grain flow deposits (**DFiv**; **SU3**). The coarse component follows random distribution patterns (XPL, scale = 1 cm. **B**) Typical aeolian fabric of the **DFiv** (**MM3**), including micro-aggregated silts/clayey silts and subrounded, micro-aggregated sand grains with silty clay, possibly attributed to aeolian saltation and/or rolling (*sensu* Boschian, 1997). Limestone granules/gravels (**ls**) are common, while bone pieces (**b**) and coprolitic matter (**p**) are occasionally present (upper in XPL and lower in PPL; scale = 500 μm). **C**) Macroscopic view of burrow (**ib**) infilled with reworked matrices from the **SU3** (northern profile; scale = 10 cm). **D**) Infilled micro-burrow (**ib**), from **MM2** (PPL, scale = 1 mm). Such features are common within the **SU1**. **E**) **MM1** thin section scan, containing **DFiv** grain flows and rare, Holocene-dated possible anthropogenic material (a large piece of charcoal – **ch** – see also: Sherriff et al., 2024; left – XPL and right - PPL). **F**) Near-fresh excretory remains with occasional dung spherulites (**ds**) and silica/plant remains, from **MM2** (PPL – left and XPL – right). Partially decayed and near-fresh excrements and other organic matter are very common within the **SU1**. **G**) Shell fragment, from **MM1** (PPL – left and XPL - right).

triggered by rainfall events. These translate into unidirectional flow of allochthonous material and surficial sediments derived from the cave exterior by traction and, to a lesser extent, suspension. Such deposition might be attributed to extensive water flows from the cave's cliff during torrential events. These were deposited within puddles which formed in small depressions at the rear parts of the cave. Two alternated phases of deposition are recognized, (1) sheetwash of coarse material during relatively higher energy events (**WTii**) within the puddles; and (2) low-energy quiescent settling of moderately-to-well-sorted silts/silty clays (**WTi**; Karkanas and Goldberg, 2019; Mallol and Goldberg, 2017; Bull, 1981). Micromorphologically observed deformation features show the syn- and post-depositional degradation of these structures. The presence of compression features and the air-escape porosity suggest a plastic character of the deposits under water-saturated conditions, while deformation features through water dripping are also noted. Post-depositional alterations occur mainly through bioturbation, as well as gravitational impact from the overlying, erosive SU3.2 rockfall episode (Fig. 15).

Mineralogically and sedimentologically **WTi** and **WTii** are different. **WTi** is relatively homogeneous, consisting of subrounded silty clay micro-aggregates of allochthonous windblown origin and silty clays through settling. **WTii** microfacies are heterogenous, comprising of rip-up fragments and rounded silty clay micro-aggregates (originally of aeolian sources), sand-sized limestone clasts, feldspars and quartz grains, and non-mineral materials (bone fragments, coprolitic nodules), eroded from the exterior and the cave surface, and re-deposited via sheetwash. Moreover, a significant percentage of the mineral component is related to angular volcanic tephra shards and other volcanoclastic fragments (fine/very fine sand), with high density of feldspar micro-phenocryst (morphotype: McLean et al., 2018). The presence of volcanic-derived component is also supported by the higher magnetic susceptibility values noted for these laminae. The relative abundance, the angularity and the lack of pronounced weathering of the shards might indicate relatively recent primary tephra deposition within the immediate cave surroundings. The tephra would then likely be in-washed into the cave following rainfall. Further chemical and tephrochronological analyses might provide a chronological anchor for the eruption episodes (Blockley et al., 2025), reducing temporal uncertainties and highlighting the relationship between human visits and such impactful events (Karkanas et al., 2015b; Lane et al., 2014).

4.1.2. Biogenic contribution

Bone fragments and coprolitic matter are some of the most dominant materials of biogenic origin in Ararat-1 Cave (Fig. 10). Except for a few heated bone examples, most of the faunal bone micro-assemblages are associated with meso- and micro-fauna denning. The habitation of both herbivorous and carnivorous animals is supported by the micromorphological results, as both spherulite-rich and bone-containing coprolites and coprolitic matter are identified respectively. Both bones and excretory products are found throughout the entire sequence, while they appear more prominent within the inner-rear parts of cave, where denning activities are suggested to occur (Mallol and Goldberg, 2017; Sanz et al., 2016). Animal or bird presence can be detected within the cave entrance too, lacking, however, the predominant character of the rear part of the cave (Canti and Brochier, 2017). Furthermore, the existence of herbivorous animal excretions is attested through the quantification of dung spherulites, which shows high contribution throughout all the sedimentological units. The highest representation is marked for the SU0, where macroscopically identifiable dung remains and the highest phosphorus peaks are also reported.

Other types of herbivore excretions, such as fibrous pellety masses (e.g., Karkanas and Kyparissi-Apostolika, 2024; Leierer et al., 2019),

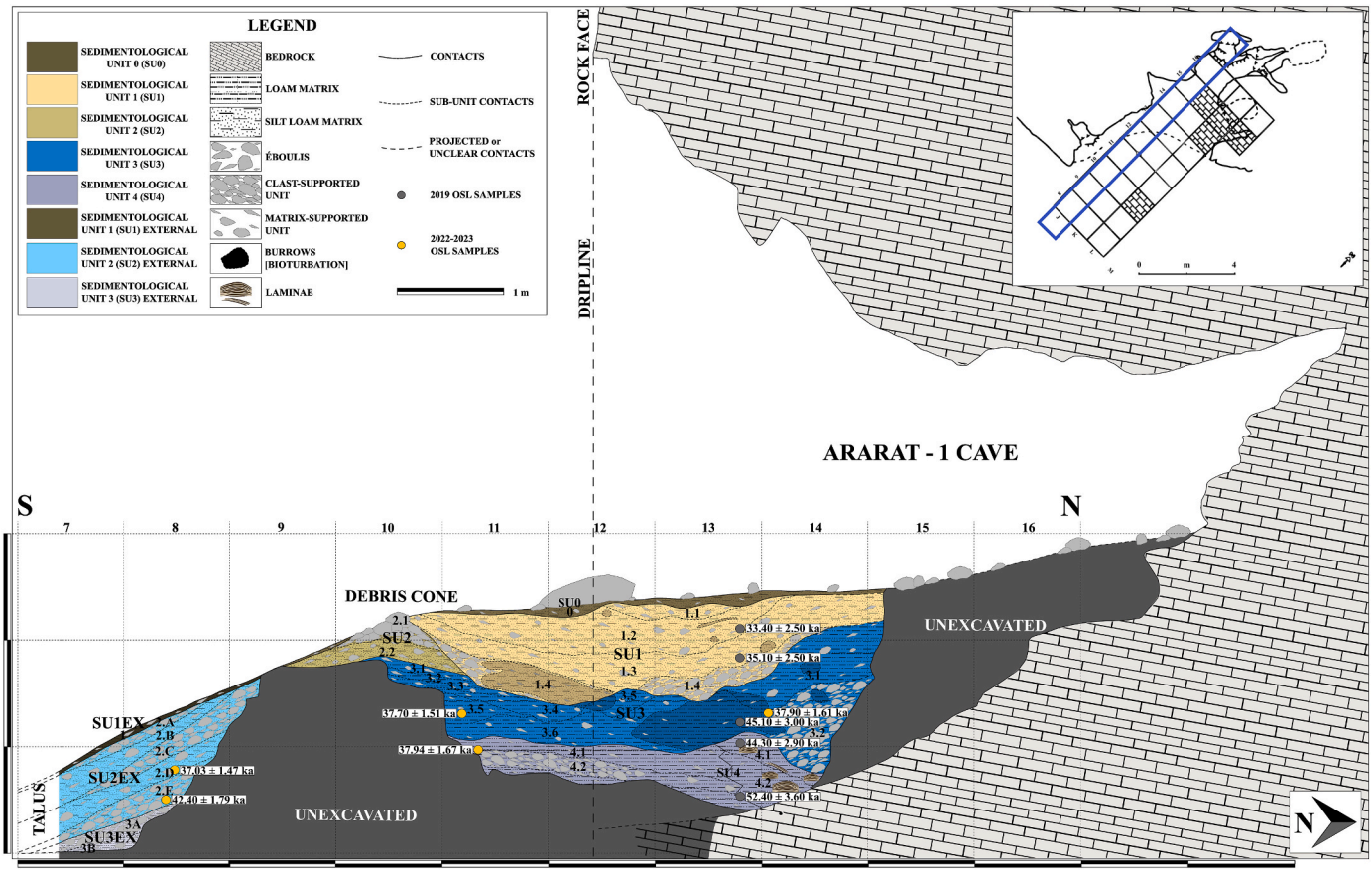

Fig. 15. Longitudinal section of Ararat-1 Cave, showing the known stratigraphic sequence throughout the S-N axis. The position of the longitudinal section is shown on the floorplan of the excavation (for the explanation of the various features, see 'LEGEND'). Note the stratification in relationship to the cave bedrock inclination, the cliff and the formation of the debris cone near the cave entrance.

spherulite-containing coprolitic matter is rarely reported for Palaeolithic sites. Lusakert-1 (cave-site within the Armenian Highlands) is one of such rare Middle Palaeolithic examples (Williams, 2004; Brittingham et al., 2019 Supplement; Mallol and Goldberg, 2017), possibly suggesting the presence of a common herbivorous animal responsible for the production of such subrounded spherulite-rich nodules during the Pleistocene (Fig. 10O). As thin section microscopy usually cannot provide identification at a species-specific level (Canti, 1997), further (micro-) faunal and biomolecular analyses could elucidate this issue (Shillito et al., 2020; Brönnimann et al., 2017a). Fresh-looking dung and dung spherulites from upper strata (mainly SU1 and SU0) should be attributed to Holocene-dated and recent animal activities. The identification of coprolites and coprolitic fragments attributed to carnivorous agents, where possible, can be primarily associated with small non-hyenid carnivores. Examples of large, tubular coprolite fragments of massive pale yellow, finely dotted, autofluorescent phosphatic groundmass with thin cortex and partially digested by gastric acid angular bone fragments (Fig. 10A, J-L), are usually attributed to such small carnivores, possibly fox, lynx, or badger (Brönnimann et al., 2017b; Sanz et al., 2016; Carrión et al., 2005). Such attribution can be supported by the preliminary zooarchaeological analyses, which highlight the presence of badgers, small felids and foxes (Vettese et al., in prep.). Smaller coprolitic pieces and nodules, occasionally preserving thicker cortex and well-digested bone fragments, could be attributed to hyena (Brönnimann et al., 2017b; Horwitz and Goldberg, 1989). However, the small size and the fragmentary character of the latter does not permit a definite identification. The contribution of other small herbivorous or omnivorous/carnivorous mammals, rodents, herpetofauna and birds, identified through the micro-zooarchaeological studies (Rogall et al., 2025), cannot be excluded (Brönnimann et al., 2017a; Mallol and Goldberg, 2017).

In most cases, the coprolite and bone micro-remains are partially translocated through the effect of the debris-grain flow deposition, as well as through syn- and post-depositional bioturbation (see Section 4.1.4.1.; Mentzer, 2017). The high degree of bone fragmentation should be attributed to similar agents as well (Rogall et al., 2025). *Quasi in situ* deposition of large carnivore coprolites and coprolitic fragments is suggested for localities only within the lower SU4.2 and SU4.1 (**DFab**; **ARAM3**). The co-representation of both fauna-related and anthropogenic residues, is observed within these localities. In other sedimentological units, such as the SU3 and SU1, the co-existence is reflected by the detection of both dung spherulites and ash pseudomorphs in the same bulk samples. The absence of burned spherulites indicates that ash pseudomorphs are not brought into the site through biogenic agents and should reflect anthropogenic activities.

The relative scarcity and mis-representation of plant-related biogenic materials could be partially related to the dry character of most of the strata, as well as the aridity of the broader region. Fresh-looking and partially humified plant matter, identified by the fibrous structures (Ismail-Meyer, 2017), the presence of fresh calcium oxalates and rare silica skeletons is occasionally reported for the upper strata (SU1-0), where it usually represents component of faecal matter. The presence of bio-silicate remains, especially opaline phytoliths, is very low, yet reported. The general scarcity of the phytoliths and the limitations imposed by thin section micromorphology do not permit a comprehensive understanding of its origins and any possible association to anthropogenic activities, except for cases where it can be directly linked to animal excrements, without the incorporation of

phytolith-specific analyses.

4.1.3. Anthropogenic contribution

The micro-geoarchaeologically detected anthropogenic component is very scarce, yet present within the inner-rear parts of the cave (**DFab** and SU4). These microfacies contain fire-induced remains, such as charcoal fragments and micro-comminuted charred plant matter (Mallol et al., 2017), aggregates of ash pseudomorphs and $CaCO_3$-enriched ashy matrices (Canti, 2003), as well as few heated bone fragments (possibly c. 400 °C; Villagran et al., 2017). Reddish silty clay aggregates, often associated with burning (Röpke and Dietl, 2017), are very rare in Ararat-1. Such pyrogenic components and features are found slightly translocated, as part of the debris flows and are only preserved in a few, partially indurated micro-layers. The partial translocation and reworking should be attributed to surficial gravity-related processes, as well as animal denning and nesting (Mentzer, 2017). No evidence of trampling is observed (Rentzel et al., 2017), as the fire residues are not in *in situ* deposition. The localised induration, eventually functioning as preservation mechanism, should be primarily attributed to calcite precipitation, while ash recrystallisation, often observed in karstic caves (e.g., Karkanas et al., 2007), appears insignificant. The clustering of the anthropogenic products, along with the presence of large aggregates of intact ash pseudomorphs, is consistent with fire-producing activities conducted by human agents within the limits of the cave. The presence of ashes and ash pseudomorph concentrations, along with the absence of burned dung spherulites, or any other evidence of coprolite burning, further supports the anthropogenic character of the combustion activities, where no animal faeces had been utilised as fuel. Such low residuality features should be attributed to few episodes of ephemeral combustions and use of hearths, during short-lived human visits. The presence of heated bone fragments might have implications for the character of such fires, as related to subsistence practices. This can be corroborated with the preliminary zooarchaeological analyses, showing that more than 7 % of the faunal assemblages document pyrogenic modifications (Vetesse et al., in prep.). Heated microfauna and/or herpetofauna remains are nearly absent, as only c. 0.05 % of the assemblage exhibits traces of burning (colouration), indicating a rather accidental character (Rogall et al., 2025).

Magnetic susceptibility values are low within all units and therefore do not suggest burning and fire-induced transformations of magnetic minerals (e.g., Schiegl et al., 1996). However, the undifferentiated susceptibility results from the areas preserving pyrogenic products should not be attributed to the absence of fire. Instead, they reflect the scarce nature of the low-density record, as admixed with the general matrix and buffered with karstic-induced calcite precipitates, as well as sampling biases, due to the over-localised character of the fire remains. Similarly, the absence of clay alteration peaks in the infrared spectra could be explained by such sediment mixing (Oikonomou, 2023; Oglobin Ramirez et al., 2023).

The contribution of other, non-pyrogenic anthropogenic materials appears less prominent. Although no micromorphological identification is possible due to the fragmentary nature of most of the faecal matter (Section 4.1.2.), the presence human-produced coprolites cannot be totally excluded for the areas that document human-related residues (**DFab**; Brönnimann et al., 2017b). Except for a single detected microflake, knapped lithic artefacts and fragments, commonly reported in Palaeolithic sites (Angelucci, 2017; Angelucci and Zilhão, 2009; Courty, 2001), remain largely undetected in Ararat-1 thin sections. Disregarding the inherent limitations imposed by the localised micromorphological sampling procedures, the lack of artefacts could be primarily attributed to the low-density character of the site. The high completeness rate of the lithic record shown by Nora et al. (2025), could explain the absence of artefact fragments, as the numbers of the latter appear in general relatively low throughout the entire sequence. Interestingly, the percentages of complete lithic artefacts show an upward decreasing trend, from c. 64 % in the SU4 to c. 57 % in the SU0, suggesting increased upward fragmentation due to post-depositional modifications, through the mass movement processes and the intensification of bioturbation.

4.1.4. Micro-environments and post-depositional/diagenetic changes

4.1.4.1. Bioturbation. Ararat-1 Cave preserves evidence of bioturbation throughout the entire sequence, with the SU3 and SU1 showing the highest rates of disturbance. Since denning and habitation of the cave by faunal populations appear as recurring activities, the redistribution of anthropogenic matter can occur very shortly after a human visit (Mallol et al., 2017; Mentzer, 2017). Such penecontemporaneous character of the human and animal deposition is evident in **DFab** and SU4, where, nevertheless, other post-depositional bioturbation features are only weakly developed, thereby retaining the sedimentary integrity. The latter can be explained by the finer-grained, clay-inclusive textures that promote stability (French, 2017), the presence of locally cemented areas, and the sealing of most of the SU4 by the overlying SU3.2 rockfall. However, the presence of post-depositional fauna-induced burrows and infilled channels curved into the loose loessic sediments, especially within the main and rear parts of the cave, has a far greater impact on the preservation of sedimentary and anthropogenic features. Deeply penetrating passages, especially in the rear parts of the cave, cause strong sediment reworking and remobilisation through different strata with possible effect on the chronometric estimations (see **4.2.2**). This is further supported by the inversion in the OSL ages (45.10 ± 3.00 and 37.77 ± 1.57 ka) in the inner parts of the SU3, where larger burrows are present.

The redistribution of sediment from the lower to the upper strata through burrowing and the intense mixing is also seen in the SU1, where the ^{14}C results of charcoal and bone show Holocene ages (cal. AD 607–675, 1460–1634, 1523–1662, 1680–1940, 1462–1634; Sherriff et al., 2024), while the OSL results provide two consistent Pleistocene ages (35.10 ± 2.50 ka and 33.40 ± 2.50 ka). It is noteworthy that the very high fragmentation rates of the microfauna assemblages, as reported by the relevant analyses (Rogall et al., 2025), are consistent with the intensive bioturbation. In contrast to faunal reworking, plant bioturbation appears very weak (Sherwood and Goldberg, 2001). It is expressed by the occasional or rare occurrence of plant roots, usually in calcified forms, and pore space indicative of root passaging, showing only minor impact on the integrity of the record.

4.1.4.2. Micro-environments and calcite cementation. Calcite indurated sediments are observed for areas near the bedrock and the cave walls, and parts of the SU4. The presence of micritic $CaCO_3$ impregnation through water percolation, micro-laminated calcareous crusts, nodules and hypo-coatings are evidence of secondary cementation through karst-induced dripping (Durand et al., 2018; Mallol and Goldberg, 2017). The degree of cementation is usually determined by the degree of $CaCO_3$ impregnation (**CFa-b** microfacies), with highly cemented areas showing high percentages of micritic $CaCO_3$ and moderately cemented areas with lower respective percentages and more heterogeneous, admixed character. Occasional recrystallisation to mirosparitic and, more rarely, sparitic $CaCO_3$ is also reported. The infilling of bone fractures, haversian canals and pores by calcite constitutes further evidence of the induration processes.

While Ararat-1 represents an example of hydrologically inactive cave, fluctuating hydrological regime (including phases of wetting and drying) in the SU4 is indicated by increased Fe/Mn ratio, the presence of sheetwash and puddle formation, karstic water dripping, the appearance of sesquioxide matrix features, the extensive oxide staining related to coprolite, bone or other biogenic matter degradation (Vepraskas et al., 2018; Villagran et al., 2017). The upward diminishing Fe/Mn ratio from the SU3 to the surface, suggests a shift from a less stable water-influenced hydrological environment to a consistently dry and oxic environment. Although changes in cave environments are often

interpreted in conjunction to large-scale, often global, shifts, it is more appropriate to attribute them primarily to local and micro-environmental changes (Sherwood and Goldberg, 2001). Warming and cooling could have a progressive weathering effect, resulting into the accretion of limestone *éboulis*. However, the impact of cryoturbation and freeze-thawing processes, often reported for other cave sites in the broader regions (e.g., Ortvale Klde: Cullen et al., 2021), are not observed in Ararat-1 sediments.

4.1.4.3. Phosphate diagenesis. Chemical alterations related to the circulation of phosphorus are relatively limited but nonetheless present in the lower unit of the cave (SU4). The main source of phosphorus in the SU4 is likely related to considerable amount of carnivorous and herbivorous animal excretions, as well as bone fragment contribution. The decomposition of the coprolites and other organic matter (Horwitz and Goldberg, 1989), along with the water infiltration, initiates the diagenetic pathways, enriching the matrix with phosphorous and forming acidic P-rich solutions. The pale greyish white and yellowish nodules and granules of hydroxylapatite ($Ca_5(PO_4)_3(OH)$) can be attributed to an initial stage of calcite reaction with the phosphatic solution (Karkanas and Goldberg, 2018; Schiegl et al., 1996). The reaction of the P-solution with the limestone clasts is demonstrated by the presence of yellowish illuvial phosphates as internal crack infillings, reaction rims, as well as by the formation of amorphous calcium phosphate granules/nodules (Karkanas and Goldberg, 2018; Karkanas et al., 2000). Such non-stoichiometric calcium phosphates retain the yellowish colour in XPL, while exhibiting a peculiar birefringence, possibly retaining portion of the characteristics of the calcite refractive index (Fig. 9H-J). The presence of bone alterations with 'ropy' patterns and unusual interference colours should be related to these processes.

Severe diagenetic alterations, usually associated to very high amounts of animal faeces and, especially, bat guano (Karkanas, 2017; Karkanas et al., 2000, 1999; Weiner, 2010; Weiner et al., 2002), are not observed in the site. The relatively limited inflow of phosphatic solutions and the confined water throughflow in Ararat-1 Cave could not promote extensive acidification. The latter is clearly illustrated by the preservation of intact dung spherulites, ashy sediments and ash pseudomorphs, highlighting the localised and restricted phosphate diagenetic effect (Gur-Arieh and Shahack-Gross, 2020; Brönnimann et al., 2017a; Canti and Brochier, 2017; Canti, 1997, 1999, 2003). Underestimations in luminescence-derived ages attributed to P circulation, occasionally suggested for cave deposits (Campaña et al., 2023), cannot be totally excluded for the SU4 ages where minor phosphatic neoformations exist. However, the merely weakly developed diagenetic alterations might imply that such underestimation is only of minor impact.

4.2. Ararat-1 depositional histories and beyond

4.2.1. Depositional histories (Fig. 16)

The inner SU4 unit exhibits bracketing ages of 52.40 ± 3.60 ka to 44.30 ± 2.90 ka showing that sediments were deposited over a period between 15.5 and 1.5 ka. Nearer to the cave entrance, SU4 sediments continued to be deposited forming parts of a debris cone until 37.94 ± 1.67 ka. The debris flow deposits in the basal part of the SU4 were infilled by tephra-rich sheetwash material. These were laid within puddles that correspond to spatially variable topographical changes within the cave, and indicate a hydrological milieu with higher water content. The debris flows of these lower units are composed of fine-grained windblown matrices and limestone *éboulis*. Within this period, low-intensity, ephemeral human visits occur in the cave, resulting in the deposition of scarce pyrogenic residues. Moreover, the presence of biogenic products throughout most of the stratigraphic sequence, especially within the inner/rear parts of the cave, suggests a frequent mode of animal habitation related to denning activities. The close depositional association of such anthropogenic remains with biogenic, excretory products of small carnivores and herbivores, indicates a temporally proximal re-occupation of the site by animal agents (Horwitz and Goldberg, 1989).

The SU3 sediments were deposited over similar timescales to SU4, though it is not possible to establish more precise timeframe as no sample was collected from the top of SU3. The approximate depositional period extends over 2–11 ka, calculated between 44.30 ± 2.90 ka (SU4) to 37.90 ± 1.61 ka years (inner parts) and 37.70 ± 1.51 ka years (cave entrance). The unit is primarily associated with dry grain flows, and with a massive rockfall event, eroding portion of the SU4 deposits of the inner cave. The origin of the sediments is similar to that of the SU4, while a subtle coarsening of the matrix is initiated. Moreover, the analysis suggests stabilization to dry micro-environmental conditions. This unit is extensively disturbed and bio-reworked through fauna-induced burrowing, resulting in admixed and loose sediments. Although anthropogenic sediments have not been detected in the micro-stratigraphic analyses, the presence of human activities is demonstrated by the relatively high frequencies of lithic artefacts within the upper parts of the SU3, near the cave entrance, at the interface with the overlying SU1 (Nora et al., 2025). These deposits are partially translocated through the grain flows and the strongly expressed bioturbation.

The SU2 corresponds to the last rockfall event through the erosion of the cliff and marks the upper part of the entrance debris cone which created a natural barrier for the deposition of material inside the cave. The sedimentation of most of the SU1 (SU1.3 and 1.2) occurred fairly rapidly via grain flow and rockfall events. Deposition begun shortly before 35.10 ± 2.50 ka and continued until 33.40 ± 2.50 ka, spanning between 0.3 and 8.4 ka. The formation of the upper units has not been geochronologically contrained, but continued until reaching the maximum sediment capacity, dictated by the entrance cone. This possibly resulted in deflation, and partial decrease of the windblown material influx and relatively higher concentration of coarse-grained autochthonous matrices and limestone *éboulis*. Extensive disturbances and mixed depositional regime due to faunal burrowing and human modifications are observed throughout the stratum, causing lateral and vertical re-distribution of Holocene-dated materials in the SU1 (Sherriff et al., 2024). The overlaying Holocene topsoil of the SU0 indicates similar post-depositional processes.

4.2.2. Short-term occupations and the Armenian Highlands

Ararat-1 Cave was occasionally visited by humans during the late Pleistocene. These short-term and infrequent visits were accompanied by combustion activities related to subsistence practices. The presence of ashes and ash pseudomorphs as evidence for the burning of woody materials might reflect the existence of wood-based fuel selection strategies. Conversely, the presence of few burned bone fragments cannot be associated with deliberate use as fuel, nor with systematic bone refusal practices, occasionally proposed for other Palaeolithic sites (Yravedra and Uzquiano, 2013; Cain, 2005; Stiner et al., 1995). Instead, the rather patchy and incidental character suggests accidental incorporation within the hearths, or simple discard following the consumption by human agents (Sanz et al., 2017).

The alternation rates between episodes of human and animal activities at Ararat-1 Cave were relatively fast, as indicated by the close depositional association of anthropogenic deposits and coprolitic matter. The presence of archaeologically sterile micro-layers suggests extended periods of site abandonment, during which small carnivores and herbivores performed prolonged denning (Leierer et al., 2019; Sanz et al., 2017). Micro-stratigraphic evidence highlighting the alternating nature of human-animal occupations in caves are known for other regions, such as the Levant (e.g., Middle Palaeolithic Shovakh Cave, Friesem et al., 2019; Middle-Upper Palaeolithic Sefunim Cave; Friesem et al., 2022). However, similar patterns are almost absent from the Armenian Highlands. Thus, Ararat-1 Cave constitutes one of the rare Middle Palaeolithic examples where low-intensity human occupations

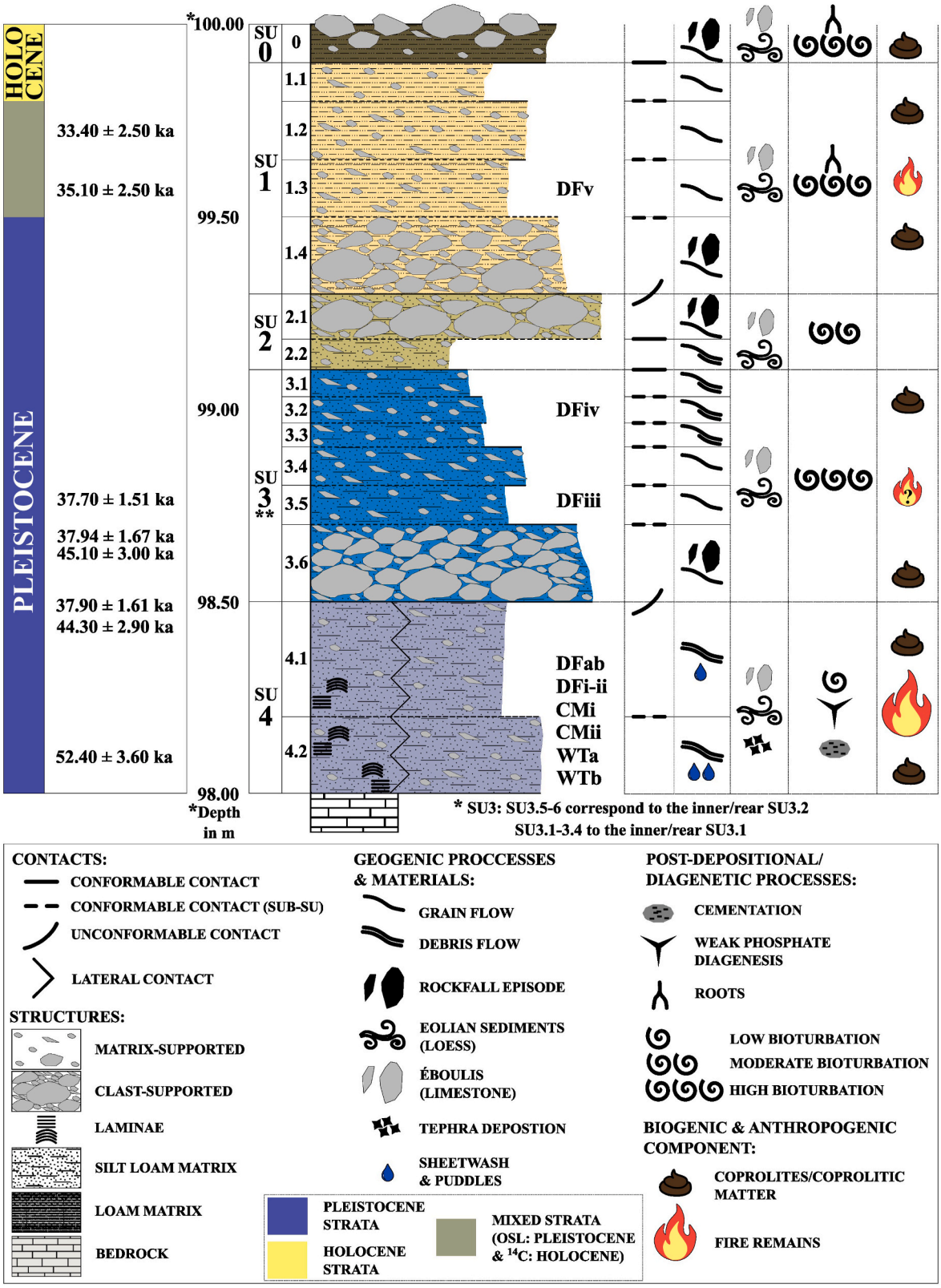

Fig. 16. Synthetic stratigraphic column summarizing the formation processes and materials of Ararat-1 Cave.

and an alternating human-animal relationship is micro-geoarchaeologically manifested.

A comparison with the available well-stratified Middle Palaeolithic cave sites from the broader region often reveals a contrasting pattern. Micromorphological results from Lusakert-1 Cave show evidence for combustion features, possibly indicating high-intensity human use (Wilkinson et al., 2025; Brittingham et al., 2019; Mallol and Goldberg, 2017; Frahm et al., 2016; Adler et al., 2012). Although no micro-stratigraphic data have been reported, Yerevan-1 Cave is associated with high-density and more persistent habitation (Gasparyan et al.,

2014). Conversely, similarly ephemeral patterns are reported for other post-dated cave sequences, such as the Late Middle Palaeolithic Ortvale Klde (Cullen et al., 2021; Moncel et al., 2013) and the Early Upper Palaeolithic Aghitu-3 Cave (Frahm et al., 2019; Kandel et al., 2011, 2017). Upper Palaeolithic hearth with dense ash concentrations and burned lithics is also noted for the former (Cullen et al., 2021).

The presence of ephemeral and low-intensity occupations during the Middle Palaeolithic in the Armenian Highlands has been associated with movement to high-elevation ecological niches (Malinsky-Buller et al. 2021). For instance, the open-air site of Kalavan-2, situated at 1640 m a.s.l., has been linked to seasonal short-term and task-specific occupations (Malinsky-Buller et al., 2021). Ephemeral occupation patterns have also been proposed for the high-altitude Hovk-1 cave, at 2040 m a.s.l. (Pinhasi et al., 2011, 2008; note Bar-Oz et al., 2012 suggesting accumulation as natural pitfall). However, our results from Ararat-1 Cave challenge this model, demonstrating the presence of short-term human visits within the intermediate- to low-altitude, dry eco-zone of the Ararat Depression. The micro-geoarchaeological evidence for ephemeral low-intensity occupations, associated with episodes of combustion and consumption, contribute to our understanding of settlement and mobility pathways, highlighting the amplitude of variation in land exploitation and territorial movement by Middle Palaeolithic polulations in the region.

5. Conclusion

The geoarchaeological analyses of Ararat-1 sequence provide a refined stratigraphic scheme and a renewed reconstruction of the formation processes, highlighting previous gaps in the understanding of site's history. The examination of larger sample size deriving from different parts of the cave reveals differential micro-topographic development between the entrance and the cave interior, indicating dynamic mass movement depositional regimes with both lateral and vertical changes. Evidence for discrete episodes of volcanic tephra and other pyroclastic particle influx via sheetwash processes, preserved in localities within the debris flows, are attested for the first time in the cave. Shifts in the sources of influent sedimentary matter are documented, indicating a noticeable decrease in allochthonous loessic materials accompanied with a progressive increase in autochthonous limestone roofspall deposition. Changes in the micro-environmental conditions, from a slightly fluctuating hydrological regime to a stabilised dry and oxic milieu, are reported. The pronounced effects of bioturbation and animal activity, along with the identification of localised and weakly-developed phosphate-induced alterations contribute to a deeper understanding of the post-depositional and diagenetic processes occurring at the site. Micro-stratigraphic observations from the earliest depositional phases of the cave, within the basal SU4, illustrate short-term, fire-producing human visits, quickly alternated by animal denning. Spatial differentiation in occupation is suggested, as animal denning would be intensified in the rear parts of the cave, while human activities would be more pronounced near the cave entrance.

Our current knowledge of the site's history is the result of a multi-proxy geoarchaeological research framework. Nevertheless, our investigations in Ararat-1 show that integrating both micro-stratigraphic and bulk sediment analyses is vital for an in-depth reconstruction of major or subtle shifts in the depositional processes and sediment influx. The use of context-specific, qualitative micromorphological observations can refine the quantitative data produced by the sedimentological and geochemical techniques. This combined approach reveals informed trends regarding local and allochthonous sediment sources, as well as changes in the depositional mechanisms and micro-environments throughout the sequence. Deciphering formation histories of cave sites, where geogenic processes are the predominant depositional agents and human activities are of low intensity, is an endeavour best achieved through multi-proxy micro-stratigraphic analytical frameworks.

CRediT authorship contribution statement

Ioannis A.K. Oikonomou: (Corresponding author), Conceptualization, Data curation, Formal analysis, Investigation, Methodology, Software, Validation, Visualization, Writing – original draft, Writing – review & editing. **Theodoros Karampaglidis:** Investigation, Data curation, Methodology, Supervision, Validation, Visualization, Writing – review & editing. **Kaja Fenn:** Data curation, Formal analysis, Validation, Writing – review & editing. **Shira Gur-Arieh:** Methodology, Supervision, Validation, Writing – review & editing. **David Nora:** Investigation, Data curation. **Laura Sánchez-Romero:** Writing – review & editing. **Dominik L. Rogall:** Investigation, Data curation. **Delphine Vettese:** Investigation, Data curation. **Boris Gasparyan:** Investigation, Funding acquisition, Project administration, Resources, Writing – review & editing. **Artur Petrosyan:** Investigation, Funding acquisition, Project administration, Resources, Writing – review & editing. **Ariel Malinsky-Buller:** Conceptualization, Investigation, Funding acquisition, Methodology, Project administration, Resources, Supervision, Validation, Writing – original draft, Writing – review & editing.

Declaration of competing interest

The authors declare that they have no known competing financial interests or personal relationships that could have appeared to influence the work reported in this paper.

Acknowledgements

The Authors would like to thank the director of the Institute of Archaeology and Ethnography of the National Academy of Sciences of the Republic of Armenia, Dr. Arsen Bobokhyan, for his support regarding the permits for fieldwork investigations and sample transportation. Ioannis A.K. Oikonomou expresses their sincere gratitude to Dr. P. Karkanas, Dr. D. Michailidis, D. Roussos, Z. Chalatsi and the Wiener Laboratory of the American School of Classical Studies, Dr. D. Friesem, R. Tzukerman and the Environmental Microhistories Laboratory of the University of Haifa, Dr. Y. Ben Dor, Dr. O. Crouvi, Y. Jacobi and the Geological Survey of Israel, Dr. R. Shaar and the Paleomagnetic Laboratory of the Institute of Earth Sciences, the Hebrew University of Jerusalem, N. Paz and the Human-Environment Dynamics Laboratory of the Institute of Archaeology, the Hebrew University of Jerusalem, for providing laboratory facilities and support during the Ararat-1 research. Moreover, Ioannis would like to thank Prof. E. Hovers, Dr. J. Sherriff, Y. Derfner, M. Matvienko, and A. Jallon. The authors extend their sincere thanks to the anonymous reviewers for providing constructive comments that improved this article. Fieldwork, laboratory analyses and syntheses were funded by *TransCause Project, Investigating Pleistocene population dynamics, in the Southern Caucasus* (ERC – Starting Grant Agreement No. 948015), the Fritz-Thyssen Foundation grant for the Project *Pleistocene Hunter-Gatherer Lifeways and Population Dynamics in the Ararat (paleo-lake) Depression, Armenia*, the Bina and Moshe Stekelis Fund for Prehistoric Archaeology, and the Hebrew University International PhD Talent Scholarship.

Appendix A. Supplementary data

Supplementary data to this article can be found online at https://doi.org/10.1016/j.quascirev.2025.109405.

Data availability

All data and/or code is contained within the submission.

References

Abich, H., 1882. Geologie des Armenischen Hochlandes 2. A. Hölder, Wien.

Adamia, S., Zakariadze, G., Chkhotua, T., Sadradze, N., Tsereteli, N., Chabukiani, A., Gventsadze, A., 2011. Geology of the Caucasus: a review. Turk. J. Earth Sci. 20, 489–544. https://doi.org/10.3906/yer-1005-11. (Accessed 19 March 2023). https://instruct.uwo.ca/earth-sci/fieldlog/Caucasus/yer-20-5-1-1005-11.pdf.

Adler, D.S., Bar-Oz, G., 2009. Seasonal patterns of prey acquisition and inter-group competition during the middle and upper palaeolithic of the southern Caucasus. In: Hublin, J.J., Richards, M.P. (Eds.), The Evolution of Hominin Diets: Integrating Approaches to the Study of Palaeolithic Subsistence, pp. 127–140. https://doi.org/10.1007/978-1-4020-9699-0_9. (Accessed 18 February 2023). https://link.springer.com/chapter/10.1007/978-1-4020-9699-0_9.

Adler, D.S., Tushabramishvili, N., 2004. Middle palaeolithic patterns of settlement and subsistence in the southern Caucasus. In: Conard, N.J. (Ed.), Settlement Dynamics of the Middle Paleolithic and Middle Stone Age. Kerns Verlag, Tubingen, pp. 91–132. ISBN 3-935751-01-X Access from (18/02/2023. http://eprints.iliauni.edu.ge/1489/.

Adler, D.S., Belfer-Cohen, A., Bar-Yosef, O., 2006. Between a rock and a hard place: neanderthal-modern human interactions in the southern Caucasus. In: Conard, N.J. (Ed.), *Neanderthals And Modern Humans Meet*, Tübingen Publications in Prehistory. Kerns Verlag, Tübingen, pp. 165–187.

Adler, D.S., Bar-Yosef, O., Belfer-Cohen, A., Tushabramishvili, N., Boaretto, E., Mercier, N., Valladas, H., Rink, W.J., 2008. Dating the demise: neanderthal extinction and the establishment of modern humans in the southern Caucasus. J. Hum. Evol. 55, 817–833. https://doi.org/10.1016/j.jhevol.2008.08.010. (Accessed 14 June 2023). https://www.sciencedirect.com/science/article/pii/S0047248408001632.

Adler, D.S., Yeritsyan, B., Wilkinson, K., Pinhasi, R., Bar-Oz, G., Nahapetyan, S., Mallol, C., Berna, F., Bailey, R., Schmidt, B.A., Glauberman, P., Wales, N., Gasparyan, B., 2012. The Hrazdan gorge Palaeolithic project, 2008-2009. In: Avetisyan, P., Bobokhyan, A. (Eds.), Archaeology Of Armenia in Regional Context, Proceedings Of the International Conference dedicated to the 50th Anniversary of the Institute of Archaeology and Ethnography, National Academy of Sciences of Republic of Armenia. Institute of Archaeology and Ethnography, Gitutyun, Yerevan, pp. 21–37.

Angelucci, D.E., 2017. Lithic artefacts. In: Nicosia, C., Stoops, G. (Eds.), Archaeological Soil and Sediment Micromorphology. John Wiley & Sons Ltd, pp. 223–230.

Angelucci, D.E., Zilhão, J., 2009. Stratigraphy and formation processes of the Upper Pleistocene deposit at Gruta da Oliveira, Almonda karstic system, Torres Novas, Portugal. Geoarchaeology 24, 277–310. https://doi.org/10.1002/gea.20267. (Accessed 19 February 2024). https://onlinelibrary.wiley.com/doi/abs/10.1002/gea.20267.

Arpin, T.L., Mallol, C. & Goldberg, P., Short Contribution: A New Method of Analyzing and Documenting Micromorphological Thin Sections Using Flatbed Scanners: Applications in Geoarchaeological Studies, Geoarchaeology: Int. J. 17:3, 305-313 DOI: https://doi.org/10.1002/gea.10014 Access from (16/August/2023): https://onlinelibrary.wiley.com/doi/10.1002/gea.10014.

Avagyan, A., Sosson, M., Sahakyan, L., Sheremet, Y., Vardanyan, S., Martirosyan, M., Muller, C., 2018. Tectonic evolution of the northern margin of the Cenozoic Ararat basin, lesser Caucasus, Armenia. J. Petrol. Geol. 41 (4), 495–512. https://doi.org/10.1111/jpg.12718. (Accessed 21 June 2023). https://onlinelibrary.wiley.com/doi/10.1111/jpg.12718.

Bailey, G., 2007. Time perspectives, palimpsests and the archaeology of time. J. Anthropol. Archaeol. 26 (2), 198–223. https://doi.org/10.1016/j.jaa.2006.08.002. (Accessed 4 July 2024). https://www.sciencedirect.com/science/article/pii/S0278416506000481.

Bar-Oz, G., Weissbrod, L., Gasparian, B., Nahapetyan, S., Wilkinson & Pinhasi, R., 2012. Taphonomy and zooarchaeology of a high-altitude upper Pleistocene faunal sequence from Hovk-1 cave, Armenia. J. Archaeol. Sci. 39 (7), 2452–2463. https://doi.org/10.1016/j.jas.2012.02.014. (Accessed 28 November 2024). https://www.sciencedirect.com/science/article/pii/S0305440312000787.

Benedetti, M.M., Haws, J.A., Bicho, N.F., Friedl, L., Ellwood, B.B., 2019. Late Pleistocene site formation and paleoclimate at Lapa do Picareiro, Portugal. Journal of Geoarchaeology 34, 698–726. https://doi.org/10.1002/gea.21735. (Accessed 21 December 2024). https://onlinelibrary.wiley.com/doi/full/10.1002/gea.21735.

Berna, F., Behar, A., Shahack-Gross, R., Berg, J., Boaretto, E., Gilboa, A., Sharon, I., Shalev, S., Shilstein, S., Yahalom-Mack, N., Zorn, J.R., Weiner, S., 2007. Sediments exposed to high temperatures: reconstructing pyrotechnological processes in late Bronze and Iron age strata at Tel dor (Israel). J. Archaeol. Sci. 34, 358–373. https://doi.org/10.1016/j.jas.2006.05.011. (Accessed 29 June 2021). https://www.sciencedirect.com/science/article/pii/S0305440306001105.

Bertran, P., Texier, J.P., 1999. Facies and microfacies of slope deposits. Catena 35 (2–4), 99–121. https://doi.org/10.1016/S0341-8162(98)00096-4. (Accessed 11 October 2024). https://www.sciencedirect.com/science/article/pii/S0341816298000964.

Birtwistle, R.J., Yeritsyan, B.G., 2012. Late middle palaeolithic Neanderthal Networks and assemblage variability in Armenia: lithic evidence from Lusakert I rockshelter. LITHICS 33, 5–16. Access from (12/02/2023. http://journal.lithics.org/wp-content/uploads/2021/04/Lithics_33_2012_Birtwistle_and_Yeritsyan.pdf.

Blockley, S., Timms, R.G.O., Flowers, K., Carter-Champion, A., Oikonomou, I.A.K., Karampaglidis, T., Kearney, R.J., Hawkins, H., Sherriff, J.E., Gasparyan, B., Petrosyan, A., Malinsky-Buller, A., 2025. Towards a tephrochronological framework for synchronisation of archaeological records in the southern Caucasus for MIS 3: new data from the Armenian Highlands. Quat. Sci. Rev. this issue.

Bosch, R.F., White, W.B., 2004. Lithofacies and transport for clastic sediments in karst conduits. In: Sasowsky, I.D., Mylroie, J. (Eds.), Studies of Cave Sediments. Springer, Boston, MA. https://doi.org/10.1007/978-1-4419-9118-8_1. (Accessed 8 January 2025). https://link.springer.com/chapter/10.1007/978-1-4419-9118-8_1.

Boschian, G., 1997. Sedimentology and soil micromorphology of the late Pleistocene and early Holocene deposits of Grotta dell'Edera (Trieste karst, NE Italy). Geoarchaeology 12, 227–249. https://doi.org/10.1002/(SICI)1520-6548(199705)12:3<227::AID-GEA3>3.0.CO;2-4Accessfrom(03/04/2025. https://onlinelibrary.wiley.com/doi/10.1002/(SICI)1520-6548(199705)12:3%3C227::AID-GEA3%3E3.0.CO;2-4.

Brittingham, A., Hren, M.T., Hartman, G., Wilkinson, K.N., Mallol, C., Gasparyan, B., Adler, D.S., 2019. Geochemical evidence for the Control of fire by middle palaeolithic Hominins. Sci. Rep. 9, 15368. https://doi.org/10.1038/s41598-019-51433-0. (Accessed 13 February 2023). https://www.nature.com/articles/s41598-019-51433-0.

Brönnimann, D., Ismail-Meyer, K., Rentzel, P., Pümpin, C., Lisá, L., 2017a. In: Nicosia, C., Stoops, G. (Eds.), Archaeological Soil and Sediment Micromorphology. John Wiley & Sons Ltd, Excrements of Herbivores, pp. 55–66.

Brönnimann, D., Pümpin, X., Ismail-Meyer, K., Rentzel, P., Eguez, N., 2017b. Excrements of Omnivores and carnivores. In: Nicosia, C., Stoops, G. (Eds.), Archaeological Soil and Sediment Micromorphology. John Wiley & Sons Ltd, pp. 67–82.

Bull, P.A., 1981. Some fine-grained sedimentation phenomena in caves. Earth Surfaces Processeses and Landforms 6, 11–22. https://doi.org/10.1002/esp.3290060103. (Accessed 9 January 2025). https://onlinelibrary.wiley.com/doi/10.1002/esp.3290060103.

Bullock, P., Fedoroff, N., Jongerius, A., Stoops, G., Tursina, T., 1985. Handbook for Soil Thin Section Description. Waine Reseach Publications, England.

Cain, C.R., 2005. Using burned animal bone to look at Middle Stone Age occupation and behavior. J. Archaeol. Sci. 32 (6), 873–884. https://doi.org/10.1016/j.jas.2005.01.005. (Accessed 12 November 2024). https://www.sciencedirect.com/science/article/pii/S0305440305000208.

Campaña, I., Benito-Calvo, A., Pérez-González, A., Bermúdez de Castro, J.M., Carbonell, E., 2016. Assessing automated image analysis of sand grain shape to identify sedimentary facies, Gran Dolina archaeological site (Burgos, Spain). Sediment. Geol. 346, 72–83. https://doi.org/10.1016/j.sedgeo.2016.09.010. (Accessed 12 May 2023). https://www.sciencedirect.com/science/article/pii/S0037073816302524.

Campaña, I., Benito-Calvo, A., Pérez-González, A., Ortega, A.I., Álvaro-Gallo, A., Miguens-Rodríguez, L., Iglesias-Cibanal, J., Bermúdez de Castro, J.M., Carbonell, E., 2023. Reconstructing depositional environments through cave interior facies: The case of Galería Complex (Sierra de Atapuerca, Spain). Geomorphology 440, 108864. https://doi.org/10.1016/j.geomorph.2023.108864. (Accessed 8 January 2025). https://www.sciencedirect.com/science/article/pii/S0169555X23002842.

Canti, M.G., 1997. An investigation of microscopic calcareous spherulites from herbivore dungs. J. Archaeol. Sci. 24 (3), 219–231. https://doi.org/10.1006/jasc.1996.0105. (Accessed 17 June 2021). https://www.sciencedirect.com/science/article/pii/S0305440396901053.

Canti, M.G., 1998. The micromorphological identification of faecal spherulites from archaeological and modern materials. J. Archaeol. Sci. 25 (5), 435–444. https://doi.org/10.1006/jasc.1997.0210. (Accessed 22 February 2022). https://www.sciencedirect.com/science/article/pii/S0305440397902107.

Canti, M.G., 1999. The production and preservation of faecal spherulites: animals, environment and taphonomy. J. Archaeol. Sci. 26, 251–258. https://doi.org/10.1006/jasc.1998.0322. (Accessed 8 September 2023). https://www.sciencedirect.com/science/article/pii/S0305440398903223?via%3Dihub.

Canti, M.G., 2003. Aspects of the chemical and microscopic characteristics of plant ashes found in archaeological soils. Catena 54 (3), 339–361. https://doi.org/10.1016/S0341-8162(03)00127-9. (Accessed 19 June 2021). https://www.sciencedirect.com/science/article/pii/S0341816203001279.

Canti, M.G., Brochier, J.E., 2017. Faecal spherulites. In: Nicosia, C., Stoops, G. (Eds.), Archaeological Soil and Sediment Micromorphology. John Wiley & Sons Ltd, 51-44.

Carrión, J.S., Gil, G., Rodríguez, E., Fuentes, N., García-Antón, M., Arribas, A., 2005. Palynology of badger coprolites from central Spain. Palaeogeogr. Palaeoclimatol. Palaeoecol. 226 (3–4), 259–271. https://doi.org/10.1016/j.palaeo.2005.05.016. (Accessed 22 October 2024). https://www.sciencedirect.com/science/article/pii/S0031018205002816.

Courty, M.A., 2001. Microfacies analysis assisting archaeological stratigraphy. In: Goldberg, P., Holliday, V.T., Ferring, C.R. (Eds.), Earth Sciences and Archaeology. Springer, Boston, MA. https://doi.org/10.1007/978-1-4615-1183-0_8. (Accessed 18 November 2024). https://link.springer.com/chapter/10.1007/978-1-4615-1183-0_8.

Courty, M.A., Goldberg, P., Macphail, R., 1989. Soils and Micromorphology in Archaeology. Cambridge University Press, Cambridge.

Crouvi, O., Amit, R., Enzel, Y., Porat, N., Sandler, A., 2008. Sand dunes as a major proximal dust source for late Pleistocene loess in the Negev Desert, Israel. Quaternary Research 70, 275–282. https://doi.org/10.1016/j.yqres.2008.04.011. (Accessed 12 December 2021). https://www.sciencedirect.com/science/article/pii/S0033589408000732.

Crouvi, O., Amit, R., Enzel, Y., Gillespie, A.R., 2010. Active sand seas and the formation of desert loess. Quat. Sci. Rev. 29, 17–18. https://doi.org/10.1016/j.quascirev.2010.04.026, 2087-2098. (Accessed 18 October 2024). https://www.sciencedirect.com/science/article/pii/S0277379110001368.

Cullen, V.L., Smith, V.C., Tushabramishvili, N., Mallol, C., Dee, M., Wilkinson, K.N., Adler, D.S., 2021. A revised AMS and tephra chronology for the late middle to early upper Paleolithic occupations of Ortvale Klde, Republic of Georgia. J. Hum. Evol. 151, 102908. https://doi.org/10.1016/j.jhevol.2020.102908. (Accessed 14 June 2023). https://www.sciencedirect.com/science/article/pii/S004724842030169X.

Dasgupta, P., 2003. Sediment gravity flow - the conceptual problems. Earth Sci. Rev. 62 (3–4), 265–281. https://doi.org/10.1016/S0012-8252(02)00160-5Accessfrom(08/01/2025. https://www.sciencedirect.com/science/article/pii/S0012825202001605.

Dean, W.E., 1974. Determination of carbonate and organic matter in calcareous sediments and sedimentary rocks by Loss on Ignition: comparison with other methods. J. Sediment. Petrol. 44 (1), 242–248. https://doi.org/10.1306/74D729D2-2B21-11D7-8648000102C1865D. (Accessed 15 June 2023). https://pubs.geoscienceworld.org/sepm/jsedres/article-abstract/44/1/242/96699/Determination-of-carbonate-and-organic-matter-in?redirectedFrom=fulltext.

Denk, T., Frotzler, N., Davitashvili, N., 2001. Vegetational patterns and distribution of relict taxa in humid temperate forests and wetlands of Georgia (Transcaucasia). Biol. J. Linn. Soc. 72, 287–332. https://doi.org/10.1111/j.1095-8312.2001.tb01318.x. (Accessed 21 February 2023). https://onlinelibrary.wiley.com/doi/abs/10.1111/j.1095-8312.2001.tb01318.x.

Durand, N., Monger, H.C., Canti, M.G., Verrecchia, E.P., 2018. Calcium carbonate features. In: Stoops, G., Marcelino, V., Mees, F. (Eds.), Interpretation of Micromorphological Features of Soils and Regoliths, second ed., pp. 206–257.

Egeland, C.P., Gasparian, B., Arakelyan, D., Nicholson, C.M., Petrosyan, A., Ghukasyan, R., Byerly, R., 2014. Reconnaissance survey for palaeolithic sites in the Debed River valley, northern Armenia. J. Field Archaeol. 39 (4), 370–386. https://doi.org/10.1179/0093469014Z.00000000096. (Accessed 10 November 2024). https://www.tandfonline.com/doi/full/10.1179/0093469014Z.00000000096.

Egeland, C.P., Gasparian, B., Fadem, C.M., Nahapetyan, S., Arakelyan, D., Nicholson, C. M., 2016. Bagrateshen 1, a stratified open-air Middle Paleolithic site in the Debed river valley of northeastern Armenia: a preliminary report. Archaeological Research in Asia 8, 1–20. https://doi.org/10.1016/j.ara.2016.10.001. (Accessed 13 February 2023). https://www.sciencedirect.com/science/article/pii/S2352226716300599?via%3Dihub.

Fayvush, G., Aleksanyan, A., 2021. Plant diversity in riverine wetlands of Armenia. Bocconea 29, 77–89. https://doi.org/10.7320/Bocc29.077. (Accessed 20 February 2023). https://www.herbmedit.org/bocconea/Bocc29_077-089.pdf.

Fayvush, G., Aleksanyan, A., 2022. Climate change and dynamics of vegetation in the lesser Caucasus: an Overview. In: Schickhoff, U., Singh, R.B., Mal, S. (Eds.), Mountain Landscapes in Transition. Effects of Land Use and Climate Change Sustainable Development Goals Series. Climate Action. Springer, pp. 417–428. https://doi.org/10.1007/978-3-030-70238-0_17. (Accessed 7 November 2021). https://link.springer.com/chapter/10.1007/978-3-030-70238-0_17.

Ferro-Vázquez, C., Mallol, C., Aldeias, V., 2021. Simply red? A systematic colour-based method for identifying archaeological fires. Geoarchaeology 1–20. https://doi.org/10.1002/gea.21886. (Accessed 12 June 2023). https://onlinelibrary.wiley.com/doi/10.1002/gea.21886.

Folk, R.L., 1951. Stages of textural maturity in sedimentary rocks. J. Sediment. Res. 21 (3), 127–130. https://doi.org/10.2110/jsr.21.127. (Accessed 23 November 2023). https://pubs.geoscienceworld.org/sepm/jsedres/article-abstract/21/3/127/112793/Stages-of-textural-maturity-in-sedimentary-rocks?redirectedFrom=fulltext.

Folk, R.L., Ward, W.C., 1957. A study in the significance of grain-size parameters. J. Sediment. Petrol. 27 (1), 3–26. https://doi.org/10.1306/74D70646-2B21-11D7-8648000102C1865D. (Accessed 23 June 2023). https://pubs.geoscienceworld.org/sepm/jsedres/article/27/1/3/95232/Brazos-River-bar-Texas-a-study-in-the-significance.

Fourloubey, C., Beauval, C., Cologne, D., Liagre, J., Ollivier, V., Chataigner, C., 2003. Le Paléolithique en Arménie: état des connaissances acquises et données récentes. Paleorient 29 (1), 5–18. Access from (13/02/2023. http://www.digitorient.com/wp/wp-content/uploads/2012/08/Fourloubey-et-al-paleorient-2003.pdf.

Frahm, E., 2017. Scanning electron microscopy. In: Gilbert, A.S. (Ed.), *Encyclopedia of Geoarchaeology. Encyclopedia of Earth Sciences Series*. Springer, Dordrecht, pp. 755–764. https://doi.org/10.1007/978-1-4020-4409-0_25. (Accessed 5 November 2020). https://link.springer.com/referenceworkentry/10.1007/978-1-4020-4409-0_25.

Frahm, E., Feinberg, J.M., Schmidt-Magee, B.A., Wilkinson, K.N., Gasparyan, B., Yeritsyan, B., Adler, D.S., 2016. Middle palaeolithic toolstone procurement behaviors at Lusakert cave 1, Hrazdan valley, Armenia. J. Hum. Evol. 91, 73–92. https://doi.org/10.1016/j.jhevol.2015.10.008. (Accessed 24 October 2024). https://www.sciencedirect.com/science/article/pii/S0047248415002481.

Frahm, E., Kandel, A.W., Gasparyan, B., 2019. Upper palaeolithic settlement and mobility in the Armenian Highlands: agent-based modeling, Obsidian sourcing, and lithic analysis at Aghitu-3 cave. Journal of Paleolithic Archaeology 2, 418–465. https://doi.org/10.1007/s41982-019-00025-5. (Accessed 14 February 2023). https://link.springer.com/article/10.1007/s41982-019-00025-5.

Frahm, E., Nora, D., Gasparyan, B., Petrosyan, A., Malinsky-Buller, A., 2025. Scales of toolstone transport in the Armenian Highlands during MIS 3: the contribution of Ararat-1 Cave (Ararat Depression) to reconstructing opportunities for social interactions. Quat. Sci. Rev. 357, 109324. https://doi.org/10.1016/j.quascirev.2025.109324. (Accessed 8 April 2025). https://www.sciencedirect.com/science/article/pii/S0277379125001441.

French, C.A.I., 2017. Colluvial settings. In: Gilbert, A.S. (Ed.), Encyclopedia of Geoarchaeology. Encyclopedia of Earth Sciences Series. Springer, Dordrecht. https://doi.org/10.1007/978-1-4020-4409-0_153. (Accessed 2 October 2024). https://link.springer.com/referenceworkentry/10.1007/978-1-4020-4409-0_153.

Friesem, D.E., Malinsky-Buller, A., Ekshtain, R., Gur-Arieh, S., Vaks, A., Mercier, N., Richard, M., Guérin, G., Valladas, H., Auger, F., Hovers, E., 2019. New data from Shovakh cave and its implications for reconstructing middle Paleolithic settlement patterns in Amud drainage, Israel. Journal of Paleolithic Archaeology 2, 298–337. https://doi.org/10.1007/s41982-019-00028-2. (Accessed 6 March 2022). https://link.springer.com/article/10.1007/s41982-019-00028-2.

Friesem, D.E., Shahack-Gross, R., Weinstein-Evron, M., Teutsch, N., Weissbrod, L., Shimelmitz, R., 2021. High-resolution of Middle Palaeolithic deposits and formation processes at Tabun Cave, Israel: guano-rich cave deposits and detailed stratigraphic application of Layer C. Quat. Sci. Rev. 274, 107203. https://doi.org/10.1016/j.quascirev.2021.107203, 1-20. (Accessed 15 May 2022). https://www.sciencedirect.com/science/article/pii/S0277379121004108?via%3Dihub.

Friesem, D.F., Shimelmitz, R., Schumacher, M.L., Miller, C.E., Kandel, A.W., 2022. A micro-geoarchaeological view on stratigraphy and site formation processes in the Middle, Upper and Epi-Paleolithic layers of Sefunim Cave, Mt. Carmel, Israel. Archaeol. Anthropol. Sci. 14 (222), 1–22. https://doi.org/10.1007/s12520-022-01686-0. (Accessed 23 June 2022). https://link.springer.com/article/10.1007/s12520-022-01686-0.

Frumkin, A., Langford, B., Marder, O., Ullman, M., 2016. Paleolithic caves and hillslope processes in south-western Samaria, Israel: environmental and archaeological implications. Quat. Int. 398, 246–258. https://doi.org/10.1016/j.quaint.2015.05.064. Access from (13/12/2021): https://www.sciencedirect.com/science/article/pii/S1040618215005844.

Gasparyan, B., 2010. Landscape organization and Resource management in the lower palaeolithic of Armenia. TÜBA-AR 13, 159. Access from (09/02/2023). https://www.tuba.gov.tr/tr/yayinlar/sureli-yayinlar/tuba-ar/tuba-ar-13.

Gasparyan, B., Glauberman, P., 2022. Beyond European boundaries: neanderthals in the Armenian Highlands and the Caucasus. In: Romagnoli, F., Rivals, F., Benazzi, S. (Eds.), Updating Neanderthals: Understanding Behavioural Complexity in the Late Middle Palaeolithic. Elsevier Science & Technology, San Diego, pp. 275–301. https://doi.org/10.1016/B978-0-12-821428-2.00018-4. (Accessed 10 July 2024). https://ebookcentral.proquest.com/lib/huji-ebooks/detail.action?docID=7024347.

Gasparyan, B., Egeland, C.P., Adler, D.S., Pinhasi, R., Glauberman, P., Haydosyan, H., 2014. The middle Paleolithic occupation of Armenia: summarizing old and new data. In: Gasparyan, B., Arimura, M. (Eds.), *Stone Age of Armenia: A Guide-Book to the Stone Age Archaeology in the Republic of Armenia*. Monograph of the JSPS. Kanazawa University Press, Kanazawa, pp. 65–105.

Gevorgyan, H., Repstock, A., Schulz, B., Meliksetian, K., Breitkreuz, C., Israyelyan, A., 2018. Decoding a post-collisional multistage magma system: the Quaternary ignimbrites of Aragats stratovolcano, western Armenia. Lithos 318–319, 267–282. https://doi.org/10.1016/j.lithos.2018.07.024. (Accessed 4 July 2023). https://www.sciencedirect.com/science/article/pii/S0024493718302639?via%3Dihub.

Gevorgyan, H., Breitkreuz, C., Meliksetian, K., Israyelyan, A., Ghukasyan, Y., Pfänder, J. A., Sperner, B., Miggins, D.P., Koppers, A., 2020. Quaternary ring plain- and valley-confined pyroclastic deposits of Aragats stratovolcano (Lesser Caucasus): Lithofacies, geochronology and eruption history. J. Volcanol. Geoth. Res. 401, 106928. https://doi.org/10.1016/j.jvolgeores.2020.106928. (Accessed 4 July 2023). https://www.sciencedirect.com/science/article/pii/S0377027320300639.

Ghazaryan, H.G., 2013. Brief Outline of soils in Armenia. In: Yigini, Y., Panagos, P., Montanarella, L. (Eds.), Soil Resources of Mediterranean and Caucasus Countries. Extension of the European Soil Database. European Commission, Luxembourg. Access from (11/06/2023. https://esdac.jrc.ec.europa.eu/.

Ghukasyan, R., Cologne, D., Nahapetyan, S., Ollivier, V., Gasparyan, B., Monchot, H., Ghataigner, Ch, 2011. Archaeology, Ethnology & Anthropology of Eurasia, 38/4, pp. 39–51. https://doi.org/10.1016/j.aeae.2011.02.003. http://www.digitorient.com/wp/wp-content/uploads/2012/08/Kalavan-2-AEAE-2011.pdf. (Accessed 12 February 2023).

Glauberman, P., Gasparyan, B., Wilkinson, K., Frahm, E., Raczynski-Henk, Y., Haydosyan, H., Arakelyan, D., Karapetian, S., Nahapetyan, S., Adler, D., 2016. Introducing Barozh 12: a middle palaeolithic open-air site on the edge of the Ararat depression, Armenia. ARAMAZD. Armenian Journal of Near Eastern Studies IX 2, 7–20.

Glauberman, P., Gasparyan, B., Sherriff, J., Wilkinson, K., Li, B., Knul, M., Brittingham, A., Hren, M.T., Arakelyan, D., Nahapetyan, S., Raczynski-Henk, Y., Haydosyan, H., Adler, D.S., 2020a. Barozh 12: formation processes of a late Middle Paleolithic open-air site in western Armenia. Quat. Sci. Rev. 236, 106276. https://doi.org/10.1016/j.quascirev.2020.106276. (Accessed 12 February 2023). https://www.sciencedirect.com/science/article/pii/S0277379120302389?via%3Dihub.

Glauberman, P., Gasparyan, B., Wilkinson, K., Frahm, E., Nahapetyan, S., Arakelyan, D., Raczynski-Henk, Y., Haydosyan, H., Adler, D.S., 2020b. Late middle Paleolithic technological organization and behavior at the open-air site of Barozh 12 (Armenia). Journal of Paleolithic Archaeology 3, 1095–1148. https://doi.org/10.1007/s41982-020-00071-4. (Accessed 12 February 2023). https://link.springer.com/article/10.1007/s41982-020-00071-4.

Goder-Goldberger, M., Malinsky-Buller, A., 2022. The initial upper Paleolithic and its place within the middle-to-upper Paleolithic transition of southwest Asia: what hides behind the curtain of taxonomies? Journal of Paleolithic Archaeology 5, 2. https://doi.org/10.1007/s41982-022-00112-0. (Accessed 28 November 2024). https://link.springer.com/article/10.1007/s41982-022-00112-0.

Goldberg, P., Bar-Yosef, O., 1998. Site Formation processes in Kebara and Hayonim caves and their significance in Levantine Prehistoric caves. In: Akazawa, T., Aoki, K., Bar-Yosef, O. (Eds.), Neandertals and Modern Humans in Western Asia. Kluwer Academic Publishers, Plenum Publishers, New York, pp. 107–126.

Goldberg, P., Macphail, R., 2006. Practical and Theoretical Geoarchaeology. Blackwell Publishing, Oxford.

Goldberg, P., Miller, C.E., Schiegl, S., Ligouis, B., Berna, F., Conard, N.J., Wadley, L., 2009. Bedding, hearths, and site maintenance in the middle stone age of Sibudu cave, KwaZulu-Natal, South Africa. Archaeol. Anthropol. Sci. 1, 95–122. https://doi.org/10.1007/s12520-009-0008-1. (Accessed 16 August 2023). https://link.springer.com/article/10.1007/s12520-009-0008-1.

Gray, A.B., Pasternack, G.B., Watson, E.B., 2010. Hydrogen peroxide treatment effects on the particle size distribution of alluvial and marsh sediments. Holocene 20 (2), 293–301. https://doi.org/10.1177/09596836093503. (Accessed 28 December 2021). https://journals.sagepub.com/doi/10.1177/0959683609350390.

Gur-Arieh, S., Shahack-Gross, R., 2020. Ash and dung calcitic micro-remains. In: Henry, A.G. (Ed.), Handbook for the Analysis of Micro-particles in Archaeological

Samples, Interdisciplinary Contributions to Archaeology. Springer, pp. 117–147. https://doi.org/10.1007/978-3-030-42622-4. (Accessed 16 June 2023). https://link.springer.com/book/10.1007/978-3-030-42622-4.
Gur-Arieh, S., Mintz, E., Boaretto, E., Shahack-Gross, R., 2013. An ethnoarchaeological study of cooking installations in rural Uzbekistan: development of a new method for identification of fuel sources. J. Archaeol. Sci. 40, 4331–4347. https://doi.org/10.1016/j.jas.2013.06.001. (Accessed 16 June 2023). https://www.sciencedirect.com/science/article/pii/S0305440313002045.
Heiri, O., Lotter, A.F., Lemcke, G., 2001. Loss on ignition as a method for estimating organiv and carbonate content in sediments: reproducibility and comparability of results. J. Paleolimnol. 25, 101–110. https://doi.org/10.1023/A:1008119611481. (Accessed 14 June 2023). https://link.springer.com/article/10.1023/A:1008119611481.
Horwitz, L.K., Goldberg, P., 1989. A study of Pleistocene and Holocene hyaena coprolites. J. Archaeol. Sci. 16 (1), 71–94. https://doi.org/10.1016/0305-4403(89)90057-5. (Accessed 13 May 2024). https://www.sciencedirect.com/science/article/pii/0305440389900575.
Ismail-Meyer, K., 2017. Plant remains. In: Nicosia, C., Stoops, G. (Eds.), Archaeological Soil and Sediment Micromorphology. John Wiley & Sons Ltd, pp. 121–136.
Kandel, A.W., Gasparyan, B., Bruch, A.A., Weissbrod, L., Zardaryan, D., 2011. Introducing Aghitu-3, the first upper Paleolithic cave site in Armenia, 2011. Armenian Journal of Near Eastern Studies (ARAMAZD) VI 2, 7–23. Yerevan.
Kandel, A.W., Gasparyan, B., Nahapetyan, S., Taller, A., Weissbrod, L., 2014. The upper Paleolithic settlement of the Armenian Highlands. Eraul 140, 39–60.
Kandel, A.W., Gasparyan, B., Allué, E., Bigga, G., Bruch, A.A., Cullen, V.L., Frahm, E., Ghukasyan, R., Gruwier, B., Jabbour, F., Miller, C.E., Taller, A., Vardazaryan, V., Vasilyan, D., Weissbrod, L., 2017. The earliest evidence for upper Paleolithic occupation in the Armenian Highlands at Aghitu-3 cave. J. Hum. Evol. 110, 37–68. https://doi.org/10.1016/j.jhevol.2017.05.010. (Accessed 14 February 2023). https://www.sciencedirect.com/science/article/pii/S004724841630269X?via%3Dihub.
Karampaglidis, T., Fenn, K., Gasparyan, B., Braucher, R., Lauer, T., Vainer, S., Gevorgyan, H., Arakelyan, D., Oikonomou, I., Haydosyan, H., Rogall, D., Carrasco, R.M., Pedraza, J., Petrosyan, A., Malinsky-Buller, A., 2025. Paleolithic hominin occupations and Quaternary geomorphological evolution in the NE Ararat Depression (Armenia). Quat. Sci. Rev. this issue.
Karkanas, P., 2017. Guano. In: Nicosia, C., Stoops, G. (Eds.), Archaeological Soil and Sediment Micromorphology. John Wiley & Sons Ltd, pp. 83–90.
Karkanas, P., Goldberg, P., 2017. Soil micromorphology. In: Gilbert, A.S. (Ed.), Encyclopedia of Geoarchaeology. Encyclopedia of Earth Sciences Series. Springer, Dordrecht, pp. 830–841. https://doi.org/10.1007/978-1-4020-4409-0_27. (Accessed 20 May 2021). https://link.springer.com/referenceworkentry/10.1007/978-1-4020-4409-0_27.
Karkanas, P., Goldberg, P., 2018. Phosphatic features. In: Stoops, G., Marcelino, V., Mees, F. (Eds.), Interpretation of Micromorphological Features of Soils and Regoliths, second ed., pp. 323–346.
Karkanas, P., Goldberg, P., 2019. Reconstructing Archaeological Sites: Understanding the Geoarchaeological Matrix. Wiley-Blackwell.
Karkanas, P., Kyparissi-Apostolika, N., 2024. Revisiting palaeolithic combustion features of Theopetra Cave: a diachronic use of dung and peat as fuel. J. Archaeol. Sci. 165, 105958. https://doi.org/10.1016/j.jas.2024.105958. (Accessed 4 July 2024). https://www.sciencedirect.com/science/article/pii/S0305440324000244.
Karkanas, P., Kyparissi-Apostolika, N., Bar-Yosef, O., Weiner, S., 1999. Mineral assemblages in Theopetra, Greece: a framework for understanding diagenesis in a Prehistoric cave. J. Archaeol. Sci. 26 (9), 1171–1180. https://doi.org/10.1006/jasc.1998.0354. (Accessed 30 March 2022). https://www.sciencedirect.com/science/article/pii/S0305440398903545.
Karkanas, P., Bar-Yosef, O., Goldberg, P., Weiner, S., 2000. Diagenesis in Prehistoric caves: the Use of minerals that form in situ to assess the completeness of the archaeological record. J. Archaeol. Sci. 27 (10), 915–929. https://doi.org/10.1006/jasc.1999.0506. (Accessed 30 March 2022). https://www.sciencedirect.com/science/article/pii/S030544039990506X.
Karkanas, P., Shahack-Gross, R., Ayalon, A., Bar-Matthews, M., Barkai, R., Frumkin, A., Gopher, A., Stiner, M.C., 2007. Evidence for habitual use of fire at the end of the lower palaeolithic: site-formation processes at Qesem cave, Israel. J. Hum. Evol. 53, 197–212. https://doi.org/10.1016/j.jhevol.2007.04.002. (Accessed 10 July 2021). https://www.sciencedirect.com/science/article/pii/S004724840700084X.
Karkanas, P., Brown, K.S., Fisher, E.C., Jacobs, Z., Marean, C.W., 2015a. Interpreting human behavior from depositional rates and combustion features through the study of sedimentary microfacies at site Pinnacle Point 5-6, South Africa. J. Hum. Evol. 85, 1–21. https://doi.org/10.1016/j.jhevol.2015.04.006. (Accessed 22 February 2022). https://www.sciencedirect.com/science/article/pii/S0047248415001037?via%3Dihub.
Karkanas, P., White, D., Lane, C.S., Stringer, C., Davies, W., Cullen, V.L., Smith, V.C., Ntinou, M., Tsartsidou, G., Kyparissi-Apostolika, N., 2015b. Tephra correlations and climatic events between the MIS6/5 transition and the beginning of MIS3 in Theopetra Cave, central Greece. Quat. Sci. Rev. 118, 170–181. https://doi.org/10.1016/j.quascirev.2014.05.027. (Accessed 13 August 2024). https://www.sciencedirect.com/science/article/pii/S027737911400208X.
Kirscher, U., Gevorgyan, H., Meliksetian, K., Navasardyan, G., Dallanave, E., Breitkreuz, C., Bachtadse, V., 2020. Pleistocene ignimbrites of western Armenia - Paleomagnetic and magnetic anisotropy constraints on flow direction and stratigraphy. J. Volcanol. Geoth. Res. 402, 106982. https://doi.org/10.1016/j.jvolgeores.2020.106982. (Accessed 4 July 2023). https://www.sciencedirect.com/science/article/pii/S0377027320301682.
Krajcarz, M.T., Cyrek, K., Krajcarz, M., Mroczek, P., Sudoł, M., Szymanek, M., Tomek, T., Madeyska, T., 2016. Loess in a cave: Lithostratigraphic and correlative value of loess and loess-like layers in caves from the Kraków-Częstochowa Upland (Poland). Quat. Int. 399, 13–30. https://doi.org/10.1016/j.quaint.2015.08.069. (Accessed 18 March 2024). https://www.sciencedirect.com/science/article/pii/S1040618215008472.
Lebedev, V.A., Chernyshev, I.V., Yakushev, A.I., 2011. Initial time and Duration of Quaternary magmatism in the Aragats Neovolcanic area (lesser Caucasus, Armenia). Dokl. Earth Sci. 437 (2), 532–536. https://doi.org/10.1134/S1028334X11040209. (Accessed 19 March 2023). https://link.springer.com/article/10.1134/S1028334X11040209.
Leierer, L., Jambrina-Enríquez, M., Herrera-Herrera, A.V., Connolly, R., Hernández, C. M., Galván, B., Mallol, C., 2019. Insights into the timing, intensity and natural setting of Neanderthal occupation from the geoarchaeological study of combustion structures: a micromorphological and biomarker investigation of El Salt, unit Xb, Alcoy, Spain. PLoS One 14 (4), e0214955. https://doi.org/10.1371/journal.pone.0214955. (Accessed 9 March 2022). https://journals.plos.org/plosone/article?id=10.1371/journal.pone.0214955.
Lisiecki, L.E., Raymo, M.E., 2005. A Pliocene-Pleistocene stack of 57 globally distributed benthic $\delta^{18}O$ records. Paleoceanography 20, PA1003. https://doi.org/10.1029/2004PA001071. (Accessed 14 October 2024). https://agupubs.onlinelibrary.wiley.com/doi/10.1029/2004PA001071.
Lomax, J., Wolf, D., Wolpert, T., Sahakyan, Lilit, Hovakimyan, H., Faust, D., Fuchs, M., 2021. Establishing a luminescence-based Chronostratigraphy for the last glacial-Interglacial cycle of the loess-palaeosol sequence Achajur (Armenia). Front. Earth Sci. 9, 755084. https://doi.org/10.3389/feart.2021.755084. (Accessed 21 March 2023). https://www.frontiersin.org/articles/10.3389/feart.2021.755084/full.
Malinsky-Buller, A., Hovers, E., Marder, O., 2011. Making time: 'Living floors', 'palimpsests' and site formation processes – a perspective from the open-air Lower Paleolithic site of Revadim Quarry, Israel. J. Anthropol. Archaeol. 30 (2), 89–101. https://doi.org/10.1016/j.jaa.2010.11.002. (Accessed 23 February 2022). https://www.sciencedirect.com/science/article/pii/S0278416510000632?via%3Dihub.
Malinsky-Buller, A., Glauberman, P., Wilkinson, K., Li, B., Frahm, E., Gasparyan, B., Timms, R., Adler, D.S., Sherriff, J., 2020. Evidence for Middle Palaeolithic occupation and landscape change in central Armenia at the open-air site of Alapars-1. Quaternary Research 99, 223–247. https://doi.org/10.1017/qua.2020.61. https://www.cambridge.org/core/journals/quaternary-research/article/abs/evidence-for-middle-palaeolithic-occupation-and-landscape-change-in-central-armenia-at-the-openair-site-of-alapars1/6613BBC6CF1348486F75BC98D71D5FFE. (Accessed 14 June 2023).
Mallol, C., Goldberg, P., 2017. Cave and rock Shelter sediments. In: Nicosia, C., Stoops, G. (Eds.), Archaeological Soil and Sediment Micromorphology. John Wiley & Sons Ltd, pp. 359–382.
Mallol, C., Mentzer, S.M., Miller, C.E., 2017. Combustion features. In: Nicosia, C., Stoops, G. (Eds.), Archaeological Soil and Sediment Micromorphology. John Wiley & Sons Ltd, pp. 299–330.
Mallol, C., Hernández, C., Mercier, N., Falguères, C., Carrancho, Á., Cabanes, D., Vidal-Matutano, P., Connolly, R., Pérez, L., Mayor, A., Ben Arous, E., Galván, B., 2019. Fire and brief human occupations in Iberia during MIS 4: Evidence from Abric del Pastor (Alcoy, Spain). Sci. Rep. 9, 18281. https://doi.org/10.1038/s41598-019-54305-9. (Accessed 15 July 2024). https://www.nature.com/articles/s41598-019-54305-9.
McLean, D., Albert, P.G., Nakagawa, T., Suzuki, T., Staff, R.A., Yamada, K., Kitaba, I., Haraguchi, T., Kitagawa, J., Smith, V.C., 2018. Integrating the Holocene tephrostratigraphy for East Asia using a high-resolution cryptotephra study from Lake Suigetsu (SG14 core), central Japan. Quat. Sci. Rev. 183, 36–58. https://doi.org/10.1016/j.quascirev.2017.12.013. (Accessed 20 October 2024). https://www.sciencedirect.com/science/article/pii/S0277379117306789.
Meignen, L., Tushabramishvili, N., 2007. Paléolithic moyen Laminaire sur les flancs Sud du Caucase: productions ithiques et fonctionnement du site de Djruchula Géorgie. Paleorient 32, 81–104. Access from (08/07/2024. https://www.persee.fr/doc/paleo_0153-9345_2006_num_32_2_5191.
Meignen, L., Tushabramishvili, N., 2010. Djruchula cave, on the southern slopes of the Great Caucasus: an extension of the near eastern middle Paleolithic blady phenomenon to the north. Journal of the Israel Prehistoric Society 40, 35–61.
Mentzer, S.M., 2017. Hearths and combustion features. In: Gilbert, A.S. (Ed.), Encyclopedia of Geoarchaeology. Encyclopedia of Earth Sciences Series. Springer, Dordrecht, pp. 411–424. https://doi.org/10.1007/978-1-4020-4409-0_133. (Accessed 26 May 2021). https://link.springer.com/referenceworkentry/10.1007%2F978-1-4020-4409-0_133.
Menzies, J., Zaniewski, K., 2003. Microstructures within a modern debris flow deposit derived from Quaternary glacial diamicton – a comparative micromorphological study. Sediment. Geol. 157, 31–48. https://doi.org/10.1016/S0037-0738(02)00193-8. https://www.sciencedirect.com/science/article/pii/S0037073802001938?via%3Dihub.
Mercier, N., Valladas, H., Meignen, L., Joron, J.-L., Tushabramishvili, N., Adler, D.S., Bar-Yosef, O., 2010. Dating the early middle palaeolithic laminar Industry from Djruchula cave, Republic of Georgia. Paleorient 36 (2), 163–173. https://doi.org/10.3406/paleo.2010.5393. (Accessed 10 August 2023). https://www.persee.fr/doc/paleo_0153-9345_2010_num_36_2_5393.
Moncel, M.-H., Pleurdeau, D., Tushubramishvili, N., Yeshurun, R., Agapishvili, T., Pinhasi, R., Higham, T.F.G., 2013. Preliminary results from the new excavations of the middle and upper palaeolithic levels at Ortvale Klde-north chamber (south Caucasus Georgia). Quat. Int. 316, 3–13. https://doi.org/10.1016/j.quaint.2012.09.012. (Accessed 11 August 2023). https://www.sciencedirect.com/science/article/pii/S1040618212031850?via%3Dihub.
Mücher, H., van Steijn, H., Kwaad, F., 2018. Colluvial and mass Wasting deposits. In: Stoops, G., Marcelino, V., Mess, F. (Eds.), Interpretation of Micromorphological

Features of Soils and Regoliths, second ed. Elsevier, pp. 21–36. https://doi.org/10.1016/B978-0-444-63522-8.00002-4 (Accessed 11 October 2024) https://www.sciencedirect.com/science/article/pii/B9780444635228000024.

Lane, C.S., Cullen, V.L., White, D., Bramham-Law, C.W.F., Smith, V.C., 2014. Cryptotephra as a dating and correlation tool in archaeology. J. Archaeol. Sci. 42, 42–50. https://doi.org/10.1016/j.jas.2013.10.033. Access from (17/October/2024): https://www.sciencedirect.com/science/article/pii/S0305440313003804.

Malinsky-Buller, A., Glauberman, P., Ollivier, V., Lauer, T., Timms, R., Frahm, E., Brittingham, A., Triller, B., Kindler, L., Knul, M.V., Krakovsky, M., Joannin, S., Hren, M.T., Bellier, O., Clark, A.A., Blockley, S.P.E., Arakelyan, D., Marreiros, J., Paixaco, E., Calandra, I., Ghukasyan Nora, D., Nir, N., Adigyozalyan, A., Haydosyan, H., Gasparyan, B., 2021. Short-term occupations at high elevation during the Middle Paleolithic at Kalavan 2 (Republic of Armenia). PLOS ONE 16 (2), e0245700. https://doi.org/10.1371/journal.pone.0245700. Access from: https://journals.plos.org/plosone/article?id=10.1371/journal.pone.0245700 (1-59).

Malinsky-Buller, A., Glauberman, P., Ollivier, V., Lauer, T., Timms, R., Frahm, E., Brittingham, A., Triller, B., Kindler, L., Knul, M.V., Krakovsky, M., Joannin, S., Hren, M.T., Bellier, O., Clark, A.A., Blockley, S.P.E., Arakelyan, D., Marreiros, J., Paixaco, E., Calandra, I., Ghukasyan Nora, D., Nir, N., Adigyozalyan, A., Haydosyan, H., Gasparyan, B., 2021. Short-term occupations at high elevation during the Middle Paleolithic at Kalavan 2 (Republic of Armenia). PLoS One 16 (2), e0245700. https://doi.org/10.1371/journal.pone.0245700. Access from: https://journals.plos.org/plosone/article?id=10.1371/journal.pone.0245700 (1-59).

Nora, D., Frahm, E., Oikonomou, I.A.K., Karampaglidis, T., Petrosyan, A., Gasparyan, B., Malinsky-Buller, A., 2025. the Role of lithic technology in shaping mobility and decision-making: the case of Ararat-1 cave. Quat. Sci. Rev. this issue.

Ogloblin Ramirez, I., Dunseth, Z.C., Shalem, D., Shahack-Gross, R., 2023. Infrared spectra of mixtures of heated and unheated clay: solving an interpretational conundrum. Geoarchaeology 38, 822–829. https://doi.org/10.1002/gea.21976. Access from (03/01/2025): https://onlinelibrary.wiley.com/doi/10.1002/gea.21976.

Oikonomou, I.A.K., 2023. Deciphering anthropo-sedimentary processes and ash micro-histories at the Neolithic lakeside settlement of Dispilio, Greece: a micro-geoarchaeological approach. J. Archaeol. Sci. Rep. 49, 103948. https://doi.org/10.1016/j.jasrep.2023.103948. Access from (19/06/2023): https://www.sciencedirect.com/science/article/pii/S2352409X23001232.

Oswald, F., 1906. A Treatise on the Geology of Armenia. University of London, Ioana, Beston, Netts.

Philips, E., 2006. Micromorphology of a debris flow deposit: evidence of basal shearing, hydrofracturing, liquefaction and rotational deformation during emplacement. Quat. Sci. Rev. 25, 720–738. https://doi.org/10.1016/j.quascirev.2005.07.004. https://www.sciencedirect.com/science/article/pii/S0277379105002003.

Pinhasi, R., Gasparian, B., Wilkinson, K., Bailey, R., Bar-Oz, G., Bruch, A., Chataigner, C., Hoffmann, D., Hovsepyan, R., Nahapetyan, S., Pike, A.W.G., Schreve, D., Stephens, M., 2008. Hovk 1 and the middle and upper Paleolithic of Armenia: a preliminary framework. J. Hum. Evol. 55, 803–816. https://doi.org/10.1016/j.jhevol.2008.04.005. (Accessed 13 June 2023). https://www.sciencedirect.com/science/article/pii/S0047248408000870?via%3Dihub.

Pinhasi, R., Gasparian, B., Nahapetyan, S., Bar-Oz, G., Leissbrod, L., Bruch, A.A., Hovsepyan, R., Wilkinson, K., 2011. Middle Palaeolithic human occupation of the high altitude region of Hovk-1, Armenia. Quat. Sci. Rev. 30, 3846–3857. https://doi.org/10.1016/j.quascirev.2011.09.020. (Accessed 13 June 2023). https://www.sciencedirect.com/science/article/pii/S027737911100299X?via%3Dihub.

Pye, K., 1995. The nature, origin and accumulation of loess. Quat. Sci. Rev. 14 (7–8), 653–667. https://doi.org/10.1016/0277-3791(95)00047-X. (Accessed 2 April 2025). https://www.sciencedirect.com/science/article/pii/027737919500047X.

Pye, K., Tsoar, H., 2009. Aeolian Sand and Sand Dunes. Springer, Berlin, Heidelberg. https://doi.org/10.1007/978-3-540-85910-9. (Accessed 14 September 2024). https://link.springer.com/book/10.1007/978-3-540-85910-9.

Regev, L., Poduska, K.M., Addadi, L., Weiner, S., Boaretto, E., 2010. Distinguishing between calcites formed by different mechanisms using infrared spectrometry: archaeological applications. J. Archaeol. Sci. 37 (12), 3022–3029. https://doi.org/10.1016/j.jas.2010.06.027. (Accessed 18 August 2021). https://www.sciencedirect.com/science/article/pii/S0305440310002244.

Rentzel, P., Nicosia, C., Gebhardt, A., Brönnimann, D., Pümpin, C., Ismail-Meyer, K., 2017. Trampling, Poaching and the effect of traffic. In: Nicosia, C., Stoops, G. (Eds.), Archaeological Soil and Sediment Micromorphology. John Wiley & Sons, pp. 281–297.

Rogall, D.L., Hugues-Alexandre Blain, M.A., Oikonomou, I.A.K., Karampaglidis, T., Petrosyan, A., Gasprayan, B., Malinsky-Buller, A., 2025. comparing past and present. The Holocene and marine Isotope stage 3 microvertebrate assemblage of Ararat-1 cave, Armenia. Quat. Sci. Rev. this issue.

Röpke, A., Dietl, C., 2017. Burnt soils and sediments. In: Nicosia, C., Stoops, G. (Eds.), Archaeological Soil and Sediment Micromorphology. John Wiley & Sons Ltd, pp. 173–180. Orangish/reddish silty clay aggregates present, but unclear if related to burning.

Ruggieri, R., Davtyan, S., Shahinyan, S., Ugujyan, A., Orsini, R., Ingallinera, A., Agosta, G., 2022. Armenian karst project. Carbonates Evaporites 37 (14), 1–20. https://doi.org/10.1007/s13146-021-00755-0. Access from (04/01/2023. https://link.springer.com/article/10.1007/s13146-021-00755-0.

Sanz, M., Daura, J., Égüez, N., Brugal, J.P., 2016. Not only hyenids: A multi-scale analysis of Upper Pleistocene carnivore coprolites in Cova del Coll Verdaguer (NE Iberian Peninsula. Palaeogeogr. Palaeoclimatol. Palaeoecol. 443, 249–262. https://doi.org/10.1016/j.palaeo.2015.11.047. (Accessed 17 October 2024). https://www.sciencedirect.com/science/article/pii/S0031018215007178.

Sanz, M., Daura, J., Égüez, N., Cabanes, D., 2017. On the track of anthropogenic activity in carnivore dens: Altered combustion structures in Cova del Gegant (NE Iberian Peninsula). Quat. Int. 437 (B), 102–114. https://doi.org/10.1016/j.quaint.2015.10.057. (Accessed 11 November 2024). https://www.sciencedirect.com/science/article/pii/S104061821501040X.

Schiegl, S., Goldberg, P., Bar-Yosef, O., Weiner, S., 1996. Ash deposits in Hayonim and Kebara caves, Israel: macroscopic, microscopic and mineralogical observations, and their archaeological implications. J. Archaeol. Sci. 23, 763–781. https://doi.org/10.1006/jasc.1996.0071. (Accessed 24 June 2021). https://www.sciencedirect.com/science/article/pii/S0305440396900710?via%3Dihub.

Schiegl, S., Goldberg, P., Pfretzschner, H.-U., Conard, N.J., 2003. Paleolithic burnt bone horizons from the Swabian Jura: Distinguishing between in situ fireplaces and dumping areas. Geoarchaeology: Int. J. 18 (5), 541–565. https://doi.org/10.1002/gea.10080. (Accessed 16 August 2023). https://onlinelibrary.wiley.com/doi/10.1002/gea.10080.

Shahack-Gross, R., 2011. Herbivorous livestock dung: formation, taphonomy, methods for identification, and archaeological significance. J. Archaeol. Sci. 38 (2), 205–218. https://doi.org/10.1016/j.jas.2010.09.019. (Accessed 12 July 2024). https://www.sciencedirect.com/science/article/pii/S0305440310003419.

Sherriff, J.E., Petrosyan, A., Rogall, D., Nora, D., Frahm, E., Lauer, T., Karambaglidis, Knul, M.V., Vettese, D., Arakelyan, D., Gur-Arieh, S., Vidal-Matutano, P., Morales, J., Fewlass, H., Blockley, S.P.E., Timms, R., Adigyozalyan, A., Haydosyan, H., Glauberman, P., Gasparyan, B., Malinsky-Buller, A., 2024. Preprint, Palaeoenvironmental and chronological context of hominin occupations of the Armenian Highlands during MIS 3: evidence from Ararat-1 cave. Quaternary Science Advances 13, 100122. https://doi.org/10.1016/j.qsa.2023.100122. (Accessed 4 July 2024). https://www.sciencedirect.com/science/article/pii/S2666033423000540?via%3Dihub.

Sherwood, S.C., Goldberg, P., 2001. A geoarchaeological framework for the study of karstic cave sites in the eastern woodlands. Midcont. J. Archaeol. 26 (2), 145–167. http://www.jstor.org/stable/20708157. (Accessed 27 September 2022). https://www.jstor.org/stable/20708157.

Stiner, M.C., Kuhn, S.L., Weiner, S., Bar-Yosef, O., 1995. Differential burning, recrystallization, and fragmentation of archaeological bone. J. Archaeol. Sci. 22 (2), 223–237. https://doi.org/10.1006/jasc.1995.0024. (Accessed 12 November 2024). https://www.sciencedirect.com/science/article/pii/S0305440385700246.

Stoops, G., 2017. Fluorescence microscopy. In: Nicosia, C., Stoops, G. (Eds.), Archaeological Soil and Sediment Micromorphology. John Wiley & Sons Ltd, pp. 393–398.

Stoops, G., 2021. Guidelines for Analysis and Description of Soil and Regolith Thin Sections, 2nd ed. John Wiley & Sons.

Stoops, G., Nicosia, C., 2017. Sampling for soil micromorphology. In: C., Nicosia & G., Stoops, *Archaeological Soil And Sediment Micromorphology*. Wiley, pp. 385–391.

Thomsen, K.J., Murray, A.S., Jain, M., Bøtter-Jensen, L., 2008. Laboratory fading rates of various luminescence signals from feldspar-rich sediment extracts. Radiat. Meas. 43, 1474–1486. https://doi.org/10.1016/j.radmeas.2008.06.002.

Tsoar, H., Pye, K., 1987. Dust transport and the question of desert loess formation. Sedimentology 34, 139–153. https://doi.org/10.1111/j.1365-3091.1987.tb00566.x. (Accessed 28 September 2024). https://onlinelibrary.wiley.com/doi/10.1111/j.1365-3091.1987.tb00566.x.

Tudyka, K., Bluszcz, A., Poręba, G., Miłosz, S., Adamiec, G., Kolarczyk, A., Kolb, T., Lomax, J., Fuchs, M., 2020. Increased dose rate precision in combined α and β counting in the μDose system - a probabilistic approach to data analysis. Radiat. Meas. 134. https://doi.org/10.1016/j.radmeas.2020.106310.

Tudyka, K., Koruszowic, M., Osadnik, R., Adamiec, G., Moska, P., Szymak, A., Bluszcz, A., Zhang, J., Kolb, T., Poręba, G., 2023. μRate: An online dose rate calculator for trapped charge dating. Archaeometry 65, 423–443. https://doi.org/10.1111/arcm.12828.

Valder, J.F., Carter, J.M., Medler, C.J., Thompson, R.F., Anderson, M.T., 2018. Hydrogeologic framework and groundwater conditions of the Ararat Basin in Armenia. Scientific Investigations Report 2017-5163, U.S. Geological Survey. https://doi.org/10.3133/sir20175163. (Accessed 22 March 2023). https://pubs.er.usgs.gov/publication/sir20175163.

Vaquero, M., 2008. The history of stones: behavioural inferences and temporal resolution of an archaeological assemblage from the Middle Palaeolithic. J. Archaeol. Sci. 35 (12), 3178–3185. https://doi.org/10.1016/j.jas.2008.07.006. (Accessed 7 March 2022). https://www.sciencedirect.com/science/article/pii/S0305440308001623.

Vepraskas, M.J., Lindbo, D.L., Stolt, M.H., 2018. Redoximorphic features. In: Stoops, G., Marcelino, V., Mees, F. (Eds.), Interpretation of Micromorphological Features of Soils and Regoliths, second ed., pp. 425–445.

Villagran, X.S., Huisman, D.J., Mentzer, S.M., Miller, C.E., Jans, M.M., 2017. Bone and other skeletal tissues. In: Nicosia, C., Stoops, G. (Eds.), Archaeological Soil and Sediment Micromorphology. John Wiley & Sons, pp. 11–38.

Volodicheva, N., 2002. The Caucasus. In: Shahgedanova, M. (Ed.), The Physical Geography of Northern Eurasia, Oxford Regional Environments. Oxford University Press, New York, pp. 350–376.

Weiner, S., 2010. Microarchaeology. Beyond the Visible Archaeological Record. Cambridge University Press. https://doi.org/10.1017/CBO9780511811210. https://www.cambridge.org/core/books/microarchaeology/90A54AACBA0B4ADD7412F43EC91B91B9. (Accessed 7 June 2021).

Weiner, S., Goldberg, P., Bar-Yosef, O., 2002. Three-dimensional distribution of minerals in the sediments of Hayonim cave, Israel: diagenetic processes and archaeological implications. J. Archaeol. Sci. 29 (11), 1289–1308. https://doi.org/10.1006/jasc.2001.0790. (Accessed 30 March 2022). https://www.sciencedirect.com/science/article/pii/S0305440301907903.

Weller, J.N., Martin, A.J., Connor, C.B., Connor, L.J., Karakhanian, A., 2006. Modelling the spatial distribution of volcanoes: example from Armenia. Statistics in Volcanology 1, 1–20. https://doi.org/10.1144/IAVCEI001.7. (Accessed 21 February 2023). https://pubs.geoscienceworld.org/gsl/books/book/1732/chapter-abstract/107594440/Modelling-the-spatial-distribution-of-volcanoesan?redirectedFrom=fulltext.

Williams, L., 2004. Caucasus Biodiversity Hotspot. Access from (11/06/2023. https://www.cepf.net/our-work/biodiversity-hotspots/caucasus.

Shillito, L.-M., Blong, J.C., Green, E.J., van Asperen, E.N., 2020. The what, how and why of archaeological coprolite analysis. Earth Sci. Rev. 207, 103196. https://doi.org/10.1016/j.earscirev.2020.103196. Access from (18/October/2004): https://www.sciencedirect.com/science/article/pii/S0012825220302427.

Wilkinson, K.N., Allué, E., Armitage, S.J., van Arsdale, A., Bar-Oz, G., Brittingham, A., Gasparyan, B., Gill, J., Glauberman, P., Higham, T.F.G., Frahm, E., Kovach, T., Lukich, V., Mallol, C., Raczynski-Henk, Y., Rey Rodríguez, I., Sherriff, J.E., Srivastava, A., Weissbrod, L., Yeshurun, R., Adler, D.S., 2025. The geoarchaeology, chronology and environment of Lusakert-1, a Late Middle Palaeolithic rockshelter (Kotayk Province, Armenia). Quat. Environ. Humans 3 (1), 100054. https://doi.org/10.1016/j.qeh.2024.100054. Access from (10/01/2025): https://www.sciencedirect.com/science/article/pii/S2950236524000525.

Wolf, D., Lomax, J., Sahakyan, L., Hovakimyan, H., Profe, J., Schulte, P., Suchodoletz, H., Richter, C., Hambach, U., Fuchs, M., Faust, D., 2022. Last glacial loess dynamics in the Southern Caucasus (NE-Armenia) and the phenomenon of missing loess deposition during MIS-2. Sci. Rep. 12, 13269. https://doi.org/10.1038/s41598-022-17021-5. (Accessed 21 March 2023). https://www.nature.com/articles/s41598-022-17021-5.

Yravedra, J., Uzquiano, P., 2013. Burnt bone assemblages from El Esquilleu cave (Cantabria, Northern Spain): deliberate use for fuel or systematic disposal of organic waste? Quat. Sci. Rev. 68, 175–190. https://doi.org/10.1016/j.quascirev.2013.01.019. (Accessed 12 November 2024). https://www.sciencedirect.com/science/article/pii/S0277379113000280.

Zeinalov, A.A., Valiev, S.S., Tagieva, E.N., 2010. Human environment in the Nakhichevan region during the Mousterian (based on the Gazma cave site, Azerbaijan). Archaeol. Ethnol. Anthropol. Eurasia 38 (2), 2–6. https://doi.org/10.1016/j.aeae.2010.08.002. (Accessed 23 February 2023). https://www.sciencedirect.com/science/article/abs/pii/S1563011010000711.

Zeynalov, A.A., Anoikin, A.A., Kulakov, S.A., Otcherednoy, A.K., Kurbanov, R.N., 2023. Gazma cave—a final middle Paleolithic site in Azerbaijan: Paleogeography, chronology, archaeology. Archaeol. Ethnol. Anthropol. Eurasia 51 (3), 40–49. https://doi.org/10.17746/1563-0110.2023.51.3.040-049. (Accessed 8 July 2024). https://journal.archaeology.nsc.ru/jour/article/view/1740.